

http://researchcommons.waikato.ac.nz/

Research Commons at the University of Waikato

Copyright Statement:

The digital copy of this thesis is protected by the Copyright Act 1994 (New Zealand).

The thesis may be consulted by you, provided you comply with the provisions of the Act and the following conditions of use:

- Any use you make of these documents or images must be for research or private study purposes only, and you may not make them available to any other person.
- Authors control the copyright of their thesis. You will recognise the author's right to be identified as the author of the thesis, and due acknowledgement will be made to the author where appropriate.
- You will obtain the author's permission before publishing any material from the thesis.

APPLICATIONS OF TRANSFORM TECHNIQUES IN ULTRASOUND IMAGING AND PROFILOMETRY

A thesis
submitted for the degree
of
Doctor of Philosophy in Physics
at the
University of Waikato
New Zealand

by

Han L. Zhang B.Sc., M.E.



University of Waikato
1995

ABSTRACT

This thesis consists of two parts. The first part describes the studies in the ultrasound pulse-echo frequency domain imaging and the second part presents the studies at the non-contact measurement of 3-D object surface using Fourier transform profilometry.

In the first part, the ultrasound backscattering characteristics of some simple phantoms were examined by two methods. These were 'pure' frequency domain ultrasound imaging based on peak frequencies in a series of echo spectra (or spectrograms) and the new type B mode frequency domain imaging based on both time domain and frequency domain information. The two major techniques used to analyse the time-varying echo signals, the short-time Fourier transform (STFT) and the orthogonal-like Gabor transform (OLGT), were studied and compared in details in order to generate more accurate spectrograms for imaging. The experimental results have found that the frequency domain images have better lateral resolution than the conventional B mode images. By using the appropriate short-time sliding window, the axial resolution in the frequency domain images can be improved. The new type B mode frequency domain images, which not only show the physical sizes of the scanned objects but also contain the frequency information of scattered targets, may have more potential diagnostic value in the future.

The second part describes how to improve the accuracy of non-contact measurement of three-dimensional (3-D) object surface by using the new image processing-based methods in Fourier transform profilometry. The methods include application of the weighted window function to the isolated first sidelobe in frequency domain, automatic determination of the bandwidth of bandpass filter based on the actual spectrum and use of object boundary guided phase unwrapping to solve large-scale discontinuities around the object boundary on the modulo 2π phase map. The accuracy of measurement of the 3-D object surfaces has been improved using those new image processing-based methods.

ACKNOWLEDGEMENTS

First, I would like to pay special thanks to my supervisor, Dr. Howell Round, who gave me so much encouragement, advice and guidance. Without his support, I would not have completed my thesis.

I would also like to thank Kees Klein for his technical support in building the ultrasound frequency domain imaging system and Craig Harper for his assistance in preparing the phantoms.

Part of my research programme was carried out at the Meat Industry Research Institute of New Zealand. Special thanks must go to Mark Loeffen for his supervision. Thanks also go to Ross Clarke for his valuable discussions and great effort implementing the Fourier transform profilometry software based on Takeda's methods.

Finally I would also like to thank my family for supporting me over the last three years when we have been in New Zealand.

CONTENTS

Abstract ii

Acknowledgements iii

Contents iv

List of Figures vii

List of Tables x

PART I ULTRASOUND FREQUENCY DOMAIN IMAGING

Chapter 1 Ultrasound Pulse-Echo Imaging Systems **I.1.1**

§ I.1.1 Introduction I.1.1

§ I.1.2 B Mode Ultrasound I.1.2

§ I.1.3 Doppler Ultrasound I.1.5

§ I.1.4 Use of Frequency Information in Ultrasound Echoes I.1.7

Chapter 2 Frequency Characteristics of A Pulse-Echo Spectrum **I.2.1**

§ I.2.1 Introduction I.2.1

§ I.2.2 Characteristics of a Spectrum of Short Ultrasonic Pulses I.2.2

§ I.2.3 Short-Time Fourier Transform I.2.5

§ I.2.4 Orthogonal-Like Gabor Transform I.2.7

Chapter 3 Ultrasound Frequency Domain Imaging System **I.3.1**

§ I.3.1 Introduction I.3.1

§ I.3.2 Setup of the System I.3.2

§ I.3.3 Phantoms I.3.5

§ I.3.4 Implementation of the Short-Time Fourier Transform I.3.7

§ I.3.5 Implementation of the Orthogonal-Like Gabor Transform I.3.12

§ I.3.6 Spectral Analysis 1.3.12

§ I.3.7 Image Formation I.3.13

§ I.3.8 Software I.3.14

Chapter 4 Experimental Results and Evaluations **I.4.1**

§ 1.4.1 Introduction I.4.1

§ I.4.2 Images of Wires I.4.2

§ I.4.3 Images of Grooves on Perspex Surface I.4.6
§ I.4.4 Comparison of Results from Fourier and Gabor Transforms I.4.10
Chapter 5 Conclusions and Suggestions I.5.1
§ I.5.1 Conclusions 1.5.1
§ I.5.2 Suggestions 1.5.2
Appendix A Fourier Transform and its Discrete and Fast Forms I.A.1
§ I.A.1 Fourier Transform I.A.1
§ I.A.2 Discrete Fourier Transform I.A.2
§ I.A.3 Fast Fourier Transform I.A.2
References I.R.1

PART II NON-CONTACT MEASUREMENT OF 3-D OBJECT SURFACE USING FOURIER TRANSFORM PROFILOMETRY
Chapter 1 Fourier Transform Profilometry II.1.1
§ II.1.1 Introduction II.1.1
§ II.1.2 Principle of Fourier Transform Profilometry II.1.3
Chapter 2 Image Processing Techniques II.2.1
§ II.2.1 Introduction II.2.1
§ II.2.2 Analysis of Major Causes of Error II.2.2
§ II.2.3 New Image Processing-Based Methods II.2.8
Chapter 3 Experimental Results II.3.1
§ II.3.1 Introduction II.3.1
§ II.3.2 Measured Phase Variation in Single Line II.3.2
§ II.3.3 Measured Phase and Height Distributions II.3.6
§ II.3.4 Object Boundary Guided Phase Unwrapping II.3.9
Chapter 4 Conclusions and Suggestions II.4.1
§ II.4.1 Conclusions II.4.1
§ II.4.2 Suggestions II.4.2
Appendix A The Traditional Takeda's Methods Used in Fourier Transform Profilometry II.A.1
§ II.A.1 Introduction II.A.1
§ II.A.2 Optical System II.A.1

§ II.A.3 Grating image II.A.3
§ II.A.4 Fourier Transform Method II.A.5
§ II.A.5 Phase Unwrapping II.A.7
§ II.A.6 Phase-To-Height Conversion II.A.10
§ II.A.7 Height Constraint II.A.10
Appendix B Comparison of Different Combinations of Weighted Window Functions **II.B.1**
References **II.R.1**

LIST OF FIGURES

PART I

Chapter 1

Figure I.1.1	Diagram of a medical transducer for pulse-echo imaging	I.1.2
Figure I.1.2	A mode display of ultrasound echo spikes	I.1.3
Figure I.1.3	A typical B mode display of ultrasound echoes	I.1.4
Figure I.1.4	The ultrasound beam field from the PICKER 595541 transducer	I.1.5

Chapter 2

Figure I.2.1	A normalized Gaussian-shaped spectrum	I.2.2
Figure I.2.2	Frequency shifting in the nearly ideal Gaussian-shaped spectra	I.2.4
Figure I.2.3	An example of the short-time Fourier transform	I.2.6
Figure I.2.4	A sliding window used in the short-time Fourier transform	I.2.7
Figure I.2.5	Orthogonal-like Gabor transform	I.2.10

Chapter 3

Figure I.3.1	A block diagram of ultrasound frequency domain imaging system	I.3.2
Figure I.3.2	Arrangement of wires	I.3.7
Figure I.3.3	Profile of grooves in a perspex block	I.3.7
Figure I.3.4	Hanning window	I.3.8
Figure I.3.5	Hamming window	I.3.8
Figure I.3.6	Hanning window impulse response	I.3.9
Figure I.3.7	Hamming window impulse response	I.3.9
Figure I.3.8	Horseshoe-shaped colour diagram	I.3.14

Chapter 4

Figure I.4.1	'Pure' frequency domain wire images using a window of 128 samples	I.4.4
Figure I.4.2	'Pure' frequency domain wire images using a window of 64 samples	I.4.4

Figure I.4.3 Improved 'pure' frequency domain Fourier image of wires using a short-time sliding window of 40 samples I.4.5
Figure I.4.4 New type B mode frequency domain images of wires I.4.6
Figure I.4.5 'Pure' frequency domain groove images using a short-time sliding window of 128 samples I.4.7
Figure I.4.6 'Pure' frequency domain groove images using a short-time sliding window of 64 samples I.4.8
Figure I.4.7 Improved 'pure' frequency domain Fourier image of grooves using a short-time sliding window of 40 samples I.4.9
Figure I.4.8 New type B mode frequency domain images of grooves I.4.10

PART II

Chapter 2

Figure II.2.1 A hemisphere reconstructed using the traditional methods in FTP II.2.2
Figure II.2.2 Aliasing in the DFT II.2.3
Figure II.2.3 Frequency leakage in the DFT II.2.5
Figure II.2.4 The edge operators in the y axis II.2.12
Figure II.2.5 The fringe image of a test hemisphere II.2.13
Figure II.2.6 The detected edges of a test hemisphere II.2.13
Figure II.2.7 The detected boundary of a test hemisphere II.2.13

Chapter 3

Figure II.3.1 Arrangement of image capture and processing II.3.1
Figure II.3.2 Phase variation in a single line reconstructed by using a Hanning window with the isolated sidelobe II.3.3
Figure II.3.3 Phase variation in a single line reconstructed by using a rectangular window with the isolated sidelobe II.3.3
Figure II.3.4 Phase variation in a single line reconstructed using the correct bandwidth of the bandpass filter II.3.4
Figure II.3.5 Phase variation in a single line reconstructed using a narrow bandwidth of the bandpass filter II.3.5
Figure II.3.6 Phase variation in a single line reconstructed

using a wide bandwidth of the bandpass filter II.3.5
Figure II.3.7 Measured phase variation on the surface of an ovine saddle by using the traditional methods II.3.7
Figure II.3.8 Measured phase variation on the surface of an ovine saddle by using the new methods II.3.7
Figure II.3.9 Measured height distribution of the hemisphere using the new methods II.3.8
Figure II.3.10 Measured height distribution of the hemisphere using the traditional methods II.3.8
Figure II.3.11 The fringe pattern of a 12" fan blade II.3.10
Figure II.3.12 Height distribution of the fan blade unsuccessfully reconstructed by using the traditional methods II.3.10
Figure II.3.13 Detected boundary of the 12" fan blade II.3.11
Figure II.3.14 Height distribution of the fan blade reconstructed by using object boundary guided phase unwrapping II.3.12
Figure II.3.15 Measured height distribution of the hemisphere using the object boundary guided phase unwrapping algorithm II.3.12
Figure II.3.16 A computer-generated hemisphere II.3.13
Figure II.3.17 Measured profile of a thick rubber ring using the new methods II.3.14
Figure II.3.18 Measured profile of a thick rubber ring using the traditional methods II.3.14

Appendix A

Figure II.A.1 Crossed-optical-axes geometry II.A.2
Figure II.A.2 Parallel-optical-axes geometry II.A.2
Figure II.A.3 The spectra of deformed grating image for a fixed y value II.A.6
Figure II.A.4 An example of phase discontinuities and phase unwrapping II.A.8

LIST OF TABLES

PART II

Chapter 3

Table II.3.1 Mean and standard deviation of errors between the measured hemispheres and the actual test hemisphere II.3.13

Appendix B

Table II.B.1 Statistics of errors for different combinations of windows II.B.3

PART I CHAPTER 1

ULTRASONIC PULSE-ECHO IMAGING SYSTEMS

§ I.1.1 Introduction

Ultrasound is a special form of sound with frequency higher than the limit of human hearing (about 20 kHz). Since ultrasound was first applied in medical diagnosis by Dussik in Austria (1937), many sophisticated ultrasonic imaging systems have been developed and used in medical diagnosis and the ultrasonic imaging has become second only to conventional X-ray in terms of number of clinical procedures performed (Shung et al., 1993). This is because ultrasound imaging presents no radiation hazard and high quality images of soft tissues can be obtained. Also the imaging systems are relatively cheap and portable compared with the other medical imaging systems (Kuttruff, 1991). As a result, ultrasonic imaging is playing an important role in present medical diagnoses (Wells, 1993).

In most medical ultrasonic imaging systems, a short pulse of ultrasound energy is emitted by a transducer and reflected and/or backscattered by objects in the medium and finally received by the same transducer as echoes. The received ultrasound echoes are converted to electrical signals and heavily processed and eventually displayed as an image on a monitor. Although the ultrasonic pulse-echo imaging systems of this kind were developed a number of decades ago, yet the principles in the early stage ultrasonic pulse-echo imaging systems are still used in the present sophisticated ultrasound equipments.

In general, the B mode (or A mode) ultrasound is used to image stationary organs, and the Doppler ultrasound is used to detect and analyse the flow of blood. But the simultaneous application of these two modes is used in some special areas such as in the human heart (Kuttruff, 1991). Most ultrasonic pulse-echo imaging systems use amplitude demodulation (AM) in image formation. In this way, the frequency information in the detected ultrasound echo signals is lost during the image

processing. The frequency information, however, is crucial for the estimation of certain tissue parameters (Seggie et al., 1985). So during the last two decades, the attention had been focused on how to use the frequency information in the reflected and/or backscattered ultrasound echoes in ultrasonic imaging and tissue characterization (Oosterveld et al., 1989).

This chapter first describes the two principal ultrasonic imaging modes: B mode ultrasound and Doppler ultrasound, and then discusses current research being carried out on using frequency information in ultrasonic imaging and tissue characterization.

§ I.1.2 B Mode Ultrasound

The ultrasound is normally generated through the inverse piezoelectric effect. When a high voltage electric pulse is applied to the surface of piezoelectric material (crystal), the crystal continuously changes its shape by expanding and contracting. This causes a pulse of ultrasound to be transmitted into the medium in front of the crystal. An ultrasonic transducer or probe is usually made by mounting a 'backing block' against the rear face of the crystal to absorb the backward travelling wave and to limit the duration of the ultrasound pulse to three or four cycles. A typical form of construction of an early medical ultrasound transducer for the generation and detection of short pulses is shown in Figure I.1.1. In general, the short ultrasound pulses are used in a medical transducer because they provide high axial resolution.

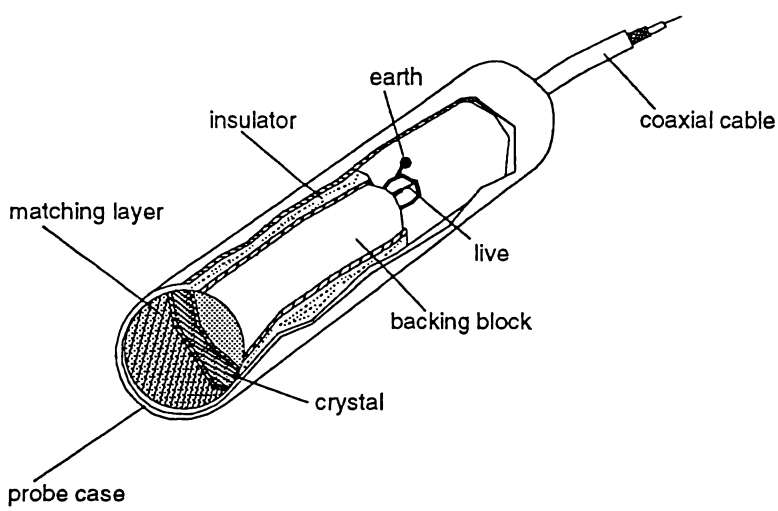


Figure I.1.1: Diagram of a medical transducer for pulse-echo imaging (Wells, 1977)

The short ultrasonic pulses travelling through the medium are reflected and/or backscattered by some objects in the region of interest (ROI) and received as echo signals by the same transducer. Because of attenuation and absorption of ultrasound in medium, some signal processing techniques such as pre-amplification and time gain compensation (TGC) are used after the ultrasound echoes are converted into the electrical signals to improve the signal. For measuring the structure of stationary objects in human body, there are two basic display modes in the ultrasonic pulse-echo imaging system, which are called the A (amplitude) and B (brightness) modes respectively.

In the A mode, the received ultrasonic echo signals in a scanning line are rectified and smoothed (i.e., amplitude demodulated) so that only the envelopes of echo signals are retained to represent the magnitudes of the echo spikes in that direction. The magnitudes of echo spikes are finally displayed by the envelopes of the echo signals on a cathode ray oscilloscope (CRO) as shown in Figure I.1.2. In this way it is impossible to use the A mode to display two-dimensional (2-D) anatomical section so that the application of the A mode is very limited in the clinical practice. However the circuit in the A mode is an essential 'building-block' in the make-up of a modern ultrasound scanner (Lerski, 1988).

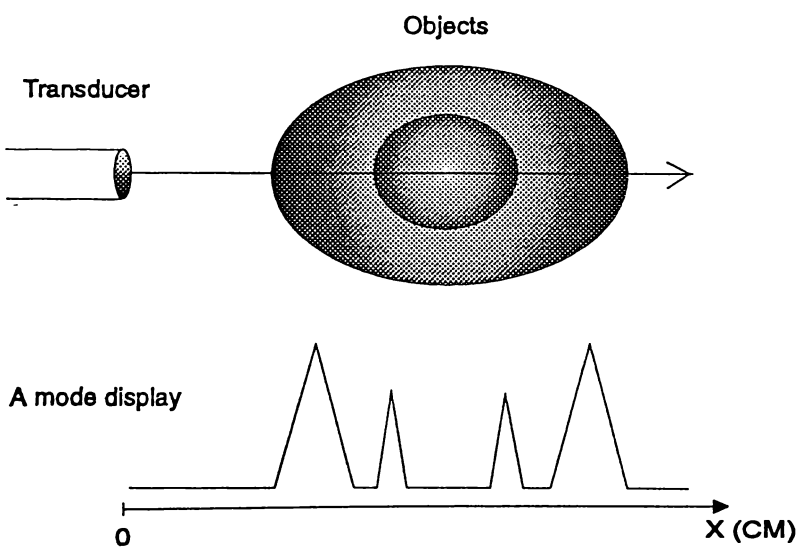


Figure I.1.2: A mode display of ultrasound echo spikes

Unlike in the A mode, the echo spikes along a single scanning line are displayed in the B mode as grey scale spots on a monitor according to their magnitudes. When the transducer itself is systematically moved or an array of transducers is linearly arranged so that the ultrasonic beam sweeps cross a plane section of interest in a human body, a 2-D image of the tissue anatomy is produced. A typical B mode display of ultrasound echoes from the object boundaries is shown in Figure I.1.3. Here the transducer is a linear array of ultrasonic elements of which a small group are simultaneously excited to obtain echoes in a line in front of them.

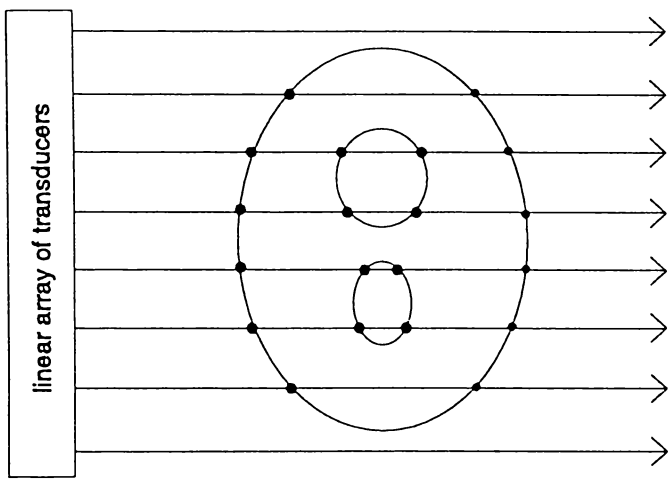


Figure I.1.3: A typical B mode display of ultrasound echoes

The quality of an image is commonly measured by its resolution. In a 2-D ultrasonic pulse-echo image, there are two spatial resolutions of importance: the axial resolution and the lateral resolution. The axial resolution fundamentally depends on the ultrasonic pulse length because the pulse length itself is often 3-4 cycles in modern ultrasound transducers and the speed of ultrasound is almost constant within a certain medium. Therefore the higher the frequency i.e., the shorter the wavelength, means the shorter the pulse length and therefore better axial resolution. The lateral resolution mainly depends upon the effective width of the ultrasound beam at the position of the reflecting objects. The narrower effective width of ultrasound beam will allow objects closer together to be resolved.

To narrow the effective width of ultrasound beam, it is usual to focus an ultrasound beam by using a concave crystal or by placing the acoustic equivalent of an optical concave lens in front of a flat crystal. In consideration of a practical range of scanning distance, the ultrasound beam should not be focused too strongly. A typical ultrasound beam field from a focused transducer, which was measured using a hydrophone and used in my experiments is shown in Figure I.1.4.

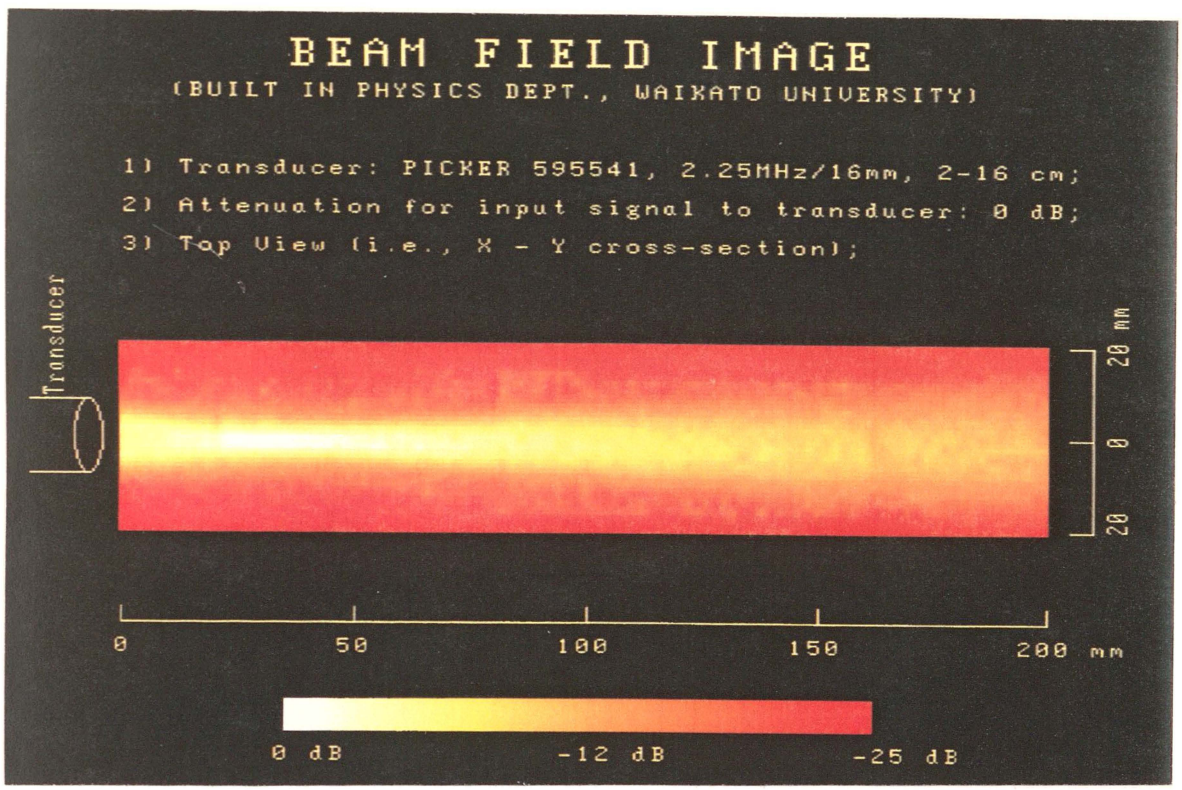


Figure I.1.4: The ultrasound beam field from the PICKER 595541 transducer

The peak of the hydrophone output was measured using the pulsed ultrasonic signal. The colour scale used in the above picture is similar to a temperature-colour scale (red-orange-white), red representing the lowest magnitude and white the highest.

§ I.1.3 Doppler Ultrasound

Doppler ultrasound is another major method used in ultrasonic pulse-echo imaging systems to detect the speed of moving objects. The Doppler principle was first discovered in the later nineteen century and its key phenomenon is well-known in physics, i.e., that when a source of sound moves towards an observer, the frequency

of sound becomes higher and when it moves away the frequency becomes lower.

In the Doppler ultrasound system used in medical diagnosis, the reflected echo signals from moving objects are multiplied with the original transmitted pulses. As in the frequency modulation (FM) in communication, the result of modulation generates two new sinusoidal signals with frequencies equal to the sum frequency and the difference frequency between the transmitted pulse and the received echo signal. The signal with the difference frequency is then separated by a low pass filter. The frequency difference (or the frequency shifting) in the filtered signal depends the velocity of the moving object. Often there is an angle between the ultrasonic beam scanning line and the direction of a moving object, so the differences in frequency shifting do not correspond to the different velocities of moving objects unless they are moving in the same direction. Nevertheless, the Doppler ultrasound is still useful to extract speed information about moving objects in a specific region of interest where most objects have a similar direction of motion.

Usually, the moving objects to be measured have different velocities. For example in human blood vessels, the blood flow has a typical velocity distribution: near the blood wall the corpuscles are moving slower than in the centre. Therefore the detected Doppler frequency differences in the filtered signal in general do not consist of the single frequency, but a spectrum of frequencies. Examination of the Doppler spectrum can reveal the complete distribution of blood flow velocities in the vessel.

Since colour flow Doppler imaging was first applied to medical diagnosis in early 1980s (Kasai et al., 1985), the Doppler ultrasound technique has often been combined with the B mode in the field of special interest, for instance, of the heart. In that case, the information in Doppler frequency shifting is first mapped into a set of pseudo colours that represent the blood flow velocities in different ventricles, which are then superimposed upon the B mode grey-scale image. That finally generates a very vivid image of the heart activity (Kuttruff, 1991).

§ I.1.4 Use of Frequency Information in Ultrasound Echoes

Although the conventional B mode ultrasound imaging system is commonly being used in current medical diagnosis, potentially valuable frequency information in the received ultrasound echoes is lost during image formation. More and more researchers have believed that some particular tissue characterization can be made by using the frequency information in the received radio-frequency (RF) echo signals. During the last two decades, many researchers had been investigating the possibilities of using the frequency information in the RF echo signals to help determine some tissue characterization and diagnose the difficult clinical problems (Lizzi et al., 1976 and 1983; Ferrari et al., 1984a and 1984b; Seggie et al., 1985; Romijn et al., 1986; Round et al., 1987; Thijssen et al., 1990).

In the middle of 1970s the spectral analysis of the reflected ultrasonic echo signals was used to help determine the parameters in three kinds of tissue: tissue with nearly-parallel planes boundaries (curved surfaces of cysts, encapsulated tumours, and ocular lenses), tissue with heterogeneous interior structure (malignant melanoma) and tissues causing acoustic 'shadowing' of posterior regions (in orbital fat) (Lizzi et al., 1976 and 1983). The three tissue parameters: absorptivity, relative acoustic impedance differences and velocity dispersion in the approximately-parallel tissue surfaces were all shown to be related to the frequency. The statistical measures of volume scattering and attenuation in heterogeneous tissue were made after the analysis of the average power spectra of the echoes. The attenuation characteristic in the posterior shadowed tissue was obtained by comparing the spectra of the same posterior tissue with and without shadowing.

In 1980s, interest in the instantaneous frequency and phase information in the ultrasound echoes grew. For example, the phase information encoded in the ultrasound pulse-echo signals was used to generate an instantaneous frequency modulation (FM) image, which was combined with the conventional AM information using the method of real zero conversion (RZC). The final image was less prone to the lateral beam artefact (Ferrari et al., 1984a and 1984b; Seggie et al., 1985). Also, the instantaneous centre frequency in the reflected ultrasonic echoes was observed to

shift due to the contributions of scatterers in the tissue. The Hilbert transform based on a finite impulse response (FIR) digital filter was thus used to detect the frequency shifting, which had important implication for tissue characterization, especially the attenuation in the tissue (Gehlbach et al., 1985). The centre frequency in the Gaussian-shaped backscattered echoes was found to shift to a slightly higher frequency when the scatterers' dimensions were less than or similar to the wavelength of the ultrasound pulse (Round et al., 1987).

More recently, the phase-derivative (PD) imaging was investigated. The phase is found by adding an analytic signal into the original RF echo signal. The resulting signal suffers because of the instability in the derived phase when the echo is too small. Thus some methods for the stabilised PD imaging were further investigated (Romijn et al., 1986 and 1987; Thijssen et al., 1990).

There were five practical methods to generate a stabilized PD image. In the first zero-crossing method an adequately-defined sine wave or *squelch* (Kay et al., 1986) was added on to the original radio-frequency echo signal and then the instantaneous frequency was obtained by taking the inverse of the time intervals between estimated successive zero-crossings in the composite signal (Komaili et al., 1986). The second and third methods directly took the phase derivative of the analytic signal that was composed of the original radio-frequency echo signal as the real part and its Hilbert transformed signal as the imaginary part (Ferrari et al., 1984a and 1984b). For the stabilization, the second method added the squelch signal on the analytic signal and the third method multiplied the analytic signal with a Wiener kernel. The fourth method was called phase unwrapping. The phase as a function of time in the analytic signal was first calculated explicitly. Since the standard algorithm may cause 2π-steps in the phase data, this discontinuities must be removed using phase unwrapping before differentiating the phase data with respect to time (Romijn et al., 1986). In the fifth method, called the smoothed analytic signal, the phase was smoothed before the derivation was performed.

The PD images developed by adding a squelch signal as described in the first and second methods resembled the conventional B mode images. The third method

employing a Wiener kernel generated the PD images containing both envelope and phase information. The fourth and fifth methods provided the "pure" PD images because of using the time derivative of the phase.

Also, the statistical parameters of phase derivative images obtained from the randomly distributed scatterers have been investigated (Thijssen et al., 1990; Oosterveld et al., 1989). Under the assumptions of incident plane wave ultrasound pulses, the echo signal generating process could be considered as a stochastic process. The echo signal was then described as a Possion time series that was convolved with the transmission pulse of the transducer. As a result, the probability density function (pdf) of the echo signal approximated to a Gaussian pdf for a narrow band pulse waveform. The mean, standard deviation and signal-to-noise ratio of the rectified phase derivatives were then derived from the pdf under the assumption of a Gaussian transmission pulse. The discovery of the statistical parameters of phase derivatives gave a good understanding of the texture of randomly distributed scatterers in a PD image.

In summary, the interest in using the frequency or phase information in radio-frequency ultrasound echo signal is growing. The construction of all sorts of "pure" frequency domain images and a new type of B mode images that contain both time domain and frequency domain information have been under intensive investigation (Oosterveld et al., 1989).

PART I CHAPTER 2

FREQUENCY CHARACTERISTICS OF A PULSE-ECHO SPECTRUM

§ I.2.1 Introduction

The conventional B mode ultrasound imaging systems use only the envelope information of the received echoes from stationary targets, although the Doppler ultrasound imaging systems use the detected frequency shifting information of moving targets. In fact, the ultrasonic echo signals from the stationary targets contain some important frequency information that can be used in tissue characterization and clinical diagnosis as described in the last section of chapter one. Notably, the echo signals backscattered from some small targets whose dimensions are less than the wavelength of the ultrasound pulses have different frequency characteristics from the original pulses. A significant experimental result was that the ultrasonic echo signals backscattered from small targets such as wire-like fibres differed from those of the original pulses in the peak frequency and the bandwidth (Surridge, 1980; Round et al., 1987). This would certainly be helpful to identify the small targets such as blood cells, the fine fibres and other textures in the human tissue or in any other imaged system.

Is it possible to build an ultrasound image totally or partially based on the spectra of echo signals? Having investigated a number of methods to obtain a series of spectra (the spectrograms) of the received time-varying radio frequency (RF) echo signals, I have concluded that it is possible. The short-time Fourier transform (STFT) and the orthogonal-like Gabor transform (OLGT) are two major methods which were used to obtain the spectrograms. The images I built heavily depend on the peak (centre) frequencies in the spectrograms. So it is important to understand the characteristics of a single spectrum of ultrasound pulses and a single spectrum of the received echoes respectively.

This chapter will first review the frequency characteristics of a typical spectrum of short ultrasonic pulses generated by a common medical transducer and an ideal spectrum of ultrasonic echoes reflected and/or backscattered by small objects. Then it will describe in detail the theoretical basis for the short-time Fourier transform and the orthogonal-like Gabor transform that are used to obtain the spectrograms of ultrasonic echo signals.

§ I.2.2 Characteristics of a Spectrum of Short Ultrasonic Pulses

The shape of a power spectrum of the short ultrasonic pulses is considered to be Gaussian in the ideal condition (without noise) (Dines et al., 1979; Round et al., 1987). The normalized magnitude in the power spectrum of the ideal short ultrasonic pulses is shown in Figure I.2.1 and its mathematical form is expressed by (I-2-1).

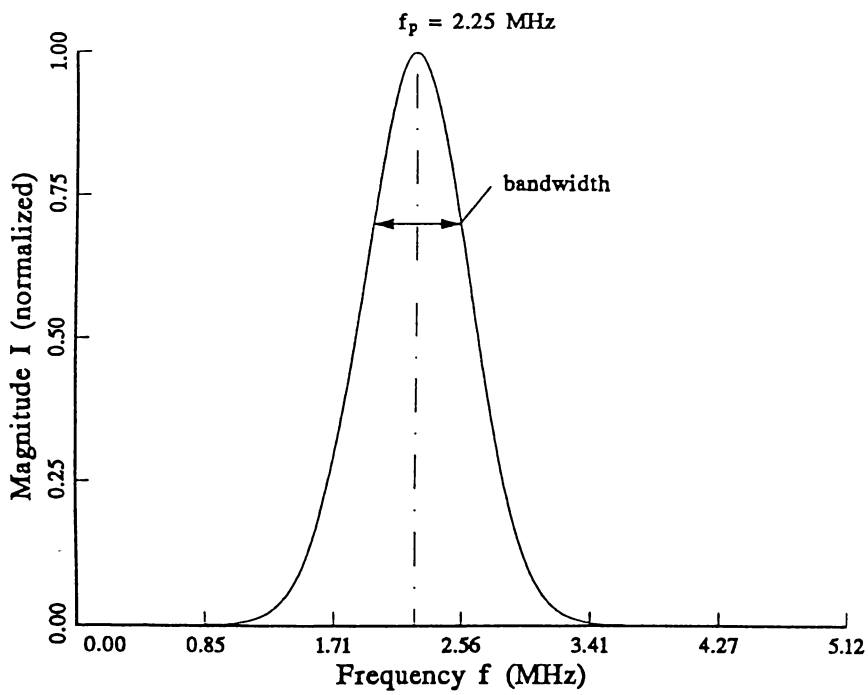


Figure I.2.1: A normalized Gassian-shaped spectrum

$$I(f) = I_o \exp\frac{-(f-f_o)^2}{2\sigma^2} \qquad \text{(I-2-1)}$$

where I_o is the maximum magnitude at the spectrum that occurs at the resonant frequency f_o and σ is a measure of the bandwidth that is located at -3dB of the maximum magnitude or 0.707 I_o.

If short ultrasonic pulses are reflected back from a flat plane perpendicular to the direction in which the pulses are travelling, the spectrum of the reflected echoes has the same shape as that of the original short pulses providing that the frequency-dependent attenuation and distortion of the pulses are small.* However, if the short pulses are backscattered from some small targets whose dimensions are similar to or less than the wavelength of short ultrasonic pulses, then a simple scattering function shown in (I-2-2) can be used to describe the spectrum of backscattered echoes (Round et al., 1987).

$$I_B(f) = k' f^s I_R(f) \qquad \text{(I-2-2)}$$

where $I_B(f)$ and $I_R(f)$ are the power spectra of backscattered echoes and reflected echoes separately. k' and s are constants depending upon the features of medium and geometry of the scanned target respectively. Typically, if the scanned target is a wire whose dimension is less than the wavelength of ultrasonic pulses, then $s \approx 3$. If the target is a small bead whose diameter is much less than wavelength of ultrasonic pulses, then $s \approx 4$. Within the human body, most muscles made of long fibres are approximately of wire shape and the blood cells are similar to the beads.

It is noticeable from (I-2-2) that the spectrum of such backscattered ultrasonic echo signals contains more higher frequency components than that of the reflected echo signals, although they have a similar Gaussian shape. Furthermore, the peak frequency f_p in the spectrum of backscattered echo signals can be found by taking the derivative of (I-2-2) and solving the following equation

$$\frac{dI_B(f)}{df} = 0 \,. \qquad \text{(I-2-3)}$$

The found peak frequency f_p is shown in (I-2-4).

* (Wells, 1977)

$$f_p = \frac{f_o}{2} + \sqrt{\frac{f_o^2}{4} + s\sigma^2} \qquad \text{(I-2-4)}$$

As the constant s is usually greater than one, then the peak frequency in the backscattered echo signals is "shifted" to a higher frequency compared to that found in the spectrum of the reflected echo signals. That theory was mentioned in the papers by Surridge and by Round and the experimental results from wires were presented by Round. The shifting range was approximately 80-100 kHz for a central frequency of 1.9 MHz with a bandwidth of 600 kHz. The frequency shifting is illustrated in Figure I.2.2 by using two nearly ideal Gaussian-shaped spectra.

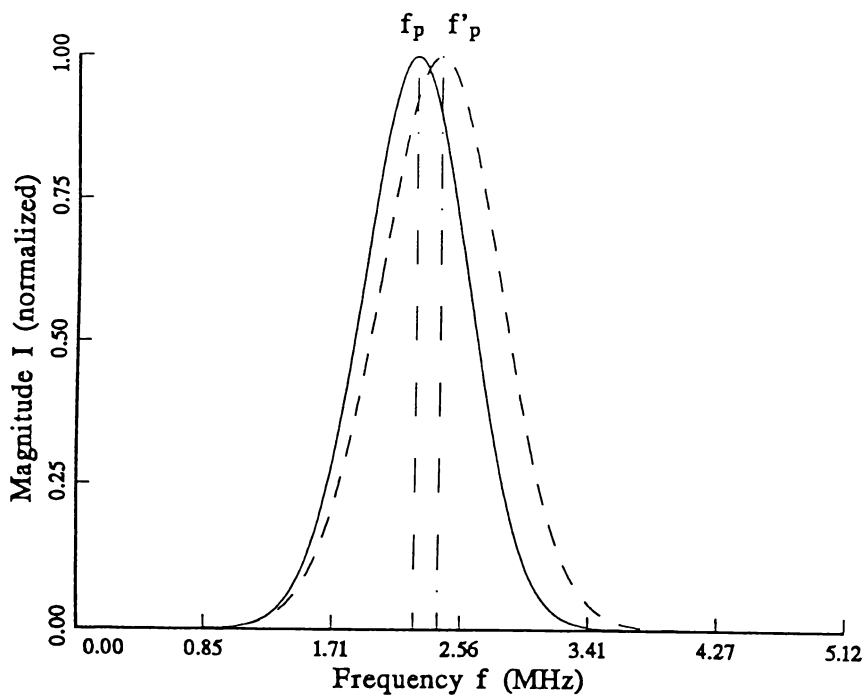


Figure I.2.2: Frequency shifting in the nearly ideal Gaussian-shaped spectra

The spectrum of original short ultrasonic pulses is represented by the solid line in Figure I.2.2. It differs from the spectrum (dotted line) of echo signals backscattered from a wire in peak frequency and bandwidth.

In a practical ultrasonic pulse-echo imaging system, however, the received echo

signals are more complicated. The ultrasonic pulses experience many physical phenomena such as attenuation, refraction, reflection, scattering and absorption as they are travelling through the medium. Also, the received and digitised echo signals contain a significant amount of noise generated in the electronic equipment and the environment. This will certainly distort the Gaussian shape of the spectrum but the Gaussian-like spectrum can still be recognized in most cases (Harper, 1990).

The spectrum of ultrasonic echo signals is often obtained using the traditional discrete Fourier transform (DFT) or the fast Fourier transform (FFT). The Fourier transform and its discrete and fast forms are described in Appendix A. However, the received ultrasonic echo signals are time-varying. That means the signals received at the different delay times contain not only different intensities but also different frequency components. Therefore the short-time Fourier transform or the orthogonal-like Gabor transform can be employed to obtain a series of spectra (spectrograms) of time-varying echo signals.

§ I.2.3 Short-Time Fourier Transform

The ultrasound echoes received in each scanning line are time delay dependant. That means the intensities and the frequency components of the echo signals received at the different delay times are different. In the B mode display, the intensities of received echo signals are represented by the magnitudes of echo envelopes and displayed on a screen using different levels of brightness. To represent the received echo signal at the different delay times using its frequency information (for instance, the peak frequency) in its Gaussian-shaped spectrum, a series of spectra of echo signals along each scanning line are needed.

The short-time Fourier transform is often used to analyse such a kind of time-varying signals (Cohen, 1989). The performance of the short-time Fourier transform is illustrated in Figure I.2.3 for an ideal time-varying signal.

This ideal time-varying signal consists of several sine waveforms with different frequencies but the same number of samples in each waveform. A short-time window

is employed to extract the samples from each sine waveform and those samples are then Fourier transformed to obtain the spectrum of every sine waveform.

In Figure I.2.3, the ideal time-varying signal is shown in (a). Each sine waveform that is extracted by a short-time window is shown in (b) and the spectra of those extracted sine waveforms are shown in (c).

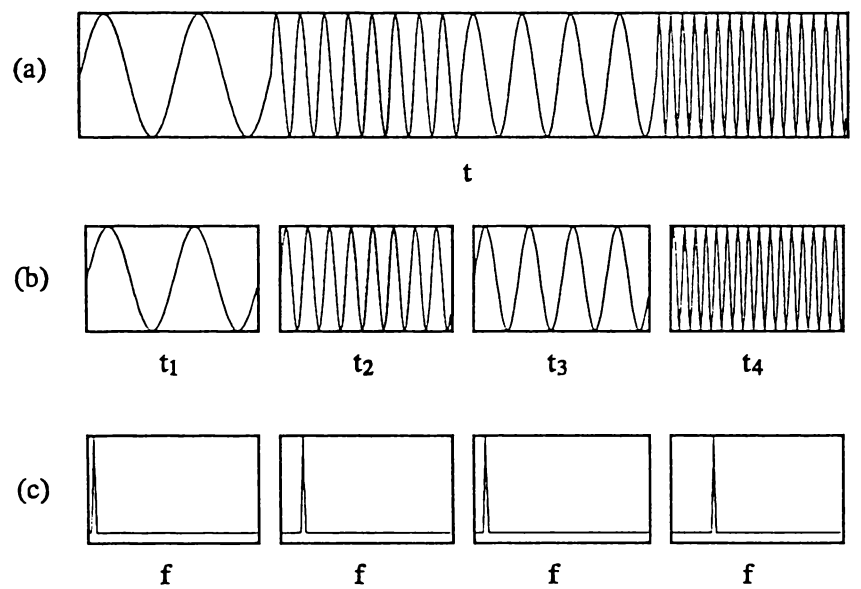


Figure I.2.3: An example of the short-time Fourier transform

The actual time-varying signals to be analysed from an ultrasonic imaging system, however, are more complicated. The spectral contents in signals are irregularly changed and unevenly distributed. To discover completely the frequency components at every instant of the time-varying signals, the Fourier transform has to be taken at every sampling point. That involves heavy data overlapping and consequently a lot of computation is needed. In practice, however, a short-time sliding window is used to shift more than one sample each time as shown in Figure I.2.4.

In Figure I.2.4, the waveform of echoes received on a single scanning line is shown in the top and part of the echo signals are continuously extracted from a short-time sliding window while the window is shifted forward by a constant time interval.

The choice of the window length and overlapping width can often distort the spectrum. A wider window gives good resolution in the frequency domain but poor resolution in the time domain. Conversely, a narrow window produces good time domain resolution but poor frequency domain resolution. The details in implementation of the short-time Fourier transform on the received ultrasonic echo signals are discussed later in chapter three.

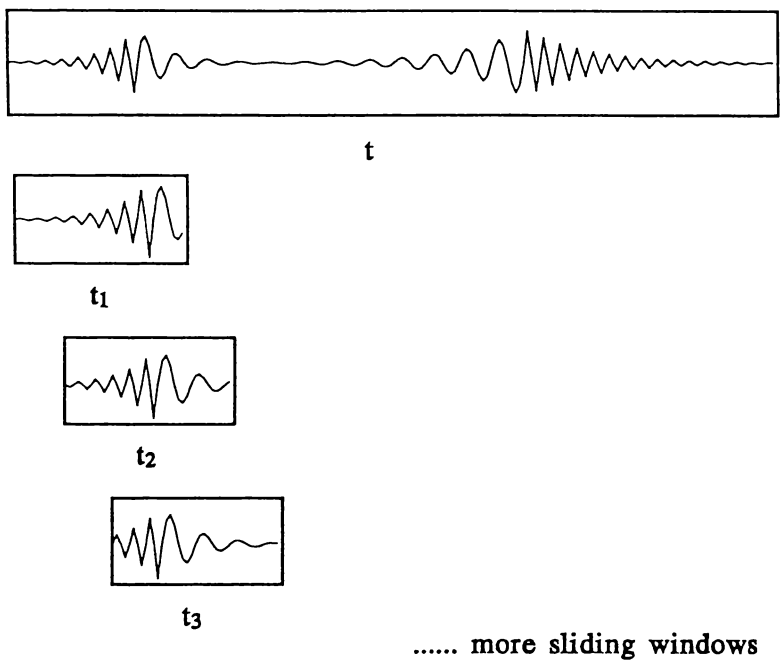


Figure I.2.4: A sliding window used in the short-time Fourier transform

Although the short-time Fourier transform has some disadvantages in computation speed and time-frequency resolution, it is still widely used in analysis of time-varying signals because of its simplicity and also it is well-known (Cohen, 1989).

§ I.2.4 Orthogonal-Like Gabor Transform

The Gabor expansion has received considerable attention in the signal processing community over the past four decades. The Gabor expansion was first presented by D. Gabor in 1946 as an approach to devise a joint function of time and frequency that would describe the energy density or intensity of a signal simultaneously in time

and frequency (Gabor, 1946). For a signal $s(t)$, the Gabor expansion is defined as:

$$s(t) = \sum_{m=-\infty}^{\infty} \sum_{n=-\infty}^{\infty} C_{m,n}\, h_{m,n}(t) \qquad \text{(I-2-5)}$$

where $C_{m,n}$ are the Gabor coefficients and $h_{m,n}(t)$ are the time and frequency shifted version of a synthesis window function $h(t)$, i.e.,

$$h_{m,n}(t) = h(t-mT)\, e^{jn\Omega t} \qquad \text{(I-2-6)}$$

where the time shift constant T and the frequency sample interval Ω determine the sampling grid pattern and density in the joint time and frequency domain. The existence of the Gabor expansion is only possible when the product of ΩT is less than or equal to 2π (Gabor, 1946; Bastiaans, 1981; Janssen, 1981). Usually the Gabor coefficients $C_{m,n}$ are calculated by

$$C_{m,n} = < s(t),\ \gamma_{m,n}(t) > \qquad \text{(I-2-7)}$$

where $< >$ denotes the inner product and $\gamma_{m,n}(t)$ is the time and frequency shifted version of the analysis window function $\gamma(t)$.

Although the Gabor expansion has been recognized to be very useful for signal processing, its applications are limited because it is difficult to find the analysis window function $\gamma(t)$ which should be biorthogonal to an arbitrary given function $h(t)$, i.e.,

$$\frac{\Omega T}{2\pi} \int_{-\infty}^{\infty} h_{m,n}(t) \gamma_{k,l}^{*}(t) = \delta(m-k)\delta(n-l)\ . \qquad \text{(I-2-8)}$$

In addition, the Gabor expansion is mainly used to characterize the underlying signal's local behaviour in the joint time and frequency domain. However, it is more difficult to have both the synthesis window functions $h(t)$ and its corresponding biorthogonal analysis window function $\gamma(t)$ concentrated in the joint time and

frequency domain. That means sometimes the synthesis window function $h(t)$ is indeed locally concentrated, but the Gabor coefficients $C_{m,n}$ do not reflect the local behaviour of $s(t)$ because the corresponding analysis window function $\gamma(t)$ is not locally concentrated.

The Gabor expansion for a finite or periodic discrete-time sequence $s(i)$ with length L is defined as (Wexler and Raz, 1990):

$$s(i) = \sum_{m=0}^{M-1} \sum_{n=0}^{N-1} C_{m,n}\, h_{m,n}(i) \qquad \text{(I-2-9)}$$

$$h_{m,n}(i) = h(i - m\Delta M)\, e^{j\frac{2\pi n \Delta N i}{L}} \qquad \text{(I-2-10)}$$

where $0 \le i \le L\text{-}1$, and $M\Delta M = N\Delta N = L$. The ΔM and ΔN represent time and frequency sampling intervals, respectively. For a stable reconstruction, it must be satisfied that $\Delta M \Delta N \le L$. The Gabor coefficients $C_{m,n}$ may be complex values and given by

$$C_{m,n} = < s(i),\ \gamma_{m,n}(i) > \qquad \text{(I-2-11)}$$

where the analysis window function $\gamma_{m,n}(i)$ must satisfy the orthogonal condition in discrete form (Wexler and Raz, 1990):

$$\sum_{i=0}^{L-1} h(i+mN)\, e^{-j\frac{2\pi n M i}{L}} \cdot \gamma^*(i) = \delta(m)\delta(n)\ . \qquad \text{(I-2-12)}$$

Using a matrix notation $H\gamma = \mu$ [$\mu=(1,0,\ldots,0)^T$] for (I-2-12), the orthogonal function $\gamma(i)$ can be found using a minimum energy equation (Qian et al., 1992):

$$\min_{\substack{\alpha,\beta,\gamma \\ H\gamma=\mu}} E = \left\| \frac{\gamma}{\|\gamma\|} - \frac{h_{\alpha,\beta}}{\|h_{\alpha,\beta}\|} \right\|^2 \qquad \text{(I-2-13)}$$

where α and β are the time and frequency shift parameters, and $H\gamma = \mu$ is the

orthogonal condition. By introducing time and frequency shift parameters, it makes the function $h_{\alpha\beta}(i)$ have the same support region as $h(i)$, except to a different centre due to time or frequency shift. Consequently there is more freedom to minimize the energy E and thereby obtain a better concentrated $\gamma(i)$. The resulting solution of (I-2-13), $\gamma(i)$, is called the optimal biorthogonal function and the Gabor transform using the optimal biorthogonal function $\gamma(i)$ is called the orthogonal-like Gabor transform (Qian et al., 1993).

Although other functions can be selected as the synthesis window function $h(i)$, the normalized Gaussian function is found to be optimally concentrated in both time and frequency and used by National Instruments[1] (NI) in its software product *Gabor Transform*.

The orthogonal-like Gabor transform can be shown in Figure I.2.5 using a simple example (Almgren, 1993).

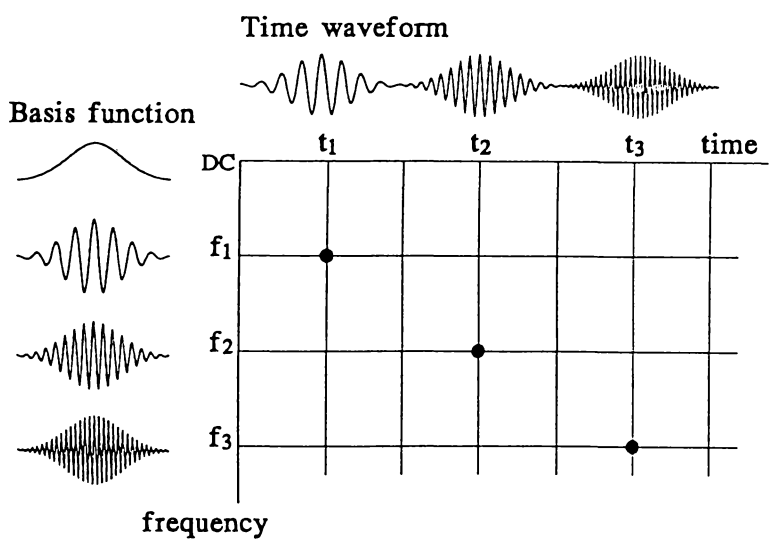


Figure I.2.5: Orthogonal-like Gabor transform

The sign • in Figure I.2.5 represents the Gabor coefficients at the specified time and

1 --- National Instruments, 6504 Bridge Point Parkway, Austin, TX 78730-5039, USA.

frequency region.

For the time-varying signals, the distribution of the energy over the frequencies is time-dependent. Two different approaches have been used to deal with this situation (Claasen et al., 1980).

In the first, a short-time sliding window is applied so that the signal within the window is considered to be stationary. The Fourier transform of this windowed signal can be used to characterize the energy distribution of the signal at the time that is given at the centre of that window.

In the second approach, the concept of instantaneous power spectrum is introduced (Page, 1952; Rihaczek, 1968; Delprat, 1992). From a number of different definitions of this concept, the Wigner distribution that originates from quantum mechanics has remarkable performance (Wigner, 1932).

In practice, the varieties of Wigner distribution have been used in this field. In the software product *Gabor Transform*, the pseudo Wigner-Ville distribution (PWVD) of the normalized Gaussian function shown in (I-2-14) is used.

$$PWVD_{h_{m,n}}(i,k) = 2e^{-[\frac{(i-m\Delta M)^2}{\sigma^2} + (\frac{2\pi\sigma}{L})^2(k-n\Delta N)^2]} \qquad \text{(I-2-14)}$$

After the Gabor coefficients $C_{m,n}$ are obtained, the PWVD in (I-2-14) is applied to each time-shifted and frequency-modulated basis function $h(i)$. The final Gabor spectrogram is found in (I-2-15).

$$GS(i,k) = 2\sum_{m=0}^{\frac{M}{2}-1}\sum_{n=0}^{\frac{N}{2}-1} |C_{m,n}|^2 \, e^{-[\frac{(i-m\Delta M)^2}{\sigma^2} + (\frac{2\pi\sigma}{L})^2(k-n\Delta N)^2]} \qquad \text{(I-2-15)}$$

The computational ratio between the short-time Fourier transform and the orthogonal-like Gabor transform is approximately shown in (I-2-16) and the ratio between the

number of parameters used in the short-time Fourier transform and the orthogonal-like Gabor transform is shown in (I-2-17).

$$R_1 = \Delta M(1 + \frac{\ln \Delta N}{\ln N}) \qquad \text{(I-2-16)}$$

$$R_2 = \Delta M \Delta N \qquad \text{(I-2-17)}$$

Normally, the time and frequency intervals ΔM and ΔN in the orthogonal-like Gabor transform are greater than 1. Therefore it is faster to obtain a spectrogram using the orthogonal-like Gabor transform than using the short-time Fourier transform for the same data sequence. In addition, the PWVD of the normalized Gaussian function is known and can be stored in a lookup table, the speed in the implementation of the orthogonal-like Gabor transform can be improved further. If both ΔM and ΔN are equal to one, the orthogonal-like Gabor transform is just the short-time Fourier transform (STFT).

The orthogonal-like Gabor transform has better resolution spectrogram than the short-time Fourier transform, because the Wigner distribution calculates the instantaneous power spectrum of the time-varying signals instead of the stationary spectrum calculated using the short-time Fourier transform, and thus more precisely represents the local frequency characteristics of the time-varying signals.

PART I CHAPTER 3

ULTRASOUND FREQUENCY DOMAIN IMAGING SYSTEM

§ I.3.1 Introduction

The spectra of the ultrasonic echo signals backscattered from small targets or particles have different frequency characteristics than those of the specularly reflected echo signals in that peak frequency and bandwidth are changed as described in the previous chapter. Using the short-time Fourier transform or the orthogonal-like Gabor transform, it is possible to construct an ultrasonic image based on the frequency characteristics. Unlike conventional ultrasound B mode imaging, ultrasound frequency domain imaging should provide additional information about the ultrasound backscattering function of small particles. This should be helpful in diagnosis of human soft tissue texture and in analysing backscattering for other non-destructive testing purposes.

To investigate this possibility, ultrasonic frequency domain images of some simple phantoms have been constructed in the laboratory. Those images are mainly based on the peak frequencies in a series of spectra or spectrograms of received ultrasound echo signals, although the other frequency characteristic such as the bandwidth may be used. The images were constructed using an ultrasound frequency domain imaging system developed in the medical physics research laboratory of the Waikato University. The entire system includes an ultrasonic pulse-echo transceiver, a signal digitizer, a phantom-moving controller, a personal computer (PC), and finally an image display unit.

In this chapter, each part in this ultrasound frequency domain imaging system is first described and then a number of simple phantoms used in the experiments are introduced. The short-time Fourier transform and the orthogonal-like Gabor transform as applied to the ultrasonic echo samples are discussed in detail. The detection of peak frequency from a distorted spectrum and the formation of an image are also

discussed. Finally the software used to control the entire system is briefly addressed.

§ I.3.2 Setup of the System

The ultrasound frequency domain imaging system used in the medical physics research laboratory of the Waikato University is shown in Figure I.3.1 by a block diagram. The entire system includes five modules, which are the ultrasonic pulse-echo transceiver for generating short ultrasonic pulses and receiving the echo signals, the signal digitizer for converting the analog echo signals into the digital samples, a phantom-moving controller to move the phantom in a water bath, the IBM[1] compatible personal computer (PC) for the data processing and the main controller of the entire system, and the image display unit used to display and print the images. All modules were controlled by the PC.

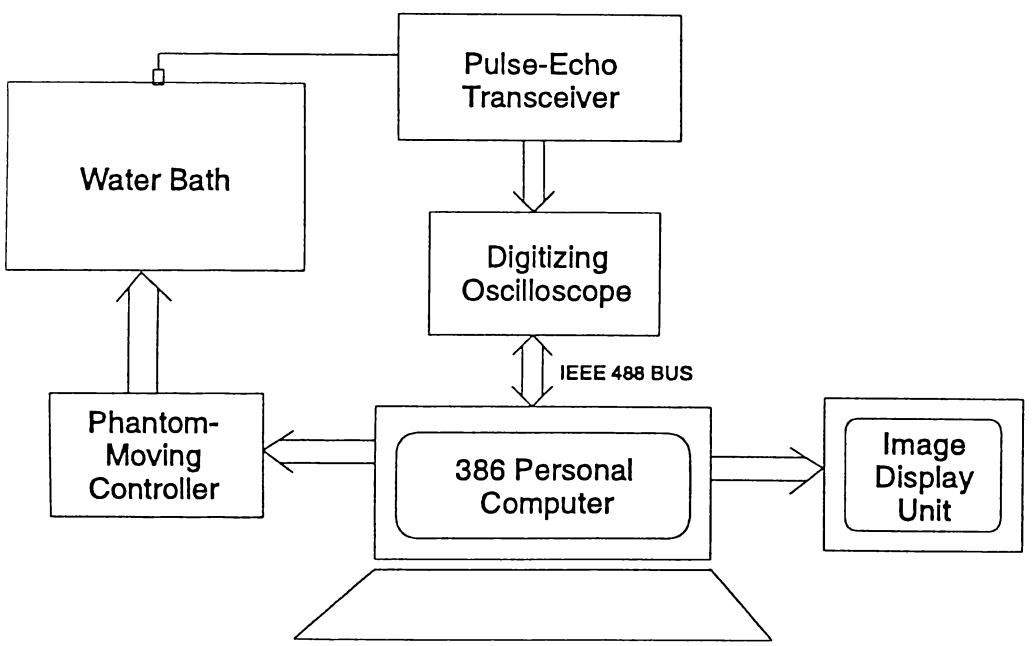


Figure I.3.1: A block diagram of ultrasound frequency domain imaging system

§ I.3.2.1 Ultrasonic Pulse-Echo Transceiver

The short ultrasonic pulses were generated by a 2.25 MHz medical transducer (model

---

1 --- International Business Machines Cooperation, PO Box 1328-C Boca Raton, Florida 33432, USA.

PICKER 595541) that was stimulated by the high voltage rectangular periodic pulses from an old commercial ultrasound A mode and B mode machine. The ultrasonic echo signals received by the same transducer were amplified using a modified electronic circuit in that machine. Also the time gain compensation (TGC) circuits in that machine were used to adjust the difference in ultrasound pulse intensities in the near and the far fields with respect to the transducer. To avoid saturation of the transceiver's amplifiers by strong ultrasonic echo signals, a resistance attenuator was used in combination with the TGC. The amplified ultrasonic echo signals were not rectified as is usually done in the A mode or B mode display in order to keep the radio frequency information in the received echo signals.

§ I.3.2.2 Signal Digitizer

An HP[1] 54501A digitizing oscilloscope was used as the ultrasonic echo signal digitizer. This digitizing oscilloscope has a maximum sampling rate of 10.24 MHz and maximum on-board memory of 1 kB. Also, the digitizing oscilloscope has a 10-bit precision for A/D conversion. The short ultrasonic pulses were generated by using the high-voltage periodic pulses to stimulate the transducer. The period of the pulses was long enough (about 2 ms) to let the machine receive the echo signals from a wide range of distances. The digitizer was externally post-triggered by the same pulses. The triggering delay depended on the distance from the transducer to the region of interest (ROI).

The digitized ultrasonic echo samples were first stored in the oscilloscope on-board memory. To reduce the random noise in the received echoes, the echoes on a single line were digitized four times. Those digitized ultrasonic echo samples were then averaged and the DC offset in echo samples was removed. The samples were finally transferred to the PC through a standard IEEE-488 bus.

§ I.3.2.3 Phantom-Moving Controller

To make a cross-sectional image of the phantom using a single transducer, it is

---

1 --- Hewlett Packard Company, PO Box 2197, Colorado Springs, Colorado 81901-9959, USA.

necessary to move either the phantom or the transducer step-by-step in the transverse direction. In this system, the transducer was fixed on one side of the wall of a large water bath and the phantom to be scanned was mounted on a gantry that can be moved in three dimensions using three individual step motors. The motors were controlled through the I/O ports on a MetraByte[1] PIO12 parallel card plugged in the PC. The phantom to be scanned was free to move in the water and its movement was totally controlled by the PC.

§ I.3.2.4 IBM compatible personal computer (PC)

An IBM compatible 80386 personal computer (PC) was used for the data processor and as well as the main controller of the entire system. To collect ultrasonic echo signals in each scanning line, the PC first issued a set of commands to the digitizer to make the digitizer ready to acquire echo signals. As soon as the trigger signal was available and a certain delay time was met, the digitizer digitized the amplified analog echo signals into its on-board memory. As described earlier, the echo signals on the same scanning line were digitized four times and averaged to reduce the random noise. Then the PC brought the averaged voltage samples back to its random access memory (RAM) through the IEEE-488 bus. The total time took only a few hundreds of milliseconds depending on the number of samples. Before collecting the echo signals in the next scanning line, the PC had to inform the phantom-moving controller to move the phantom to a new position. This was done by sending some commands to the phantom-moving controller via a number of digital I/O ports on the MetraByte PIO12 parallel card.

The voltage data stored in the PC RAM, which represent the received ultrasonic echoes were then ready to be Fourier transformed or Gabor transformed. In the early stages of the investigation, the Fourier transform was implemented using the fast Fourier transform (FFT) on an Array Processor Board (Model Number APB-3264AT)[2]. In view of the time taken in transferring data to and from this board, the

---

1 --- MetraByte Corporation, 440 Myles Standish Blvd., Taunton, MA 02780, USA.

2 --- Marinco Company, 10975 Torreyana Rd., SanDiego, CA 92121, USA.

FFT was later implemented in software and so was the Gabor transform.

The details of implementation of the short-time Fourier transform and some algorithms used in it are discussed in the next section.

After Fourier transforming or the Gabor transforming the sampled data, the peak frequencies in the spectra of echo samples at a series of specified time intervals were detected. Those detected peak frequencies in a series of spectra (or spectrograms) would be mapped to the pixel values in an ultrasonic frequency domain image.

§ I.3.2.5 Image Display Unit

The image display unit was rather simple using a just frame store that was plugged into the PC. The peak frequencies detected were finally mapped into an 8-bit colour image. The colour scale was designed to simulate a temperature-like colour range, red representing the lowest frequency and white the highest frequency.

§ I.3.3 Phantoms

To find the peak frequency shifting in the spectrum of ultrasonic echo signals backscattered from the small targets whose dimension or diameter is less than the wavelength of the ultrasonic pulses, a number of simple phantoms similar to the fine fibres in human body were prepared and used in the experiments.

One of the simple phantoms was made of fine copper wires. The dimension of wires was about 0.5 mm that is less than the wavelength of the ultrasonic pulses (0.67 mm). The wavelength of the ultrasonic pulses can be calculated using the equation in (I-3-1) (Kuttruff, 1993).

$$\lambda = \frac{c}{f} \qquad \text{(I-3-1)}$$

where c is the sound speed in the water, about 1500 ms^{-1} and f is the frequency (2.25 MHz) of the short ultrasonic pulses generated by the transducer. The wires were

about evenly distributed within a region of 45 mm long and 50 mm wide. The arrangement of wires is shown in Figure I.3.2. The scanning was taken from the left to the right and the transducer was moved from top to bottom.

Another simple phantom consisted of the grooves in a perspex block. The profile of those grooves in a perspex block is shown in Figure I.3.3. Each groove has two sharp edges from which the higher frequencies in the pulses are expected to be detected. The scanner was placed over the grooves and moved cross them. The final image is a cross section of all grooves.

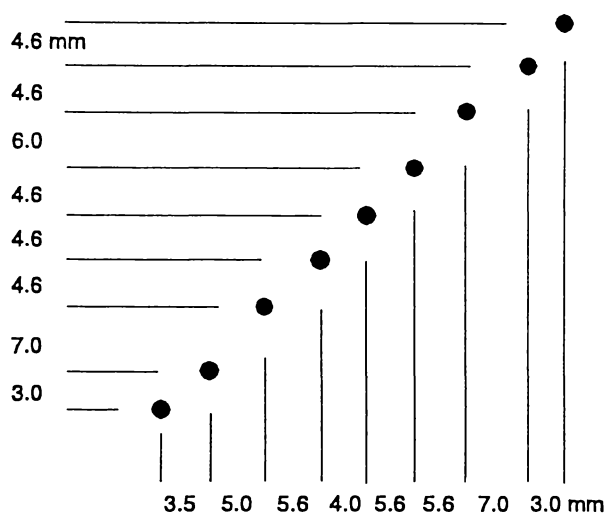


Figure I.3.2: Arrangement of wires

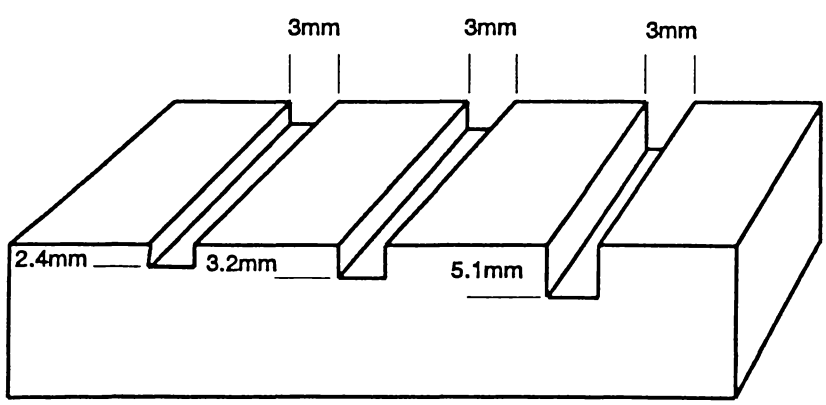


Figure I.3.3: Profile of grooves in a perspex block

§ I.3.4 Implementation of the Short-Time Fourier Transform

As described in I.2.3, a short-time sliding window was employed to move along each scanning line. Only echo samples observed within this window were taken in the discrete Fourier transform.

§ I.3.4.1 Leakage Error

Given a sequence of ultrasonic echo samples acquired in each scanning line, a short-time sliding window was moved from the beginning of those samples to the end. Every time this window made a shift of the same time interval. This operation is already shown in Figure I.2.4.

In theory, the discrete Fourier transform considers the data sequences to be periodic. In practice, the data sequences extracted from the above window are truncated at their end points. This kind of discontinuity often causes spectral leakage error. That means a given spectral component will be observed at another frequency. Such as a bias in frequency caused by the leakage is bothersome for the detection of small signals in the presence of nearby larger signals. It is especially true for the detection of smaller backscattered echo signals that are embedded in the larger reflected echo signals. To reduce the leakage error, it is common to multiply the data by one of the well-known window functions.

§ I.3.4.2 Window Functions

In fact, the above-mentioned short-time sliding window used to extract the echo samples is a rectangular (Dirichlet) window that is defined as

$$w_k = 1, \quad k = 0,1,2,\ldots,N-1 \ . \tag{I-3-2}$$

The transform of this window is the Dirichlet function, which has a mainlobe width of two frequency intervals ($2\Delta f$) and a first sidelobe level approximately 13 dB down from the mainlobe. The sidelobes fall off at 6 dB per octave (Harris, 1978).

A number of classic windows functions have been defined. Of them the Hanning

window and the Hamming window are most well-known and commonly used. The Hanning window is defined in (I-3-3) and shown in Figure I.3.4.

$$w_k = 0.5*(1.0 - \cos\frac{2\pi k}{N}), \quad k = 0,1,2,\ldots,N-1 \qquad \text{(I-3-3)}$$

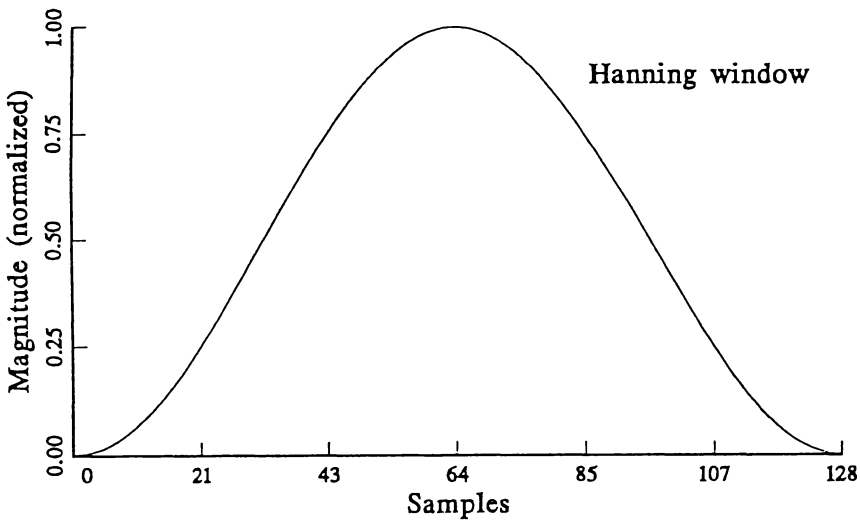


Figure I.3.4: Hanning window

The Hamming window is in fact not much different to the Hanning window. Its definition is expressed in (I-3-4) and the shape is shown in Figure I.3.5.

$$w_k = 0.54 - 0.46\cos\frac{2\pi k}{N}, \quad k = 0,1,2,\ldots,N-1 \qquad \text{(I-3-4)}$$

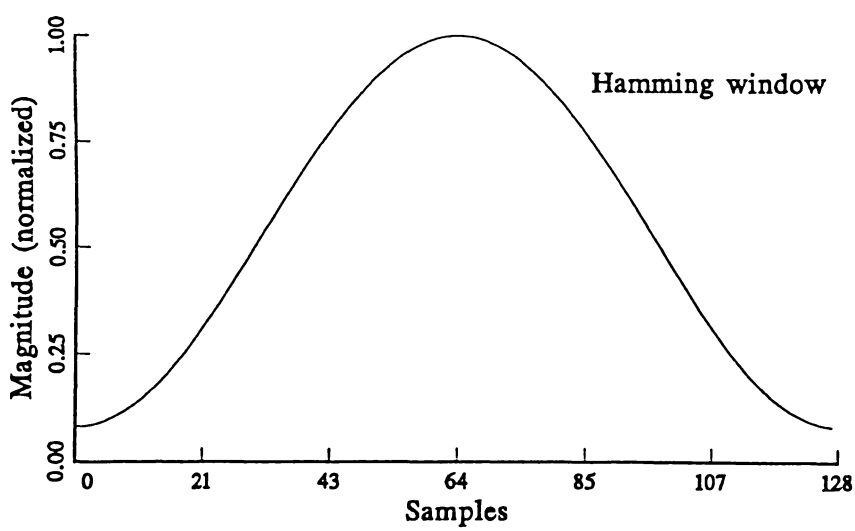


Figure I.3.5: Hamming window

Both Hanning and Hamming windows have lower level first sidelobes compared with the rectangular window. Assume the mainlobe is 0 dB and then the first sidelobe level in Hanning is -32 dB and in Hamming is -43 dB as shown in Figure I.3.6 and Figure I.3.7.

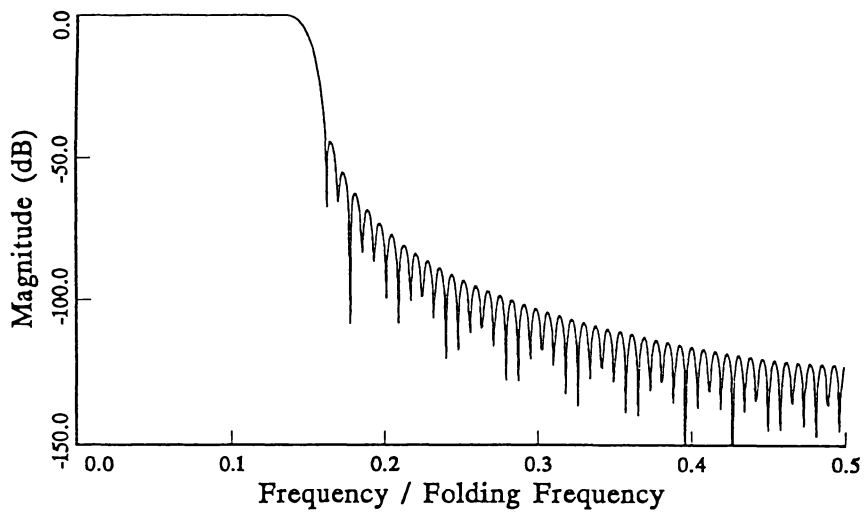


Figure I.3.6: Hanning window impulse response

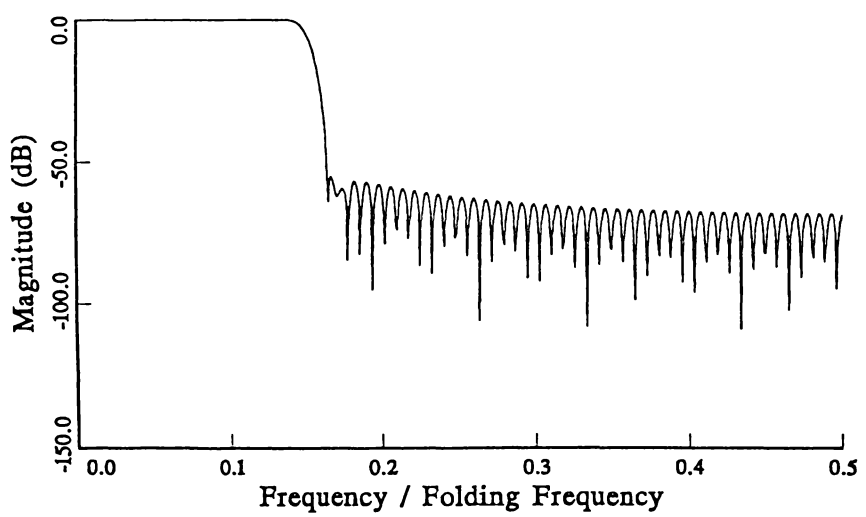


Figure I.3.7: Hamming window impulse response

Both Figure I.3.6 and I.3.7 give the complex gain at the frequency that is a fraction of the folding frequency (half sampling frequency), but the Hamming window has the same asymptotic rate of falloff of sidelobes as the rectangular window. The

Hanning window has a rate of -18 dB/oct that is three times faster than the other two windows. In consideration of these facts, the Hanning window was selected in the short-time Fourier transform.

§ I.3.4.3 Spectrum Resolution

The resolution of a spectrum is defined as the discrete frequency interval Δf and is determined by the reciprocal of total samples in the discrete Fourier transform. The more samples that are used, the higher the resolution of the spectrum will be. In the short-time Fourier transform, however, the number of samples collected from each short-time sliding window is normally not enough to generate a high resolution spectrum. To solve this problem, it is common to artificially pad a number of zero samples before and after this short-time window. Finally, the data to be Fourier transformed in each short-time sliding window is of the form:

$$u_i = \sum_{i=-\frac{N}{2}}^{\frac{N}{2}} h_i w_i s_i \qquad h_i = \begin{cases} 0 & \text{if } |i| \geq \frac{M}{2} \\ 1 & \text{if } |i| < \frac{M}{2} \end{cases} \tag{I-3-5}$$

where, M is the window width that is much smaller than the total data length N. The actual sample s_i is meaningful only within the window w_i.

The resolution of a spectrum for a given number of samples M extracted from a short-time sliding window can now be improved by artificially padding zero samples on the original echo samples. In my experiments, zero were padded onto both outsides of every short-time sliding window as shown in (I-3-5). Consequently, the total number of data N being Fourier transformed became much larger than the number of samples M taken from each short-time sliding window. Of course, N cannot be unconditionally increased otherwise it will contain less information about the echo signals but also will take a longer time to compute the discrete Fourier transform. In the implementation of software for STFT, N = 1024 was used.

§ I.3.4.4 Axial Resolution of Image

The idea of using a short-time sliding window is to extract a block of echo samples

along each scanning line and find the peak frequency in its spectrum. Then the peak frequency is used to represent a pixel value at the time corresponding to the middle of window in the final image. In this way, the image axial resolution in every scanning line is determined by the number of short-time windows used along that scanning line. The window width M must be wide enough to cover the rapidly changing frequency components in time-varying ultrasound echo signals. In general, for higher frequency ultrasound pulses, which are sampled at a higher sampling rate, a narrower window can be used.

From the other point of view, a short-time sliding window is moved along the scanning line to extract the echo samples. The smaller time interval shifted by the window each time means that more windows are used on single scanning line. However if the window shifting time S in samples is too smaller then there is no significant change of the frequency components in the adjacent windows. Consequently this does not improve the image axial resolution on a single scanning line but increases the time for calculating the spectra of echo samples extracted from those windows.

Ideally, the signal covered by the short-time window should be more or less stationary at any time interval (Cohen, 1989). In practice, however, it is impossible to find such a window suitable for any time-varying signals. From my experience in selecting the window width M and the shifting time S, I have found that if a complete waveform of 3 - 4 ultrasonic cycles is extracted by the window then the spectrum will more truly represent the time-varying frequencies. Of course the window shifting time may be any value, but the time-varying frequencies would not be changed too much if the window shifting time is no more than one cycle (i.e., about one fourth of a complete pulse). For the transducer used in my experiments, which has a nominal frequency of 2.25 MHz, this means that M must be greater than 1.78 μs and S must be no less than 0.45 μs. After a number of tests on the combination of M and S, I have found the best solution was $M \approx 4$ μs and $S \approx 0.8$ μs. Using the digitizer with a sampling rate 10 MHz, about forty samples were extracted from that window and the window was shifted about eight samples each time.

§ I.3.5 Implementation of the Orthogonal-Like Gabor Transform

The discrete orthogonal-like Gabor transform was implemented by the National Instruments LabVIEW software. Compared to the short-time Fourier transform, the time and frequency intervals ΔM and ΔN are normally not equal to one because of the use of the pseudo Wigner-Ville distribution.

To use the orthogonal-like Gabor transform, one has to balance the time and frequency resolutions by selecting appropriate ΔM and ΔN according to the specified window width L. The sampling condition $\Delta M \Delta N \leq L$ must be satisfied. The condition $\Delta M \Delta N = L$ is called the critical sampling.

The results are varied with different input signals. In practice, the best resolution for the given echo signals was obtained by testing the different combination of ΔM and ΔN for a chosen L. The final frequency domain images constructed using the Gabor transform and the short-time Fourier transform were compared and results are discussed in the next chapter.

§ I.3.6 Spectral Analysis

To construct a frequency domain ultrasonic image based on the peak frequencies, the spectrogram (or a series of spectra) obtained from a data sequence collected from every scanning line must be analysed to find out the peak frequencies. But the echo signals contain lots of noise so that the Gaussian-shape is seriously distorted in some spectra. Consequently, the desired peak frequencies become hard to detect in those spectra.

One solution is to use a threshold to ignore the spectra generated mostly by low-level noise. The threshold is automatically based on a pre-determined percentage of the maximum intensity of echo signals collected in each scanning line. This of course will cause some small echo signals to be ignored. Another helpful solution is to set a narrow frequency window for the desired peak frequencies. Any peak frequencies outside this frequency window are assumed to come from noise because the frequency shifting is expected within a small range as shown in (I-2-4) in theory.

The above two solutions were both used in my experiments to detect the desired peak frequencies. If only the narrow frequency window is used, a 'pure' frequency domain ultrasound image is obtained otherwise a new type B mode frequency domain image is formed. The experimental results have shown the efficiency and the effectiveness of these two methods.

§ I.3.7 Image Formation

The peak frequency detected in each spectrum is then mapped into a grey level for display on a monochrome monitor or into three prime colour values if displayed on a colour monitor. A range of 256 grey levels was selected after considering the limitation of most current display monitors. To increase the visibility of the proposed frequency shifting in the spectrum of ultrasonic echoes backscattered from small targets, an estimated frequency range was used in mapping according to the actual frequency of the transducer used. This range was set 2 MHz to 2.5 MHz for the transducer PICKER 595541 with a nominal frequency of 2.25 MHz. The mapping is linear in this range with 2 MHz mapped to 0 and 2.5 MHz to 255.

To transfer a grey level into a colour in the smoothly-changed temperature-like colour scale (red-orange-white), a non-linear mapping was used based on the triangle inside the horseshoe-shaped (or tongue-shaped) colour diagram shown in Figure I.3.8. The colours change smoothly from one region to the other. Although the diagram illustrates the range of colours visible to the human eye, only the colour range inside the triangle can be reproduced by the video colour monitor using three colour primaries red, green and blue, which are indicated by three vertices.

Colour points are labelled along the curve in Figure I.3.8 according to colour wavelength in nanometres. Assuming A, B, and C are the three colour primaries and x, y and z are the amount of each component contributed in the final colour. Then the equations shown in (I-3-6) indicate that only two variables (x and y) for the amount of colour components are needed and third one (z) can be easily calculated out from the others.

$$x = \frac{A}{A + B + C}$$

$$y = \frac{B}{A + B + C} \qquad \text{(I-3-6)}$$

$$z = \frac{C}{A + B + C}$$

$$x + y + z = 1$$

In the design of a temperature-like colour scale (red-orange-white), the amount of component for each colour primary was determined according to the above horseshoe-like diagram and the basic equations in (I-3-6) plus some correction coefficients for human eye to the colour primaries.

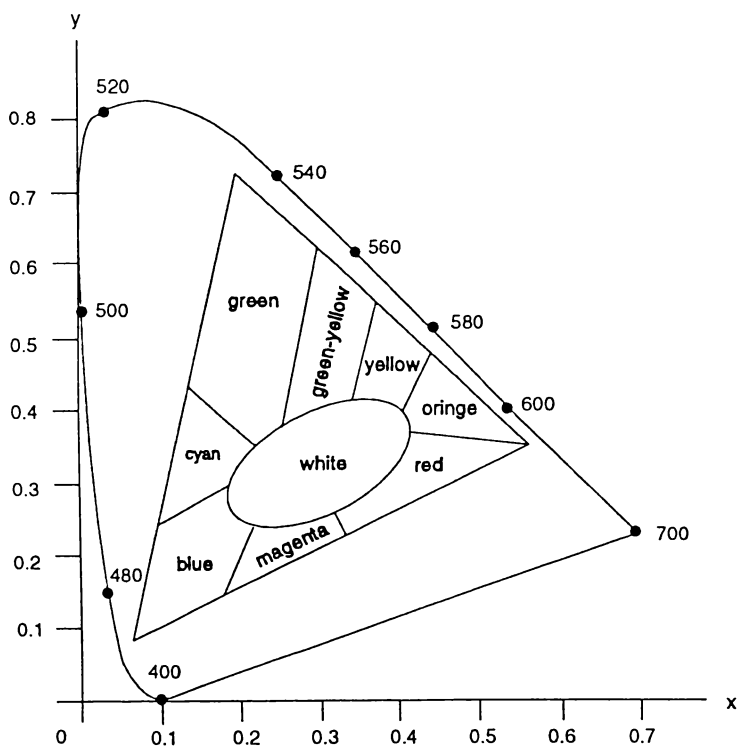


Figure I.3.8: Horseshoe-shaped colour diagram (Whittaker, 1993)

§ I.3.8 Software

The entire ultrasonic frequency domain imaging system needs the software to drive

and control. The software was designed and implemented in a number of modules which are the same as those shown in the system block diagram in Figure I.3.1. For example, the software used to control the HP 54501A digitizing oscilloscope to acquire echo samples was kept in the module named 'HP'. In this way, it is easy to maintain and update any part of the software without affecting others.

Every module was kept in a separate file and coded in the C programming language. The final program was compiled using the Microsoft C compiler Version 5.1 and run under the MS-DOS on IBM compatible 80386 personal computer.

PART I CHAPTER 4

EXPERIMENTAL RESULTS AND EVALUATIONS

§ I.4.1 Introduction

Simple test phantoms shown in figures I.3.2 and I.3.3 were scanned in the way described in the last chapter. Several two-dimensional (2-D) images that represent cross-sections of the test phantoms were then constructed by using the previously-described ultrasound frequency domain imaging system. Those images were based on the peak frequencies detected from a series of spectra (spectrograms) of the received ultrasonic echo signals. The spectrograms can be generated using either the short-time Fourier transform or the orthogonal-like Gabor transform. In my experiments both transforms were used. The purpose of doing so was to find out which transform can provide the better resolution for the ultrasound frequency domain images.

Based on the detected peak frequencies, two kinds of frequency domain images were built and shown in this chapter. The 'pure' frequency domain ultrasound images are purely based on the peak frequencies of echo spectrograms regardless of any information in the time domain. The new type B mode frequency domain ultrasound images show only the peak frequencies of echo spectrograms when the corresponding echo intensities in the conventional B mode ultrasound images are over a pre-defined threshold.

To compare the short-time Fourier transform with the orthogonal-like Gabor transform, a number of sliding windows with different widths were used in both transforms. Also, a narrow frequency window described in §I.3.6 was always used in order to get rid of the unwanted peak frequencies from noise. The images made from the short-time Fourier transform are called the Fourier images and the images made from the orthogonal-like Gabor transform are called the Gabor images. For comparison, both Fourier image and the Gabor image of the same phantom built

under the similar conditions are printed within one picture as well as the conventional B mode image of this phantom.

§ I.4.2 Images of Wires

The phantom of wires shown in Figure I.3.2 was transversally scanned by a single transducer (PICKER 595541). The received echo signals on each scanning line were then both Fourier transformed and Gabor transformed. In both Fourier and Gabor transforms, a sliding window of the same width was used. In the Fourier transform, this window was shifted a certain distance in time on each scanning line in order to obtain successive pixels in the final image. While in the Gabor transform, the equivalent to the same shifting time as in the Fourier transform was selected as the time sampling interval.

The desired peak frequencies found in a series of spectra (or spectrograms) of echoes were assumed to be within a narrow frequency window with the range of 2.25 ± 0.25 MHz (where 2.25 MHz is the nominal frequency of the PICKER 595541 transducer used). This range was wide enough to cover any possible frequency shifting that was mentioned in the second chapter. In the experimental results presented by Round, the maximum shifting was 100 kHz for a transducer with nominal centre frequency 1.9 MHz. That means that the maximum shifting was about 5.25% of the centre frequency. In my experiments, the maximum frequency shifting was assumed to be approximately 11% of the centre frequency on both sides of the centre frequency although no frequency down shifting was expected in the theory described in chapter two. Consequently any peak frequency was considered unusual or coming from noise and then ignored if it was found outside this narrow frequency window. If only the narrow frequency window is used to select the desired peak frequencies without thresholding based on the intensities in the conventional B mode image, a 'pure' frequency domain ultrasound image is obtained.

A threshold that was equal to 20% of the greatest brightness on each scanning line in the conventional B mode image was also used in the way as described in §I.3.6. Using the thresholding method eliminates the influence of any low-level noise so that

the selected spectra more truly represent the frequency characteristics of the ultrasonic echo signals. However the final images partly rely on the informatio in the conventional B mode images. This kind of image is called the new type of B mode frequency domain images because those images contains both time domain and the frequency domain information. It gives a better way to illustrate the backscattering characteristics of scanned objects without the influence of lower level noise. Therefore, it will probably have more diagnostic value in the future.

The peak frequencies detected within the narrow frequency window regardless of using a thresholding method or not were then mapped into the pseudocolour codes in a temperature-like colour scale. Finally a 2-D frequency domain image in pseudocolour was generated and printed out.

The width of the sliding window used in both transforms was found to have great effect on the axial resolution of 'pure' frequency domain ultrasound images. A few of the different sliding windows in width were used. The window width was measured by the number of samples in a discrete signal. For the phantom of wires, 512 samples on each scanning line were collected at the sampling rate of 10 MHz. Both 'pure' frequency domain Gabor and Fourier images built using a sliding window with the width of 128 and 64 samples are shown in Figure I.4.1 and Figure I.4.2 respectively. In the Fourier transform, the sliding window was shifted for eight samples each time and in the Gabor transform the time sampling interval of eight samples was used.

The wires are clearly seen in the Gabor and the Fourier images as well as in the B mode image. Generally the higher frequencies are detected when the wire is in the centre of the beam and the frequencies become lower when the wire is positioned close to the beam edges. Also the Fourier images of wires clearly show the effect of the window width on the axial resolution of images although the Gabor images of wires are not so sensitive to the window width. For the Fourier images of wires, the narrower the window is, the higher axial resolution will be achieved. As the axial resolution improves, the 'resonances' behind the wires, easily seen in the Gabor

images, start to appear in the Fourier images.

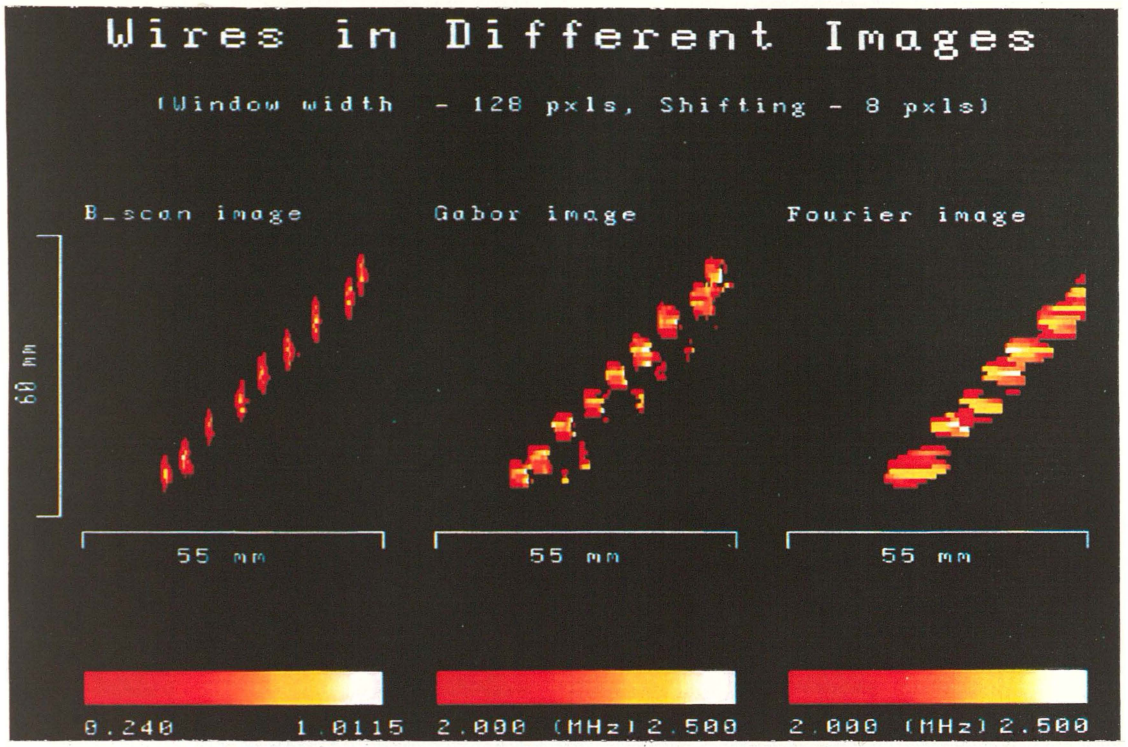


Figure I.4.1: 'Pure' frequency domain wire images using a window of 128 samples (please refer back page I.3.6 for the scanning direction)

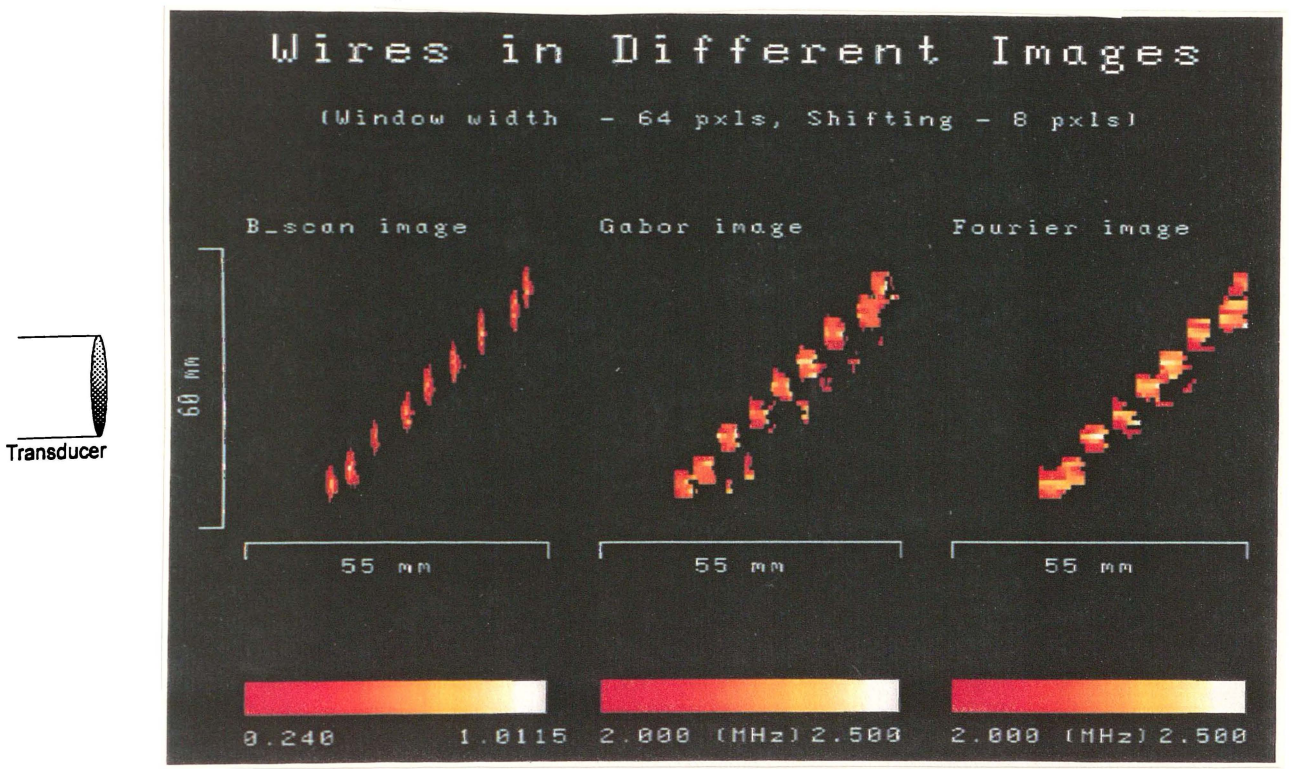


Figure I.4.2: 'Pure' frequency domain wire images using a window of 64 samples (please refer back page I.3.6 for the scanning direction)

The axial resolution of the Fourier images of wires can be further improved by carefully selecting an appropriate short-time sliding window. As described in §I.3.4.4, a short-time sliding window with forty samples wide was used in my experiments. As a result, the axial resolution in Fourier image of wires was apparently improved. The improved 'pure' frequency domain Fourier image of wires is shown in Figure I.4.3 with the similar Gabor image that has the highest axial resolution in the experiments. It should also be noted that the lateral resolution is slightly better in the Gabor image even though the axial resolution is slightly worse.

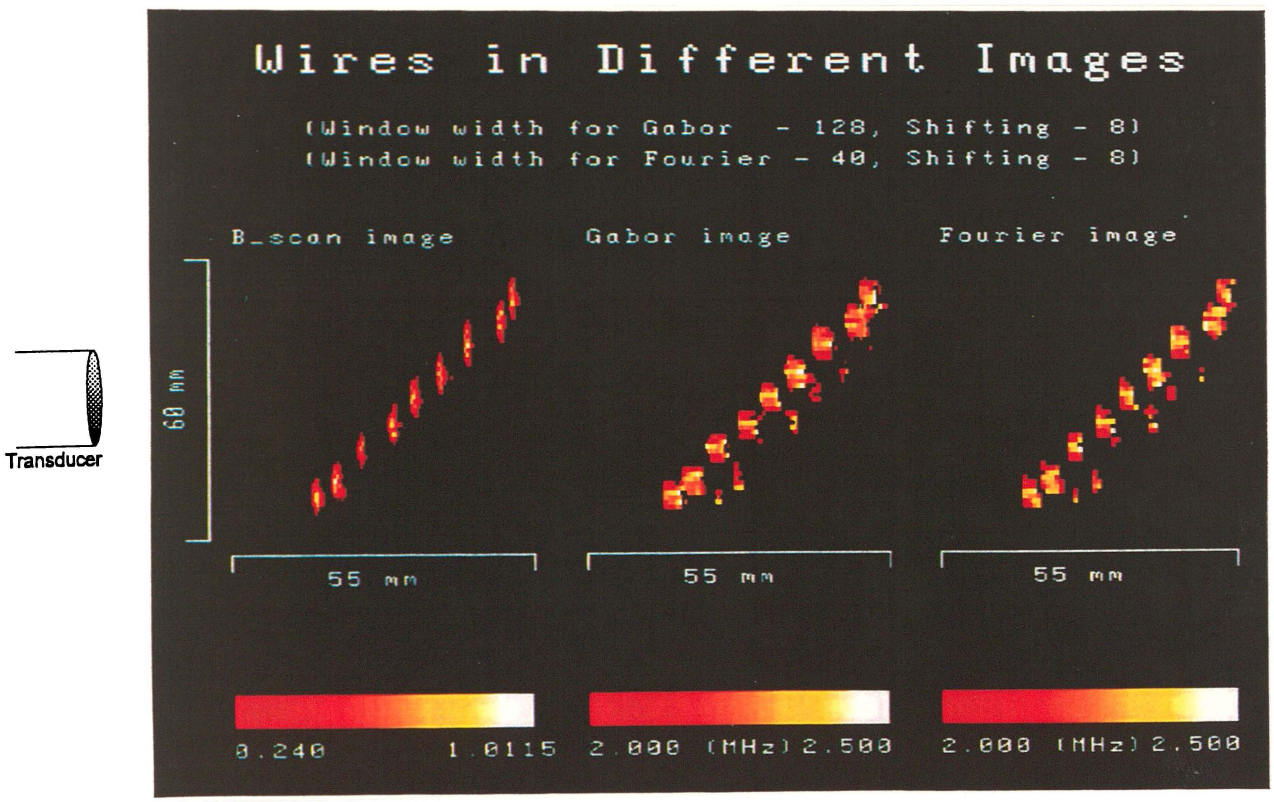


Figure I.4.3: Improved 'pure' frequency domain Fourier image of wires using a short-time sliding window of 40 samples
(please refer back page I.3.6 for the scanning direction)

The thresholding method described previously was then used in combination with the narrow frequency window. Consequently, the new type B mode frequency domain images of wires are shown in Figure I.4.4.

In comparison with the 'pure' frequency domain images of the wires, the new type B

* The reverberations seen on Figures I.4.1-4 are possibly caused by the multiple reflections in the front layers of the transducer or between the front surface and the backing material of the transducer.

mode frequency domain images present not only the information of peak frequencies in time-varying echo signals but also give a better representation of the size of the scanned wires, especially improving the axial resolution. Therefore, the new type B mode frequency domain images probably have more diagnostic value in the future. In addition the Gabor image shows some reverberations behind the wires that are not seen in the other images.*

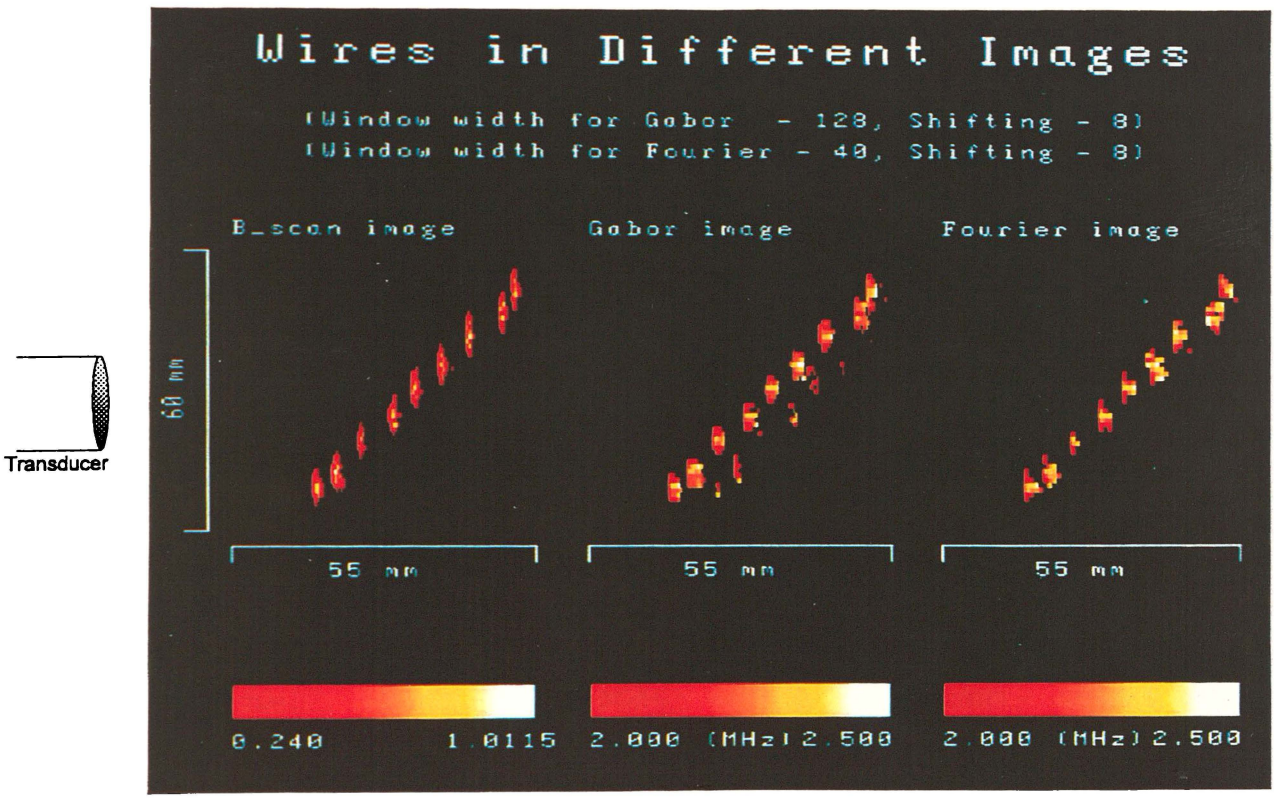


Figure I.4.4: New type B mode frequency domain images of wires (please refer back page I.3.6 for the scanning direction)

§ I.4.3 Images of Grooves on Perspex Surface

As with the wires, the grooves on the perspex surface were scanned across by the same transducer. The echo signal was sampled at the sampling rate of 10 MHz and the 256 samples on each scanning line were collected. Those echo samples were then both Fourier transformed and Gabor transformed respectively to produce a series of spectra (spectrograms) wanted.

The short-time sliding windows with 128 and 64 samples wide were used in the

Fourier and Gabor transforms respectively. Sliding window was shifted eight samples each time in the Fourier transform. Similarly, the time sampling interval of eight samples was used in the Gabor transform.

The 'pure' frequency domain Gabor and Fourier images constructed using the sliding windows with 128 and 64 samples wide are shown in Figure I.4.5 and Figure I.4.6 separately.

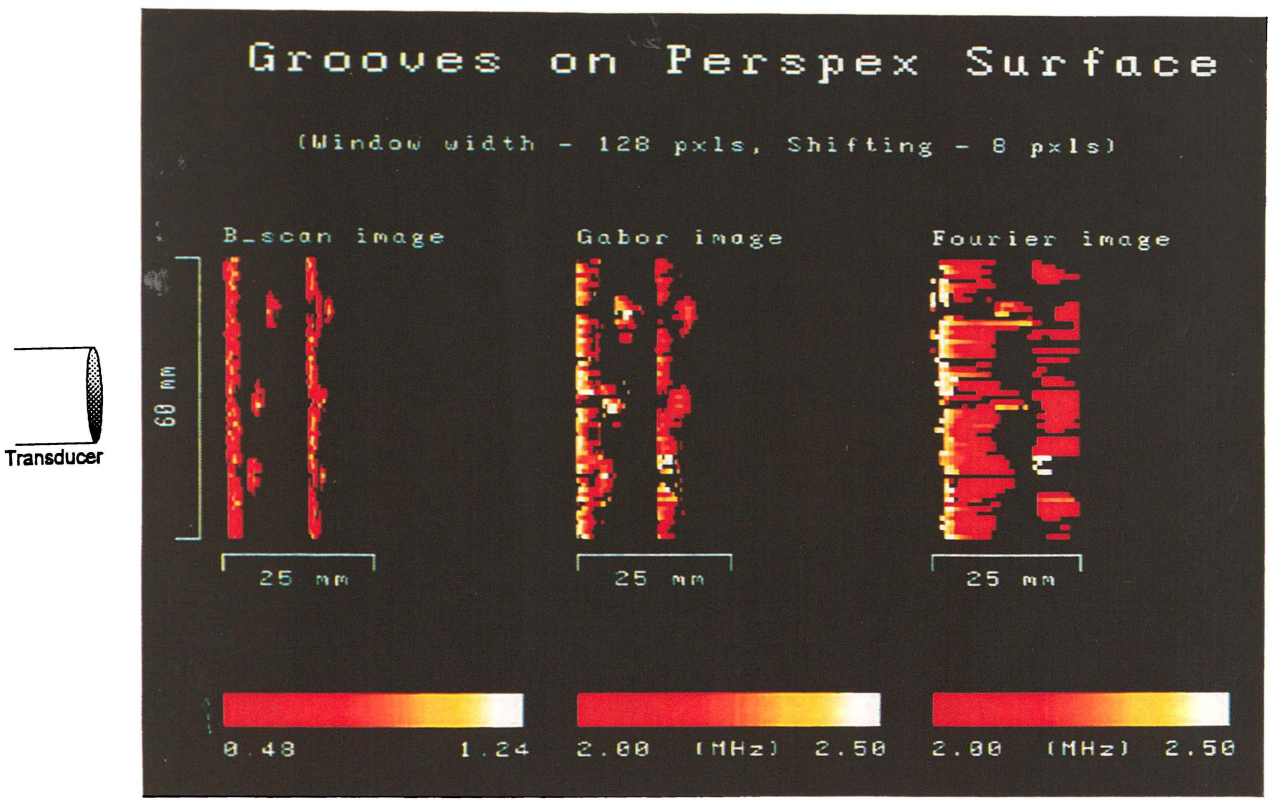


Figure I.4.5: 'Pure' frequency domain groove images using a short-time sliding window of 128 samples (please refer back page I.3.6 for the scanning direction)

It is interesting to consider the peak frequencies of the echoes off the flat perspex surface between the grooves. These clearly show that the frequencies of the leading edge of the pulse are higher than those at the trailing edge. They are about 2.5 MHz at the leading edge and about 2.0 MHz at the trailing edge with the mean frequency, 2.25 MHz, being the nominal frequency of the transducer.

* Due to the frequency dependent absorption, the intensity and the centre frequency of the spectrum of echoes are both decreased. The centre frequency f_x can be calculated using the following equation (Round et al., 1987):

$$f_x = \frac{f_c - 8g\sigma_c^4\alpha_i x}{1 - 8e\sigma_c^2\alpha_i x}$$

where, f_c and σ_c are the centre frequency and bandwidth of the spectrum of backscattered echoes, which should be same as the original pulse because the back surface of perspex is a perfectly reflecting plane. Usually the bandwidth is about 10-20% of the centre frequency under the Gaussian assumption. α_i is the intensity attenuation coefficient and x is the depth of the object to be measured. g and e are also given in the same reference:

$$g = \frac{n}{2}(2-n)f_c^{n-1}, \qquad e = \frac{n}{2}(n-1)f_c^{n-2}$$

where n is a exponent constant depended on the frequency.

Using the above equations, the centre frequency f_x of the spectrum of echoes from the back surface of the perspex block shown in Figure I.4.6 was calculated. The perspex was assumed to be similar to bone in ultrasound characteristics. For bone, n should be a little bit greater than unity when the frequency is above 2 MHz and α_i should be 3-4 $dBcm^{-1}MHz^{-1}$ (Wells, 1977). The thickness of the block is about 1.25 cm. On substituteing these values in the above equations it is found that for $\sigma_c = 0.12 f_c$ MHz, then $f_x = 2.03$ MHz when $f_c = 2.25$ MHz and $f_x = 2.17$ MHz when $f_c = 2.40$ MHz. Thus the frequency shift $\Delta f = f_c - f_x \approx 0.22$ MHz. The calculated results agree approximately with the colour change observed from the front to back surfaces of perspex in Figure I.4.5-8.

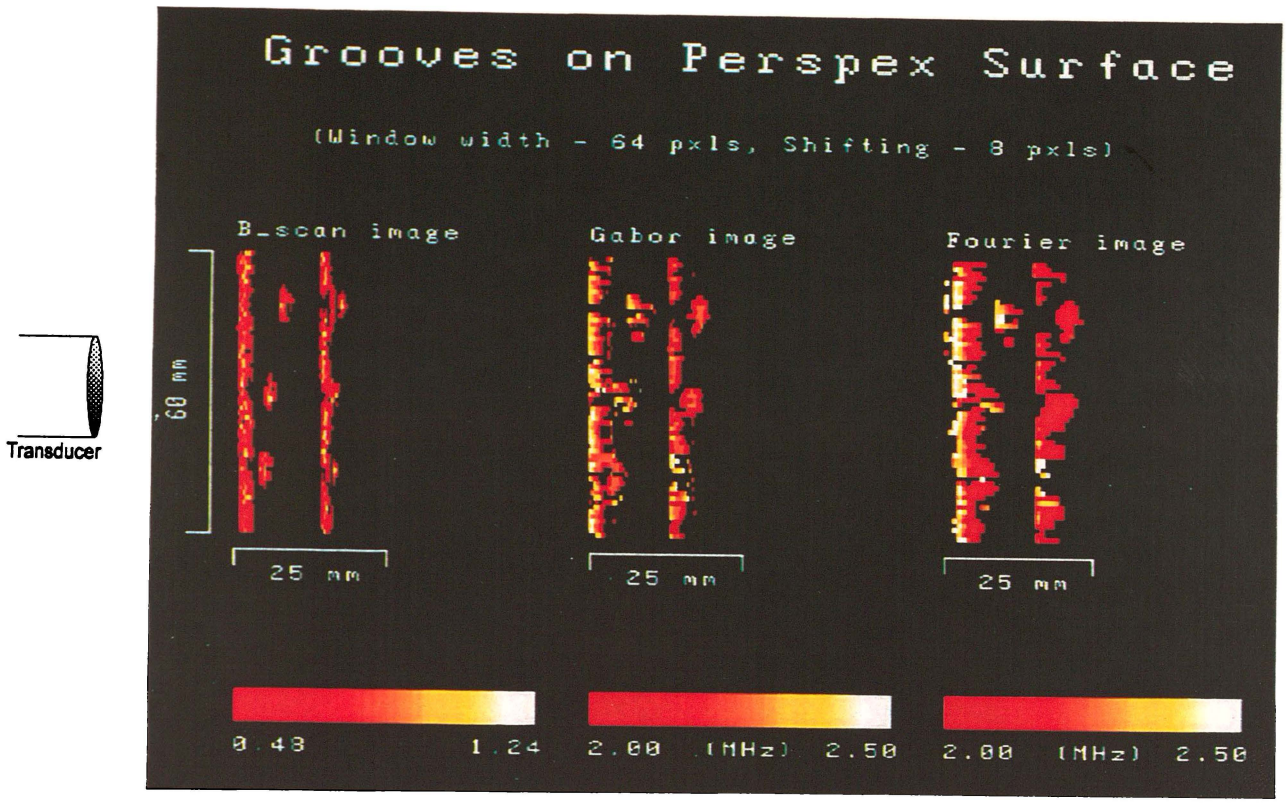


Figure I.4.6: 'Pure' frequency domain groove images
using a short-time sliding window of 64 samples
(please refer back page I.3.6 for the scanning direction)

Also note that the echoes from the back surface of the perspex block are at lower frequency than those from the front. This indicates the frequency dependent absorption of ultrasound pulse by the perspex phantom.*

The three 3-mm-wide grooves on the perspex surface that are not easily seen in the conventional B mode image are clearly seen in the Gabor image and possibly in the Fourier image as well. This further shows that the frequency domain images have the better lateral resolution than the conventional B mode image.

Again those groove images clearly show the effect of the short-time window width on the axial resolution of both Gabor and Fourier images although the Gabor groove images are not so sensitive to the window width. As the same as in the wire images, the narrower window is used, the higher axial resolution will be achieved for the

Fourier images of grooves.

The axial resolution of the Fourier groove images was further improved by using a short-time sliding window with forty samples wide. The improved 'pure' frequency domain Fourier image of grooves is shown in Figure I.4.7 with the similar Gabor groove image that has the best axial resolution in the experiments.

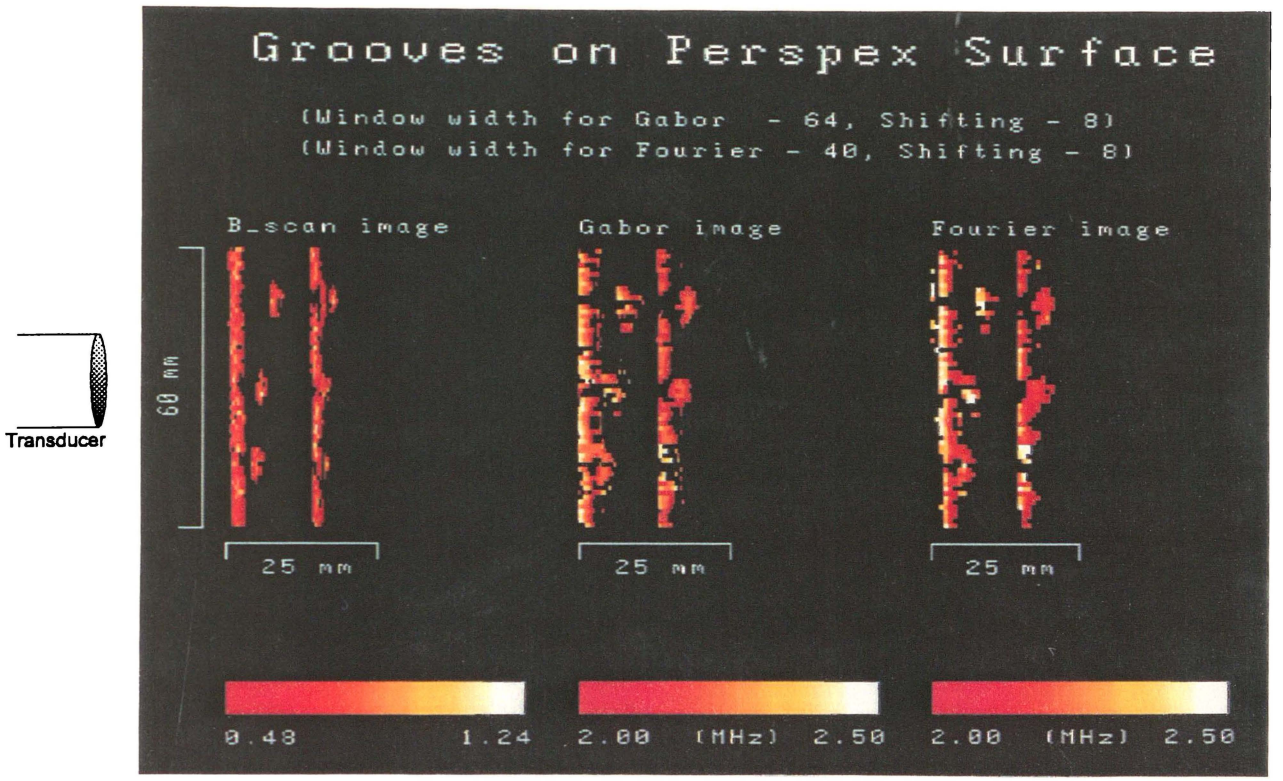


Figure I.4.7: Improved 'pure' frequency domain Fourier image of grooves using a short-time sliding window of 40 samples
(please refer back page I.3.6 for the scanning direction)

The previously-described thresholding method was then used together with the narrow frequency window to build the peak frequency based ultrasound image of grooves. Finally the new type B mode frequency domain images of grooves containing both time domain and the frequency domain information are shown in Figure I.4.8.

The axial and lateral resolutions in both Gabor and Fourier images of grooves are dramatically improved by using the thresholding method. Consequently three 3-mm-

wide grooves on the perspex surface that are not seen in the conventional B mode image are more clearly seen than before in both Gabor and Fourier images. This result again shows that the new type B mode frequency domain images have the better lateral resolution than the conventional B mode image for detecting the sharp edges close to each other.

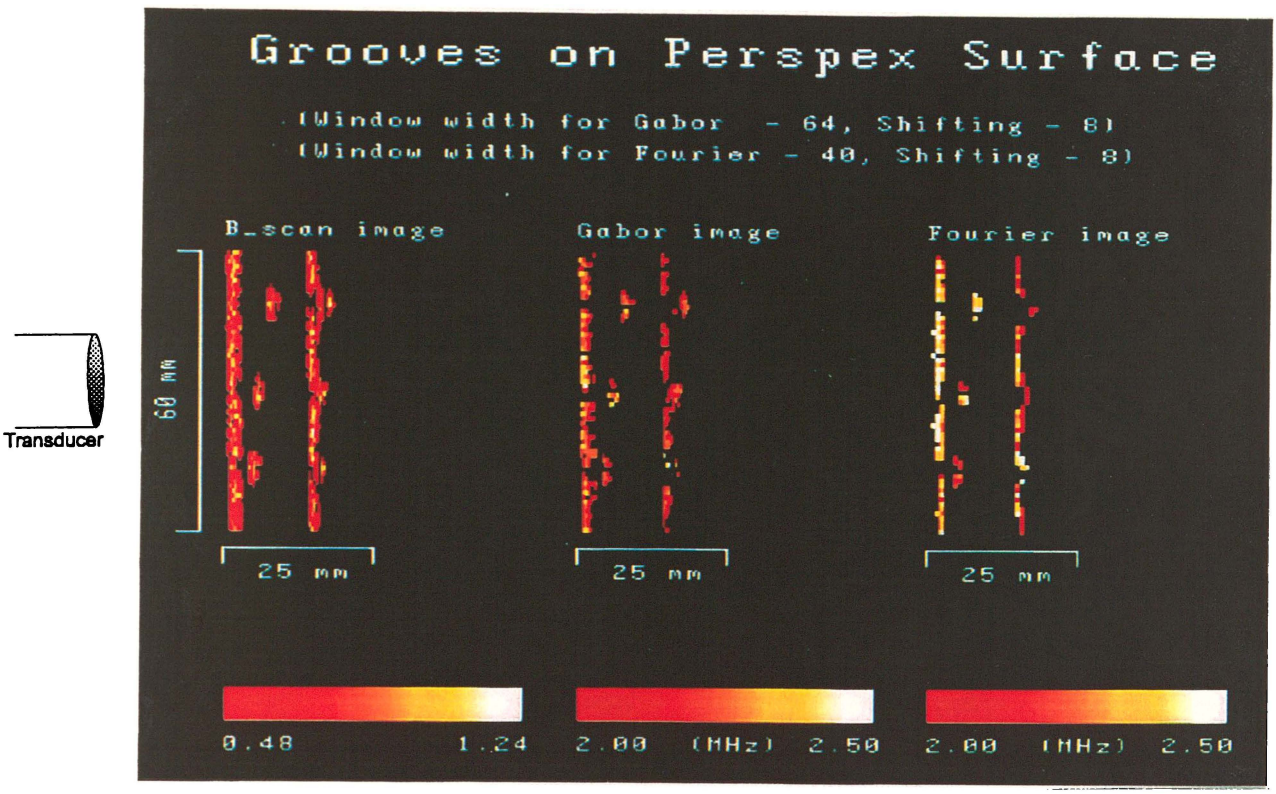


Figure I.4.8: New type B mode frequency domain images of grooves (please refer back page I.3.6 for the scanning direction)

§ I.4.4 Comparison of Results from Fourier and Gabor Transforms

Although both short-time Fourier transform and the orthogonal-like Gabor transform can be used to produce the spectrograms of time-varying ultrasound echo signals, the differences between them have been seen from the images shown above.

The results have shown that both transforms need a short-time window and an appropriate short-time window can improve the axial resolution of an image. For the Fourier transform, the axial resolution of an image will be different when using different short-time sliding windows. In general, the narrower the window is, the

higher axial resolution will be achieved. This has been shown in Figure I.4.1-3 and Figure I.4.5-7. In practical application it is not easy to find an appropriate window without experience. However, the Gabor transform is much more tolerant to the window width. This has been confirmed by the 'pure' frequency domain Gabor images of both wires and grooves built using different sliding windows. Therefore, the Gabor transform from the practical point of view is much easier to use than the Fourier transform.

In addition, the results have shown that the Gabor images of both wires and grooves have higher resolution than the similar Fourier images under the same conditions (i.e., the same sliding window and time shifting interval). This can be clearly seen in all 'pure' frequency domain ultrasound images of both wires and grooves.

In respect of computational speed, the Gabor transform is about ten times faster than the Fourier transform although the Gabor transform was run on a different workstation (Macintosh II-70).

The axial resolution of the Fourier images was further improved in the experiments by carefully finding an appropriate short-time sliding window. Also the improved 'pure' frequency domain Fourier image of both wires and grooves shown in Figure I.4.3 and Figure I.4.7 seemed to have higher resolution than the relative Gabor images that had the highest resolution in the experiments. These results do not mean that the Fourier images will have higher resolution than the Gabor images. The resolution of Gabor images could have been further improved as well by choosing an appropriate window. However, in the software package *Gabor Transform* I used, the Gabor transform was limited to the use of a number of fixed window widths.

In summary, the Gabor transform is easier to use in practice and can produce the better images than the Fourier transform under the same windowing conditions. In addition, Gabor transform costs less time in computation than the Fourier transform.

PART I CHAPTER 5

CONCLUSIONS AND SUGGESTIONS

§ I.5.1 Conclusions

During the past two decades, a number of researchers have used the frequency information of the reflected and/or backscattered ultrasound echoes in ultrasonic imaging and tissue characterization. Based on the theory of peak frequency shifting (Surridge, 1980; Round et al., 1987), I have used both short-time Fourier transform and the orthogonal-like Gabor transform to build a number of two-dimensional (2-D) 'pure' frequency domain ultrasound images and new type B mode frequency domain images for some simple phantoms. The 'pure' frequency domain ultrasound images were based only on the peak frequencies in echo spectrograms and the new type B mode frequency domain images were based not only on the peak frequencies in echo spectrograms but also on the information of echo intensities.

One phantom consisted of the copper fine wires, whose diameter was just less than the wavelength of the ultrasound pulses, and the other was made of a perspex block with several grooves on its top side. The spectrum of the short ultrasound pulses is assumed to have the Gaussian shape under the ideal condition, but the practical spectrum was distorted due to attenuation, scattering and absorption in medium and noise in electronic equipment and the environment. From the distorted spectra or spectrograms, the peak frequencies, which were considered as one of the frequency features in the Gaussian-shaped spectra, were extracted to construct the frequency domain ultrasound images.

The short-time Fourier transform and the orthogonal-like Gabor transform are two major methods to analyse the time-varying echo signals. For the purpose of comparison, both transforms were used under similar conditions to produce a series of spectra or spectrograms of ultrasound echo signals. From the experimental results, it has been shown that the short-time sliding window is an important factor in

determining the axial resolution of images and the Gabor transform is more tolerant to the width of that window. In addition the images constructed by the Gabor transform have higher axial resolution than those constructed by the Fourier transform under the same windowing conditions and the axial resolution of both Fourier and Gabor images can be improved by choosing the appropriate short-time sliding window.

It was also found from the experiments that the frequency domain images generally have better lateral resolution than the conventional B mode image although the axial resolution is degraded, which has been shown in the frequency domain images of both wires and grooves. This discovery indicates that using the frequency domain images can more easily show the objects that are close to each other in the direction perpendicular to the ultrasound beam scanning line.

The experimental result from the 'pure' frequency domain perspex images has shown that the echoes from the back surface of perspex block have lower frequency than those from the front. This frequency dependent absorption that is normally not seen in the conventional B mode ultrasound image can be easily seen from the frequency domain image.

The new type of B mode frequency domain images containing only peak frequencies of echo spectrograms that are selected according to a threshold of echo intensities was investigated. The experimental results have shown that the new type of B mode frequency domain images not only contained the frequency information of scattered targets but also clearly displayed the physical sizes of the scanned objects. Therefore ,this new type of B mode frequency domain images probably has more diagnostic value in the future.

§ I.5.2 Suggestions

Both 'pure' frequency domain ultrasound images and the new type of B mode frequency domain images shown in the last chapter were based on the peak frequencies detected in a series of spectra or spectrograms of echoes, but the peak

frequencies were affected by many factors in processing the received ultrasound echoes. Although a number of factors have been considered in my experiments, some others are discussed here as suggestions for any further consideration of research in this line.

a) The spectra of short ultrasonic pulses normally do not have an ideal Gausssian shape in practice and also are not same at different positions in the area scanned due to the nature of the ultrasound beam of transducer. It is well known that the effective centre frequency of an ultrasound beam may vary along its axis. That would affect the accuracy in detection of peak frequency shifting although the actual values of shifting were not used in my experiments.

   To explicitly know the time-frequency distributions of original short ultrasound pulses in the area scanned and find the centre frequencies corresponding to all different locations in time domain would give a good reference to judge whether the individual spectrum at different location comes from echoes or noise. The time-frequency distributions of original ultrasound pulses can previously be calculated from the ultrasound beam of a particular transducer, which could be measured from pulses reflected off a plane surface.

b) Since the constructed frequency domain ultrasound images will be heavily based on the frequency information detected from a series of spectra or spectrograms of echoes, any circuitry that is between receiving the reflected and/or backscattered ultrasound echoes and digitizing the amplified echoes should carefully be selected not to affect the desired spectrograms of echoes. Non-linear amplifiers and the time gain compensation (TGC) should be used with caution to avoid against any distortion. Frequency dependent absorption of the ultrasound echoes should also be investigated and compensated for if it is found to be a factor.

   Since this thesis was written, a new ultrasonic pulse-echo transceiver and a new digitizer have been installed in the system to replace the old commercial

ultrasound A mode and B mode machine and the HP 54501A digitizing oscilloscope respectively. It seems possible to take the above suggestions into account in the further system development.

c) The software for automatically detecting and extracting the information about peak frequencies and/or bandwidths from a series of spectrograms generated by the Gabor transform needs to be further developed, although the similar software used for the Fourier transform has been implemented.

Finally, it is important to point out that the experimental results shown in the previous chapter and the conclusions drawn in this chapter have demonstrated two major advantages of peak frequency imaging: higher lateral resoulation and quantification of dependent absorption. So peak frequency imaging may be used to aid medical diagnostic imaging. It may help distinguish some closely-located targets in the lateral direction and differentiate between soft tissues having differing frequency dependent absorption which is hard to be detected by using conventional B mode imaging.

PART I APPENDIX A

FOURIER TRANSFORM AND ITS DISCRETE AND FAST FORMS

The Fourier transform and its discrete and fast forms can be found in many textbooks. For convenience, they are briefly described in this appendix.

§ I.A.1 Fourier Transform

The Fourier transform is a principal mathematical tool in the many signal processing and analysis applications, especially in the analysis of linear time-invariant systems. The Fourier integral is conventionally defined by the expression shown in (I-A-1).

$$H(f) = \int_{-\infty}^{\infty} h(t)\, e^{-j2\pi ft} dt \tag{I-A-1}$$

If the integral exists for every value of the parameter t, then Equation (I-A-1) defines $H(f)$ as the Fourier transform of $h(t)$. Typically, $h(t)$ is termed a function of the variable time and $H(f)$ is termed a function of the variable frequency. In general, the Fourier transform is a complex quantity:

$$H(f) = R(f) + jI(f) = A(f)\, e^{j\theta(f)} \tag{I-A-2}$$

where, $R(f)$ and $I(f)$ are the real and imaginary parts of the Fourier transform. $A(f)$ and $\theta(f)$ are the amplitude and phase of the Fourier transform. The relations between $A(f)$, $\theta(f)$ and $R(f)$, $I(f)$ are shown in (I-A-3).

$$\begin{aligned} A(f) &= \sqrt{R^2(f) + I^2(f)} \\ \theta(f) &= \arctan\frac{R(f)}{I(f)} \end{aligned} \tag{I-A-3}$$

The inverse Fourier transform is defined in (I-A-4).

$$h(f) = \int_{-\infty}^{\infty} H(f)\, e^{j2\pi ft} df \tag{I-A-4}$$

§ I.A.2 Discrete Fourier Transform

Since many applications involving the continuous Fourier transform rely on digital computer for implementation, this leads to the use of the discrete Fourier transform (DFT) and hence the fast Fourier transform (FFT).

The discrete values in both the time and frequency domains are obtained through a sampling theory. Note that sampling in the time domain results in a periodic function of frequency, and sampling in the frequency domain results in a periodic function of time. After assuming the waveform $h(t)$ is approximated by N samples in one period and its Fourier transform is also approximated by N samples in one period, the discrete Fourier transform can be expressed by

$$H\left(\frac{n}{NT}\right) = \sum_{k=0}^{N-1} h(kT)\, e^{-j2\pi nk/N}, \quad n = 0,1,\ldots,N-1 \qquad \text{(I-A-5)}$$

The discrete inverse Fourier transform is defined by

$$h(kT) = \frac{1}{N} \sum_{n=0}^{N-1} H\left(\frac{n}{NT}\right) e^{j2\pi nk/N}, \quad k = 0,1,\ldots,N-1 \qquad \text{(I-A-6)}$$

where, T is the sampling interval.

Since the discrete waveform $h(kT)$ has N data points and the Fourier spectrum consists of N separate frequency elements, the number of complex multiplications is proportional to N^2. For large N, the computation of the discrete Fourier transform requires excessive machine time even with high-speed computers.

§ I.A.3 Fast Fourier Transform

The solution for reducing the computing time of the discrete Fourier transform was not found until 1965 when a mathematical algorithm, which has become known as the fast Fourier transform (FFT) was published (Cooley and Tukey, 1965). This algorithm assumes the samples N as a base-2 number, i.e., $N = 2^{\gamma}$. Then k, n can be represented in binary form. Using the special feature of the item $[e^{-j2\pi/N}]^N = 1$, the N^2 complex multiplications are replaced by γ summations and two complex

multiplications in each summation. However, the multiplier in the first multiplication of each summation is actually unity, so the final number of complex multiplications in the FFT algorithm is $N\gamma$ or $Nlog_2N$.

Many variations of the FFT algorithm have been developed since then. Each algorithm variation is formulated to exploit either a particular property of the data being transformed or the computer architecture. Although the fast Fourier transform is simply an algorithm that can compute the discrete Fourier transform much more rapidly than other available algorithms. it plays an important role in practical applications.

PART I REFERENCES

1. Almgren R., *Gabor Spectrogram - a Revolution in Joint Time-Frequency Analysis*, **A Distributed Document with the Gabor Transform,** 1993.
2. Bastiaans M. J., *Gabor's Expansion of a Signal into Gassian Elementary Signals,* **Proceedings of the IEEE** Vol. 68, pp. 594 - 598, April 1980.
3. Bastiaans M. J., *A Sampling Theorem for the Complex Spectrogram and Gabor's Expansion of a Signal in Gaussian Elementary Signals,* **Optical Engineering** Vol. 20, pp. 594 - 598, August 1981.
4. Classen T. .C M., and Mecklenbrauker W. F. G., *The Wigner Distribution --- A Tool for Time-Frequency Signal Analysis, Part III: Relations with other time-frequency signal transformations,* **Philips J, Res.,** Vol. 35, No. 6, pp. 372 - 389, 1980.
5. Cohen L., *Time-Frequency Distributions - A Review,* **Proceedings of the IEEE,** Vol. 77, No. 7, pp. 941 - 981, July 1989.
6. Cooley J. W., and Tukey J. W., *An Algorithm for the Machine Calculation of Complex Fourier Series*, **Mathematics of Computation** Vol. 19, No. 90, pp. 297 - 301, 1965.
7. Daubechies I., *The Wavelet Transform: A Method for Time-Frequency Localization,* **Advances in Spectrum Analysis and Array Processing,** Prentice Hall, pp. 366 - 417, Chapter 8, 1990.
8. Delprat N. et al, *Asymptotic Wavelet and Gabor Analysis: Extraction of Instantaneous Frequencies,* **IEEE Trans. on Information Theory,** Vol.38, No. 2, pp.644 - 664, March 1992.
9. Dines K. A., and Kak A. C., *Ultrasonic Attenuation Tomography of Soft Tissues,* **Ultrasonic Imaging,** Vol. 1, pp. 16 - 23, 1979.
10 Ferrari L. A., Ranalli R., and Gopinathen R., *A Comparison of Images Derived from the Envelope and Instantaneous Frequency of Pulse-Echo Signals Experimental Results,* **Ultrasonic Imaging,** Vol. 6, 1984.
11 Ferrari L. A., Sankar P. V., Fink M., Shin S. B., and Chandler P., *Use of*

Signal Phase in Medical Ultrasound, **Acta Electronics,** Vol. 26, pp. 111 - 120, 1984.

12 Flax S. W. et al, *Spectral Characterization and Attenuation Measurements in Ultrasound,* **Ultrasonic Imaging,** Vol. 5, 1983.

13. Gabor D., *Theory of Communication,* **Journal of the IEE**, Vol. 93, Part III, pp. 429 - 457, 1946.

14. Gehlbach S. M., Sommer F. G., and Stern R. A., *Scatter-Induced Frequency Variations in Reflected Acoustic Pulses: Implications for Tissue Characterization,* **Ultrasonic Imaging,** Vol. 7, pp. 172 - 178, 1985.

15. Harper C., *Frequency Domain Ultrasonic Imaging,* **A Thesis for Master Degree**, University of Wakaito, 1990.

16. Harris F. J., *On the Use of Windows for Harmonic Analysis With the Discrete Fourier Transform,* **Proceedings of the IEEE**, Vol. 66, No. 1, January 1978.

17. Jain A. K., **Fundamentals of Digital Image Processing,** Prentice Hall Inc., 1989.

18. Janssen A. J. E. M., *Gabor Representation of Generalized Functions,* **J. Math. Anal. Appl.** Vol. 83, pp. 377 - 394, 1981.

19. Kasai C. et al, *Real Time Two-Dimensional Blood Flow Imaging Using an Auto Correlation Technique,* **IEEE Trans. on Sonics Ultrason.** SU-32, pp. 458 - 464, 1985.

20. Kay S. M., and Sudhaker R. A., *Zero Crossing-Based Spectrum Analyzer,* **IEEE Trans. Acoust. Speech Signal Proc.** ASSP-34, pp. 96 - 104, 1986.

21. Komaili J., Sankar P. V., Ferrari L. A., and Leaman S., *The Instantaneous Frequency of a Sinewave Squelched Bandlimited Signal,* **Ultrasonic Imaging,** Vol. 8, pp. 285 - 295, 1986.

22. Kuttruff H., **Ultrasonics - Fundamentals and Applications**, Elsevier Science Publishers Ltd., 1991.

23. Lerski R. A., **Practical Ultrasound**, IRL Press Limited, 1988.

24. Lizzi F., Katz Louis L. St., and Coleman D. J., *Applications of Spectral Analysis in Medical Ultrasonography,* **ULTRASONICS**, pp. 77 - 80, March 1976.

25. Lizzi F., Greennbaum M., Feleppa E. J., and Elbaum M., *Theoretical*

Framework for Spectrum Analysis in Ultrasonic Tissue Characterization, **J. Acoust. Soc. Am.** Vol. 74, No. 4, pp. 1366 - 1373, April 1983.

26. Momaili J. Sankar P. V., Ferrari L. A., and Leeman S., *The Instantaneous Frequency of a Sinewave Squelched Bandlimited Signal,* **Ultrasound Imaging,** Vol. 8, pp. 285 - 295, 1986.
27. Oosterveld B. J., Romijn R. L., and Thijssen J. M., *Phase-Derivative Imaging II: Effects of Beam Diffraction and of Scatterer Density,* **Ultrasonic Imaging,** Vol. 11, pp. 153 - 174, 1989.
28. Page C. H., *Instantaneous Power Spectra,* **Journal of Appl. Physics,** Vol. 23, pp. 103 - 106, 1952.
29. Qian S., Chen K., and Li S., *Optical Biorthogonal Functions for Finite Discrete-Time Gabor Expansion,* **Signal Processing,** Vol. 27, No. 2, pp. 177 - 184, May 1992.
30. Qian S., and Chen D., *Discrete Gabor Transform,* **IEEE Trans. on Signal Processing,** pp. 2429 - 2438, July 1993.
31. Rihaczek A. W., *Signal Energy Distribution in Time and Frequency,* **IEEE Trans. on Information Theory,** Vol. IT-14, pp. 369 - 374, 1968.
32. Romijn R. L., Oosterveld B. J., and Thijssen J. M., *Calculation and Stabilization Methods of Instantaneous Frequency Echogram,* **Ultrasound Imaging,** Vol. 8, pp. 42 - 43, 1986.
33. Romijn R. L., Oosterveld B. J., and Thijssen J. M., *Phase-Derivative Imaging I: Methods and Stabilization Analysis,* **Ultrasonic Imaging,** Vol. 9, pp. 147 - 161, 1987.
34. Round W. H., and Bates R. H. T., *Modification of Spectra of Pulse from Ultrasonic Transducers by Scatterers in Non-Attenuating and In Attenuating Media,* **Ultrasonic Image,** Vol. 9, 1987.
35. Seggie D. A. et al, *Ultrasonic Imaging Using The Instantaneous Frequency of Pulse-Echo Signals,* **Acoustical Imaging**, Vol. 14, pp. 487 - 496, Plenum Press, New York, 1985.
36. Shung K. K., and Thieme G. A., **Ultrasonic Scattering in Biological Tissues,** CRC Press, 1993.
37. Surridge A. D., *Frequency Shift of an Acoustic Wavetrain Due to Atmosphere*

Absorption, **Acustica**, Vol. 44, 1980.

38. Thijssen J. M., Oosterveld B. J., and Romijn R. L., *Phase-Derivative Imaging III: Theoretical Derivation of First and Second Order Statistics,* **Ultrasonic Imaging,** Vol. 12, pp. 17 - 34, 1990.
39. Wells P. N. T., **Biomedical Ultrasonics**, Academic Press, London, 1977.
40. Wells P.N.T., **Ultrasound in Medical Diagnostics**, Walter de Gruyter, Bertlin, 1988.
41. Wells P.N.T., *The Present Status of Ultrasonic Imaging in Medicine*, **Ultrasonics,** Vol. 31, No. 5, pp. 345 - 352, 1993.
42. Wexler J., and Raz S., *Discrete Gabor Expansions,* **Signal Processing,** Vol. 21, pp. 207 - 220, 1990.
43. Wigner E., *On the Quantum Correction for Thermodynamic Equilibrium,* **Phys. Rev.,** Vol. 40, pp. 749 - 759, 1932.
44. Whittaker R., **Television Production,** Mayfield Publishing Company, 1993.

PART II CHAPTER 1

FOURIER TRANSFORM PROFILOMETRY

§ II.1.1 Introduction

The demand for the nondestructive measurement of three-dimensional (3-D) object surfaces is increasing in many industrial applications. There are a lot of techniques using optical measurement systems available for this purpose because of their inherent accuracy and nondestructive nature. Most of them can be grouped into three main classes: geometric, interferometric and Fourier transform profilometric.

The geometric methods are based on the well-established principle of triangulation. The desired information of 3-D object surface is first obtained from two (or more) two-dimensional (2-D) views. This is very similar to the stereoscopic vision. The points of interest on the object are then projected on several 2-D image planes. Using the principles of triangulation, the 3-D positions of those points in the real world can easily be determined (Idesawa, 1989).

In comparison, the interferometric methods use the principle of interference to determine the 3-D object surface. First, a grating is put between the source of light and the surface of an object to be measured. When this grating image is observed through the second grating of same type, interference fringes known as *moiré* fringes appear. The moiré fringes represent the contour lines on the 3-D object surface. A contour map of the object can then be obtained using fringe-contour-generation techniques (Chen, 1988; Patorski, 1988; Suzuki et al., 1988).

Since the geometric methods require two (or more) views and the interferometric methods need two gratings to generate the moiré fringes, both techniques have complicated optical systems. Although interferometric methods using moiré contouring techniques are widely used in laboratory, there are still many problems associated with the moiré contouring technique, which make its application to the

industrial applications very difficult. The major problems include automatic distinction between a depression and an elevation on the object surface, assigning fringe order for surface height measurement, determining the centre line of some broad fringes, and interpolating the region between contour lines (Takeda et al., 1983).

To be useful to the industrial end-user, general optical fringe pattern interpretation needs to be automated.

Fourier transform profilometry applies the Fourier transform to the non-contour types of fringe patterns to extract information about the 3-D object surface. The grating image projected on the 3-D object surface is deformed due to the varied height of the object. The deformed grating image is then Fourier transformed and processed in the frequency domain as well as in the spatial domain to extract the slowly varying phase function that is related to the height variation of the 3-D object surface. As a result, all the data processing can be automated in the computer. In addition, the optical system is relatively simple because only one grating is used and no moiré fringes occur.

Fourier transform profilometry was first proposed by Takeda in 1983 and investigated since by many other researchers (Kreis, 1986; Green et al., 1986a and 1986b; Burton et al., 1988 and 1989; Towers et al., 1989 and 1991; Vrooman, 1989). From my experiments, however, I have found that the traditional methods proposed by Takeda in Fourier transform profilometry sometimes don't provide highly accurate measurements of some 3-D object surfaces, and the other phase unwrapping algorithms developed later by other researchers to improve the accuracy of 3-D object surface measurement are very complicated. Therefore, I have investigated a number of new image processing-based methods used with Fourier transform profilometry to improve the accuracy of 3-D object surface measurements.

The major contributions in this part of my thesis are as follows:

- Studies of the principle of Fourier transform profilometry and the traditional

Takeda's methods used in Fourier transform profilometry.

- Analysis of the major error sources that may occur in the discrete Fourier transform (or fast Fourier transform) and the phase unwrapping algorithm used in Fourier transform profilometry.
- Investigating the new image processing-based methods to improve the accuracy in measurement of 3-D object's surfaces. Those include application of a weighted window function to the isolated first sidelobe in the frequency domain, automatic determination of the bandwidth of a bandpass filter based on the actual spectrum, and use of object boundary guided phase unwrapping to solve large-scale discontinuities around the object boundary on the modulo 2π phase map.

The outline of the remainder in this part of the thesis is as follows. In the rest of this chapter, the simple principle of Fourier transform profilometry is briefly described. More detailed description of Fourier transform profilometry and the traditional Takeda's methods are provided in Appendix A or can be reviewed in the original papers written by Takeda *et al.* in 1982 and 1983. Chapter two gives an analysis of the major error sources that may cause the inaccurate measurement of 3-D object surface and investigates some new methods in image processing techniques to improve the accuracy in measurement of 3-D object surface. The results obtained using the new methods are provided in chapter three and are compared with those obtained using the traditional Takeda's methods. In the last chapter conclusions are drawn and the suggestions of possible further developments in Fourier transform profilometry are given.

§ II.1.2 Principle of Fourier Transform Profilometry

Fourier transform profilometry is in fact a kind of fringe pattern analysis method. It extracts the desired phase information using a Fourier transform of the fringe pattern arising out of the interference of tilted wavefronts. The two kinds of optical systems used to generate fringe patterns in Fourier transform profilometry are shown in Figure II.A.1 and Figure II.A.2 respectively.

The phase modulated fringe pattern $g(x,y)$ has the general form (Takeda et al., 1982)

$$g(x,y) = a(x,y) + b(x,y)\cos[2\pi f_c x + \phi(x,y)] \qquad \text{(II-1-1)}$$

where, the phase function $\phi(x,y)$ contains the desired important information about the 3-D object profile. The unwanted irradiance variations arising from the nonuniform light reflection or transmission are expressed by terms $a(x,y)$ and $b(x,y)$. The fundamental frequency of the regular grating pattern is given by f_c.

The above form of the fringe pattern can be rewritten

$$g(x,y) = a(x,y) + c(x,y)\,e^{2\pi j f_c x} + c^*(x,y)\,e^{-2\pi j f_c x} \qquad \text{(II-1-2)}$$

where

$$c(x,y) = \frac{1}{2} b(x,y)\,e^{j\phi(x,y)} \qquad \text{(II-1-3)}$$

and * denotes a complex conjugate.

Taking the Fourier transform of the fringe pattern with respect to x will give

$$G(f,y) = A(f,y) + C(f-f_c,y) + C^*(f+f_c,y) \qquad \text{(II-1-4)}$$

where, the capital letters denote the Fourier spectrum and f is the variable in the frequency domain. Since the spatial variations of $a(x,y)$, $b(x,y)$ and $\phi(x,y)$ are slow compared to the variation introduced by the fundamental frequency f_c, the Fourier spectra in (II-1-4) are separated by the fundamental frequency f_c into three distinct regions, corresponding to the three items in (II-1-2). The three distinct regions in Fourier spectra can be seen from the spectrum of sampled grating image shown in Figure II.A.3,

The central zero order spike represents the average brightness of the image and slowly varying image intensity. The two symmetrical first order sidelobes contain the desired phase information shown in (II-1-3). Removing the zero order spike and one of the first order sidelobes yields a non-symmetrical spectrum that on inverse Fourier transformation will produce the complex function $c(x,y)exp(2\pi j f_c x)$ (Takeda et al.,

1983). In the same way as the phase modulated fringe pattern, using a regular grating pattern will produce the complex function $exp(-2\pi jf_c x)$. Multiplying $c(x,y)exp(2\pi jf_c x)$ by $exp(-2\pi jf_c x)$ then gives $c(x,y)$.

The desired phase function $\phi(x,y)$ is obtained by using the following equation

$$\phi(x,y) = \tan^{-1}\left[\frac{Im[c(x,y)]}{Re[c(x,y)]}\right] . \qquad \text{(II-1-5)}$$

Since the computer-generated arctangent routine gives a principal value ranging from $-\pi$ to π, the calculated phase function $\phi(x,y)$ is wrapped into this range or looks like a 'sawtooth' as shown in Figure II.A.4. The discontinuities in the principal phase are then detected using a threshold between π and 2π, and the continuous phase function can be constructed by adding the phase offsets based on the direction (positive or negative) of phase jumps. Consequently, the height distribution of 3-D object profile is reconstructed using the calibrated system geometric parameters.

PART II CHAPTER 2

IMAGING PROCESSING TECHNIQUES

§ II.2.1 Introduction

In Fourier transform profilometry, the grating image projected on a 3-D object surface is usually captured and digitized into a discrete form for being processed on a digital computer. The height distribution of the object surface is then reconstructed by using a series of image processing techniques. Those techniques are mainly described in Appendix A. They include one-dimensional (1-D) discrete Fourier transforming both the deformed grating image and the regular grating image in the x direction line by line, isolation of the first sidelobes in both spectra, discrete inverse Fourier transforming the isolated sidelobes, extraction of phase variation information through the multiplication of both complex signals from inverse Fourier transform, phase unwrapping of the discontinuous phase distribution, and finally phase-to-height conversion.

However, some 3-D object surfaces reconstructed using those traditional methods didn't appear to give accurate representations of the actual 3-D object profiles, while the others had very large errors. One of the examples was a solid hemisphere with smooth surface lying on a smooth reference plane. The reconstructed surfaces of this test object and the reference plane are shown in Figure II.2.1. It shows a very poor representation of both the hemisphere and the reference plane.

This chapter gives a detailed analysis of the major causes of error in the traditional Takeda's methods and then investigates some new methods to improve the accuracy of 3-D object surface measurement using the Fourier transform profilometry.

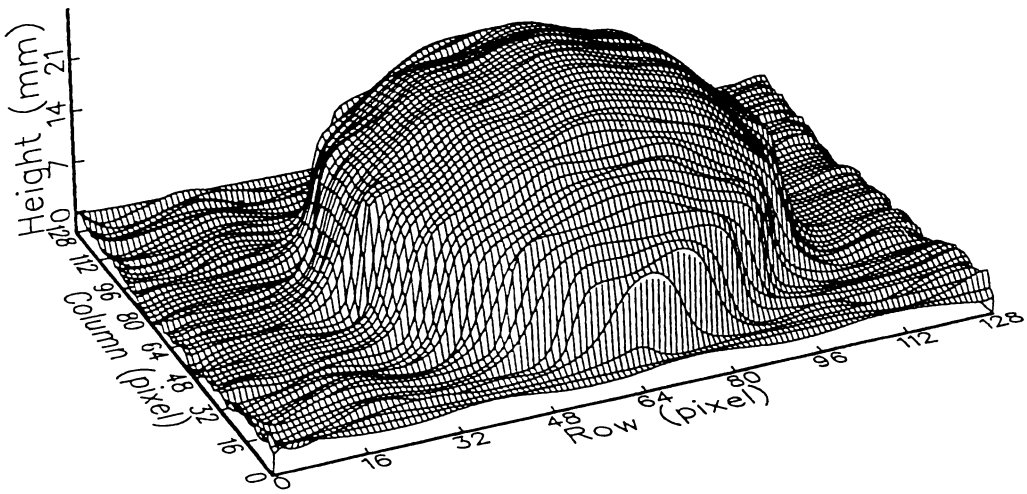


Figure II.2.1: A hemisphere reconstructed using the traditional methods in FTP

§ II.2.2 Analysis of Major Causes of Error

As the name suggests, the Fourier transform plays an important role in Fourier transform profilometry. To perform the Fourier transform on a fringe image using a digital computer, the fringe image must be sampled to allow the discrete Fourier transform (DFT) or the fast Fourier transform (FFT) to be used. The Fourier transform and its discrete and fast forms are discussed elsewhere in the first part of my thesis (see Appendix A in Part I). It is noticed that the DFT and the inverse DFT are based on the sampling theorem, which says that sampling in the time domain results in a periodic function of frequency and sampling in the frequency domain results in a periodic function of time.

If the signal is undersampled, i.e., the sampling rate is too slow, the error called *aliasing* will occur in the signal periodic spectrum. Sampling data to be processed also results in the sampled data being limited to a period of time. This means that the data to be Fourier transformed seem to be truncated on both ends of a series of sampled data, but improper truncation of data would cause *leakage* error.

In addition, the desired first sidelobe in the spectrum is usually isolated by using a bandpass filter. Since the 1-D spectra vary from line to line in the fringe pattern,

the phase variation recovered will heavily depend on the bandwidth of this bandpass filter. The traditional phase unwrapping algorithm is also unable to correct the large-scale discontinuity in the modulo 2π phase map constructed by a computer-generated arctangent routine. All these problems have made some object surfaces difficult to reconstruct or have very large errors even if they can be reconstructed.

§ II.2.2.1 Aliasing

As a continuous signal is sampled into its discrete form, the spectrum of the signal appears periodically at the multiples of the sampling frequency nf_s. If the sampling frequency f_s is less than twice the highest frequency component in the signal, the higher frequency components in one spectrum are then overlapped with the lower frequency components in the other spectrum. This is commonly called 'aliasing' and can be seen from an example shown in Figure II.2.2. In theory, the minimum sampling frequency used to avoid the aliasing is equal to twice the highest frequency in the signal, which is usually called the Nyquist frequency, but the minimum sampling rate needed in practice is often higher than the Nyquist frequency, usually five to six times high than the highest frequency in the signal.

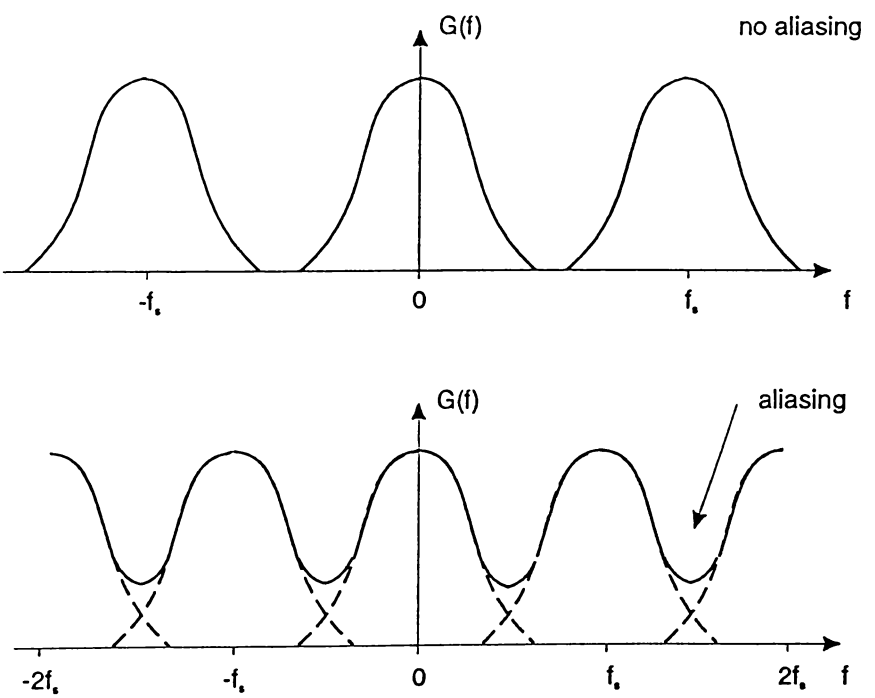


Figure II.2.2: Aliasing in the DFT

The sampling frequency f_s in Fourier transform profilometry is determined by the ratio of the number of samples to the width of the digitized grating image. It is not to be confused with the spatial carrier frequency or the fundamental frequency of the observed grating image f_c, that is defined by the ratio of the number of fringes to the width of fringe pattern. In Fourier transform profilometry it is assumed that the phase variation $\Delta\phi(x,y)$ and the uneven distribution of light reflectivity on the object surface $r(x,y)$ vary slowly compared with the spatial carrier frequency f_c in most practical applications, so the spatial carrier frequency is probably the highest frequency component in the signal except for any noise. In my experiments, the sampling frequency was set about four times higher than the spatial carrier frequency. As a result, the aliasing seemed not to be the major problem in Fourier transform profilometry, but it is worthwhile to mention it here because it often causes errors in discrete signal spectral analysis.

§ II.2.2.2 Leakage in Both Frequency and Spatial Domains

The data samples to be analysed using the discrete Fourier transform are normally limited to a certain number N and also must be assumed to be periodic over the interval N/f_s or NT. But the sampled data to be processed often have discontinuities at the data boundaries of the periodic extension. It seems that the data are truncated by a rectangular window. Consequently, the frequency components of the data appear to leak out into portions of the spectrum adjacent to the correct spectral value due to the sharp corners of the rectangular window. The phenomenon of frequency leakage is illustrated in Figure II.2.3 by using a simple sinusoidal signal. It is noticed that not only are some extra frequency components added in the discrete spectrum but also the frequency f'_m where the largest spectral value appears is not same as the correct value f_m in the continuous spectrum.

In Fourier transform profilometry, the sampled data taken from each line in the fringe image are obviously not periodic because of the discontinuities at the data boundaries of the periodic extension.

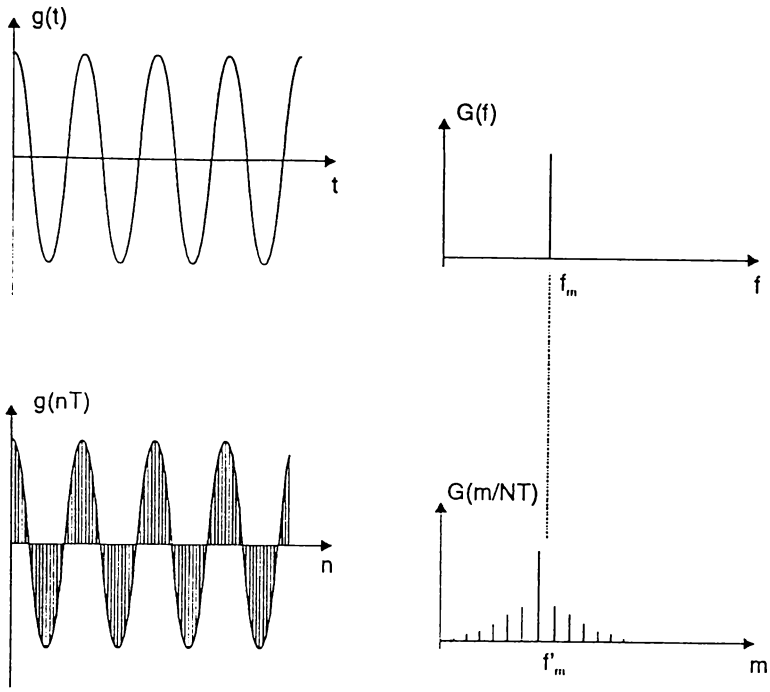


Figure II.2.3: Frequency leakage in the DFT

In addition, one of the first sidelobes in the periodic spectrum must be isolated for the discrete inverse Fourier transform in Fourier transform profilometry. In the ideal condition, the sidelobe appears to be periodic in the spectrum with decreasing magnitudes. Usually, the desired first sidelobe in the spectrum is isolated by using a bandpass filter with the rectangular window type. Owing to sharp corner of the rectangular window, the isolated sidelobe becomes non-periodic with respect to the other sidelobes , but the discrete inverse Fourier transform assumes the data must be periodic. Consequently, the leakage would occur in the obtained complex signal in the spatial domain similar to the way it does in the frequency domain .

According to the principle of Fourier transform profilometry, the recovery of the phase variation $\Delta\phi(x,y)$ is heavily dependent on the complete cancellation of the fundamental frequency of regular grating pattern through the DFT and inverse DFT. If the leakage occurs in either frequency or spatial domain, then the fundamental frequency of the regular grating pattern would not be completely cancelled so that the recovered phase variation $\Delta\phi(x,y)$ would be contaminated by the leaked-out

components of spatial carrier frequency. As a result, the height distribution of the 3-D object surface would have some errors.

§ II.2.2.3 Isolation of the First Sidelobe

It is assumed in Fourier transform profilometry that the phase variation $\Delta\phi(x,y)$ and the uneven distribution of light reflectivity on the object surface $r(x,y)$ vary slowly compared with the spatial carrier frequency f_c. Since the grating image $g(x,y)$ is a phase-modulated signal, most of frequency components in $\Delta\phi(x,y)$ and $r(x,y)$ are located on both sides of the spatial carrier frequencies nf_c as shown in Figure II.A.3. Normally, those components can be extracted using a bandpass filter centred at the spatial carrier frequencies.

Although the phase variation $\Delta\phi(x,y)$ is assumed to vary slowly, the frequency components in $\Delta\phi(x,y)$ are different for each line. In particular, $\Delta\phi(x,y)$ may contain higher frequency components in some surface areas of the 3-D object if the surface is not smooth or the height of the object surface changes rapidly. If the bandpass filter used to isolate the desired first sidelobe is not flexible on the bandwidth for every line, the higher frequency components of the phase variation $\Delta\phi(x,y)$ in some surface areas would be missed out. Consequently, the true phase variation $\Delta\phi(x,y)$ in those areas may not be completely reconstructed after the inverse Fourier transform.

In addition, using a bandpass filter with a narrower bandwidth may not completely extract the frequency components of $r(x,y)$, if the uneven distribution of light reflectivity $r(x,y)$ contains higher frequency components. Consequently the reconstructed $r(x,y)$ after the inverse Fourier transform would not be the true representation of the actual one. The reconstructed $r(x,y)$ may become a complex function and the imaginary part of $r(x,y)$ would be misinterpreted as the phase variation such that the reconstructed phase variation $\Delta\phi(x,y)$ would have some errors.

Furthermore, using a bandpass filter with the incorrect bandwidth would allow some of the high frequency components of noise to be unnecessarily included in the isolated spectrum. Some lines of samples in a fringe image contain very slow

variation of phase and reflection or no phase variation at all, particularly on the reference plane. If the bandpass filter used still uses the same bandwidth as used for other lines where there are higher phase variations, some not very high frequency noise would be unnecessarily included in the spectrum isolated. Consequently those not very high frequency components of noise after the inverse Fourier transform would cause unexpected error in the recovered phase variation $\Delta\phi(x,y)$.

§ II.2.2.4 Phase Unwrapping

In Fourier transform profilometry, the phase variation $\Delta\phi(x,y)$ obtained using the arctangent function in (II-1-5) will have a principal value ranging from $-\pi$ to π or 0 to 2π, because this function is normally implemented by a computer-generated routine. This routine unlike its corresponding theoretical function not only calculates the product but also checks the signs of the numerator and denominator in its argument. Consequently the phase distribution produced using this computer-generated routine is discontinuous or wrapped. To reconstruct the height distribution of the 3-D object surface, the discontinuous phase distribution must be unwrapped. The algorithm used in the traditional methods for phase unwrapping that are described in Appendix A is relatively simple and efficient in most cases, but it has disadvantages.

According to this algorithm the phase unwrapping always starts from left to right on each line in the x direction and only one line in the y direction. The phase on other lines in the y direction are corrected on the basis of the offset obtained from this line only. If there is a large-scale discontinuity, this algorithm fails. This is because the maximum offset phase that can be added in each step of phase unwrapping is $\pm 2\pi$ while the actual phase offset needed at the large-scale discontinuity may be $\pm 4\pi$ or more. The large-scale discontinuity usually occurs at the boundary of the object. Using the traditional phase unwrapping method that starts from left to right in the x direction often causes this error.

In general, the whole surface of an object to be measured should be visible in the fringe image and as well as the reference plane, but in some fringe images, there is

no visible reference plane between the image edge and the object boundary, or the surface of an object starts to be visible immediately from the image edge. If this happens on the starting point of phase unwrapping and also the actual phase variation at this point is beyond the range of $-\pi$ to π, the algorithm in the traditional methods for phase unwrapping becomes unable to detect it. Thus the following phase unwrapping would be based on this starting erroneous phase that is difficult to correct.

Although there is no Fourier transform in the y direction to cause the phase discontinuity, the phase distribution in the y direction is discontinuous after the phase unwrapping in the x direction. In the traditional methods the phase offset obtained from phase unwrapping on only one line in the y direction is used for all lines in the y direction. The actual situation is more complicated especially at the object boundary. If there is also a large-scale discontinuity at the object boundary in the y direction, the phase offset would be different around this area compared with the others.

§ II.2.3 New Image Processing-Based Methods

To avoid or reduce the possible errors caused by the above factors, I have investigated some new image processing-based methods to improve the accuracy of 3-D object surface measurement in Fourier transform profilometry. Those new methods include the application of the weighted window functions on the data samples and the isolated first sidelobe to reduce the leakage in both spatial and frequency domains, the automatic determination of the bandwidth of the bandpass filter based on the actual spectral width in order to include the desired phase and background information and exclude the unwanted noise, and the detection of the object boundary to guide the phase unwrapping to solve the large-scale discontinuity around the object boundary.

§ II.2.3.1 Weighted Window Functions

To reduce the frequency leakage, it is common to select an appropriate weighted window function to round off the sharp corners of the data samples that are truncated

by a rectangular window. From a popular viewpoint, the weighted window function is applied to the data samples (as a multiplicative weighting) to reduce the order of the discontinuity at the data boundaries of the periodic extension. Consequently the windowed data samples are smoothly brought to zero or near zero at the data boundaries so that the periodic extension of the data is continuous in many orders of derivative. A number of different forms of the weighted window functions were early proposed (Jenkins, 1961; Blackman 1967; Welch, 1967; Tukey, 1967). The popular window functions such as Hanning and Hamming windows have been used in the ultrasound frequency-domain imaging and discussed in the first part of my thesis. A comprehensive catalogue of weighted window functions and the comparison of their performances can be reviewed in the paper by Harris (1978).

The weighted window function was first used in Fourier transform profilometry on the data samples in 1989 (Burton et al., 1989) and also reported later in 1990 (Malcolm et al., 1990). However, no research was reported on using the weighted window function on the isolated first sidelobe in the frequency domain until 1992 (Judge et al., 1992) when I investigated this method. Just as is applied to the data samples in the spatial domain, an appropriate weighted window function is applied to the isolated first sidelobe in the frequency domain to reduce the order of the discontinuity at the sidelobe boundaries of the periodic extension. The results obtained in experiments, to be shown in the next chapter, have proved that the use of weighted window function on the isolated first sidelobe in the frequency domain has a significant effect on the accuracy of 3-D object surface measurement.

In theory, the results of the inverse FFT of the spectrum of a set of data samples should have the same values as the original samples , but due to the leakage, there are always some errors. To choose which pair of weighted window functions are to be used in Fourier transform profilometry, I have tested some combinations of the weighted window functions on a single line of data samples in a test hemisphere fringe image. The results of tests have shown that a pair of Hanning windows have the smallest average error and a pair of BHar3 and Hanning windows have the smallest maximum error. The detailed test results are presented in Appendix B. For

the purpose of simplicity and popularity, I have used a pair of Hanning windows in all my experiments.

§ II.2.3.2 Determination of the Bandwidth of Bandpass Filter

In practice, it is also important to determine the bandwidth of the bandpass filter for extracting the desired information from the first sidelobe. As described in II.1.2, the grating image $g(x,y)$ is a phase-modulated signal, the desired frequency components in $\Delta\phi(x,y)$ and the unwanted distribution of light reflectivity $r(x,y)$ are mostly located on both sides of the spatial carrier frequency f_c in either of the first sidelobes. They vary slowly as compared with the spatial carrier frequency f_c, but the frequency components in $\Delta\phi(x,y)$ and $r(x,y)$ are not the same in all lines. For some lines of sampled data that represent the regular fringe on the reference plane, there is almost no frequency information of $\Delta\phi(x,y)$ at all. For most lines of data that contain the deformed fringe pattern, the highest frequency components of $\Delta\phi(x,y)$ and $r(x,y)$ vary, some close to the spatial carrier frequency f_c and some far away. To allow the isolated sidelobe to have the desired frequency information of $\Delta\phi(x,y)$ and $r(x,y)$ but few noise frequency components, it is necessary to automatically determine the bandwidth of the bandpass filter based on the actual spectrum on each line.

The cutoff frequency f_{cut} of bandpass is normally defined at the position in a power spectrum where the magnitude is reduced to -3 dB from 0 dB of the maximum value. The maximum value in the power spectrum is usually at the carrier frequency f_c for the phase-modulated signal $g(x,y)$. If the spectral values on both sides of the carrier frequency are roughly the same, the bandwidth of the bandpass filter can be based on the cutoff frequency on one side of the carrier frequency f_c. Consequently, the bandwidth of the bandpass filter BW is equal to

$$BW = |2\,(f_{cut} - f_c)| \ . \qquad \text{(II-2-1)}$$

If it is not, the bandwidth of the bandpass filter must be determined according to the actual cutoff frequencies f_{cut1} and f_{cut2} calculated on both sides of the carrier frequency f_c. As a result, the bandwidth of the bandpass filter BW is calculated from

$$BW = |f_{cut1} - f_{cut2}| \ . \qquad \text{(II-2-2)}$$

Since the spatial carrier frequency f_c is defined by the ratio of the number of fringes to the width of fringe pattern, which is usually constant over the entire fringe pattern, the bandwidth of the bandpass filter was measured by the spatial carrier frequency f_c. For example, the bandwidth of the bandpass filter may be much less than f_c for some lines of data and greater than f_c for other lines of data. If the bandwidth of the bandpass filter is automatically determined based on the actual spectrum, it would extract the important frequency information of $\Delta\phi(x,y)$ and $r(x,y)$ more successfully and reject most of unwanted frequency components of noise.

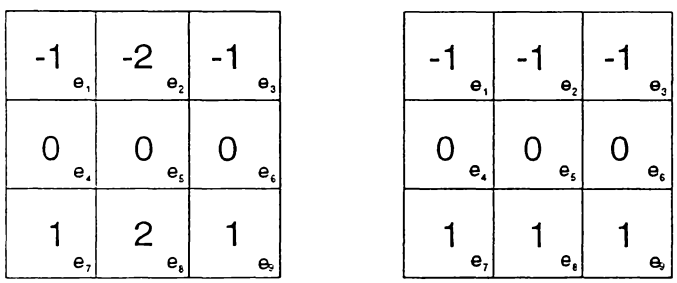
However the bandwidth of the bandpass filter must not be too narrow because the isolated sidelobe is to be multiplied by a weighted window function for reducing the leakage in the spatial domain. If the bandwidth of the bandpass filter is set too narrow, the shape of the weighted window function would be deformed such that the effect of reducing leakage would not be achieved.

In summary, the automatic determination of the bandwidth of the bandpass filter would result in a different bandwidth used to isolate the first sidelobe for each line of sampled data. The experimental results, which are to be shown in the next chapter, will confirm that using the different bandwidths of the bandpass filter for different lines of data has a noticeable effect on the reconstructed phase information.

§ II.2.3.3 Detection of Object Boundary

The 3-D object to be measured is usually put on the reference plane, part of which must also be visible in the fringe image so as to provide a reference from which the object height is measured. Since the surface of the 3-D object has been assumed to vary slowly, large-scale discontinuities normally occur around the object boundary. If the phase unwrapping is guided by the object boundary, it would save a lot of time in phase unwrapping because the phase variation on the reference plane is normally not wrapped. Also, it can avoid any possible errors arising from the incorrect phase unwrapping around the object boundary due to the large-scale discontinuities.

To use the object boundary guided phase unwrapping, the object boundary in the fringe pattern must be first detected. The object boundary can be detected using one of the common edge operators, the Sobel or the smoothed edge operator, but in the fringe pattern, the fringes have strong edges that will affect the detection of the object boundary. It has been noticed that the lines of grating are normal to the x axis in the fringe image so that most of the fringe edges are basically perpendicular to the x axis. To detect the object edges and ignore those fringe edges, only the edge operator in the y axis would be used. The Sobel and the smoothed edge operators in the y axis are shown in Figure II.2.4.



(a) Sobel (b) Smoothed

Figure II.2.4: The edge operators in the y axis

The 3 × 3 kernel of the edge operator is moved pixel by pixel around the image and every element in the kernel is multiplied with the corresponding pixel in the image which is covered by the kernel. The new value of centre pixel in the image that is covered by the kernel is calculated by the following formula

$$c_5 = c_1 \cdot e_1 + c_2 \cdot e_2 + c_3 \cdot e_3 + c_7 \cdot e_7 + c_8 \cdot e_8 + c_9 \cdot e_9 \qquad \text{(II-2-3)}$$

where, c_i and e_i are the corresponding pixel values in the image and in the kernel respectively.

Since the edge operation is performed in the y direction only, the edges detected are discontinuous in the y direction over the fringe pattern. Also, in the x direction there are not many strong edges detected. To determine the boundary of an object, the

* The processing steps used from Figure II.2.5 to Figure II.2.7 were as follows. After applying the edge detection to the fringe image of a hemisphere shown in Figure II.2.5, the edge map shown in Figure II.2.6 was obtained. Based on the histogram of any edge map, typically 5-10% of pixels in the edge map were declared as major edges. So the major edge points around the hemisphere boundary were selected by using a thresholding method. Afterwards, the B-spline routine (extracted from *Numerical Recipes* published by the Cambridge University Press) was applied twice to the two half circles to interpolate the missing edge points and the complete boundary of a hemisphere shown in Figure II.2.7 was finally obtained.

missing edge points on the object boundary must be estimated. The B-spline algorithm that is commonly used to smooth the curve is employed to determine the missing edge points on the object boundary.

As an example, the original fringe image of a test hemisphere is shown in Figure II.2.5. Its edge map generated by the Sobel edge operator is shown in Figure II.2.6. The final object boundary determined using the B-spline algorithm is shown in Figure II.2.7.*

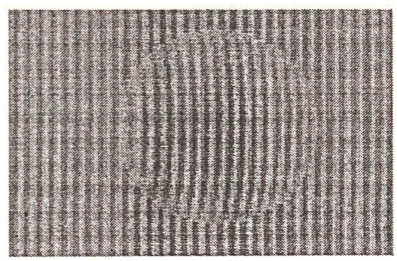


Figure II.2.5: The fringe image of a test hemisphere

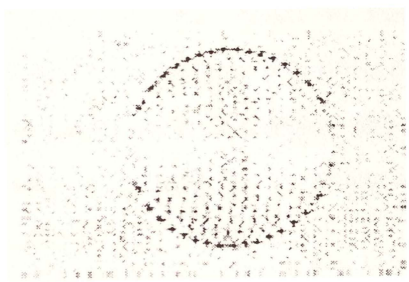


Figure II.2.6: The detected edges of a test hemisphere

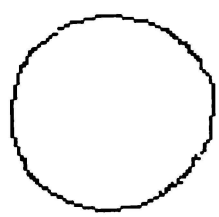


Figure II.2.7: The detected boundary of a test hemisphere

§ II.2.3.4 Objected Boundary Guided Phase Unwrapping

The scanning algorithm for phase unwrapping in the traditional methods has been proven to be efficient in computation and successful in most cases (Vrooman, 1989), but for the reasons mentioned earlier it cannot correctly unwrap large-scale discontinuities in the 2π modulo phase map especially at the object boundary area. A number of methods for phase unwrapping have been reported since Fourier transform profilometry emerged.

The cellular automata method (Spik et al., 1991) is one of the path independent algorithms that deal with the large-scale discontinuity of phase, but it needs hundreds of iterations on the whole image. One new phase-unwrapping algorithm (Huntley, 1989) that places cut lines in the phase map to prevent unwrapping through erroneous region has proven to be noise-immune. The tiling method (Tower et al., 1989) that utilizes graph theory to generate a minimum spanning tree for the efficient path of phase unwrapping is able to reject bad data to avoid possible errors.

However, these methods are relatively expensive in computation and complicated in implementation such that they are not suited to industrial applications. On the contrary, because the boundary of the object has been detected and the surface of the object has been assumed to vary slowly, the phase unwrapping can be performed on the object surface only using the traditional scanning method.

It is reasonable to choose the starting point at the centre of the object for phase unwrapping. The phase data are first unwrapped row by row until the boundary of the object and then the unwrapped phase data are unwrapped column by column until the boundary of the object again. Finally the unwrapped phase data within the object boundary are adjusted by a phase offset $\Delta\theta$ based on the difference between the average phase θ_{avg} on the reference plane and the maximum phase θ_{max} on the surface of object.

If $0 < |\theta_{max} - \theta_{avg}| < 2\pi$ then $\Delta\theta = 0$. If $2\pi \leq |\theta_{max} - \theta_{avg}| < 4\pi$ then $\Delta\theta = -2\pi$ and so on.

The new object boundary guided phase unwrapping algorithm not only reduces the computational time on the phase unwrapping, but also solves the problem of large-scale discontinuities around the object boundary. The successful results using object boundary guided phase unwrapping algorithm are shown in the next chapter.

PART II CHAPTER 3

EXPERIMENTAL RESULTS

§ II.3.1 Introduction

To show how well the new image processing-based methods proposed in the last chapter can improve accuracy of 3-D object surface measurement in Fourier transform profilometry, the profiles of some 3-D objects were reconstructed using both new methods and the traditional Takeda's methods. The optical system used in the experiments was the same as the parallel-optical system described in Appendix A. The fringe image was captured by a Panasonic[1] WV-CD50 CCD camera and digitized by an Imaging Technology[2] PCVISIONplus frame grabber that was plugged in one of the local bus slots of the standard PC. All images had the same size of 128 × 128 pixels with 8-bit precision. Both the regular grating image of reference plane and the fringe pattern containing the object surface were captured for every object to be measured. All new image processing-based methods were implemented in software and executed in an IBM compatible 486 PC clone. The arrangement of image capture and processing is shown in Figure II.3.1.

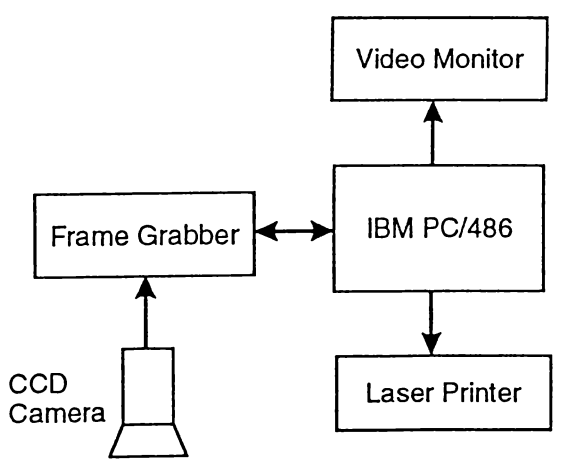


Figure II.3.1: Arrangement of image capture and processing

---

1 --- Panasonic - Matsushita Electric Trading Co., Ltd. P.O. Box 288, Central Osaka, Japan.

2 --- Imaging Technology - 600 West Cummings Park, Woburn, Massachusetts 01801, USA.

This chapter presents the profiles of some 3-D objects reconstructed by using the new image processing-based methods and compares them with the corresponding results obtained using the traditional Takeda's methods. The intermediate results are also presented to show how the new methods improve the accuracy of the measurement in every step.

§ II.3.2 Measured Phase Variation in Single Line

Since the phase variation in every line on the x direction is obtained mainly through 1-D Fourier transform of the sampled data and 1-D inverse Fourier transform of the isolated first sidelobe, the major leakage errors caused by the DFT (or FFT) and inverse DFT (or FFT) can be reduced by using the weighted window functions as described in the last chapter. To get the accurate phase variation information, either of the first sidelobes can be isolated using a bandpass filter with the automatically-determined bandwidth. The following two sections show the improvement of the reconstructed phase variation in a single line of sampled data by using the weighted window functions and the correct bandpass filter respectively.

§ II.3.2.1 Weighted Window Functions

In order to reduce the leakage occurring in the spatial domain, the isolated sidelobe was multiplied with a weighted window function before being inverse Fourier transformed in the new image processing-based methods. One single line of sampled data from the middle row of the fringe pattern of a hemisphere was tested by multiplying a Hanning window and a rectangular window respectively with the isolated one of first order sidelobes. Since the leakage occurring in the frequency domain is well known and already noticed in most applications as the frequency leakage, a weighted window function (Hanning window) was always used with the sampled data in both new and traditional methods. The phase function in that single line was reconstructed with using a weighted window function and without using any weighted window function except for a rectangular window is shown in Figure II.3.2 and Figure II.3.3 separately.

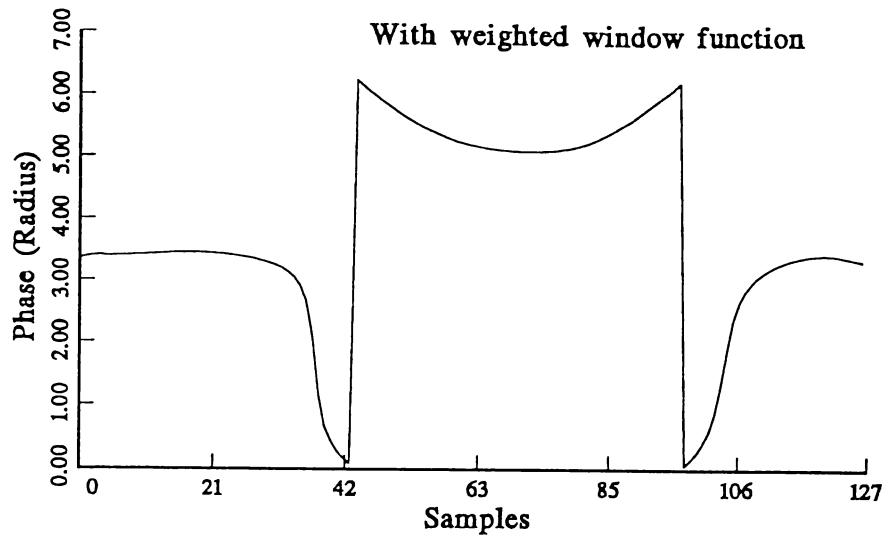


Figure II.3.2: Phase variation in a single line reconstructed by using a Hanning window with the isolated sidelobe

Although the phase function reconstructed was wrapped as expected, there were less ripples on the curve of phase variation constructed by using the Hanning window. It is clear that the ripples were caused by the leakage in the spatial domain due to the discontinuities at both ends of the isolated sidelobe when using a rectangular window.

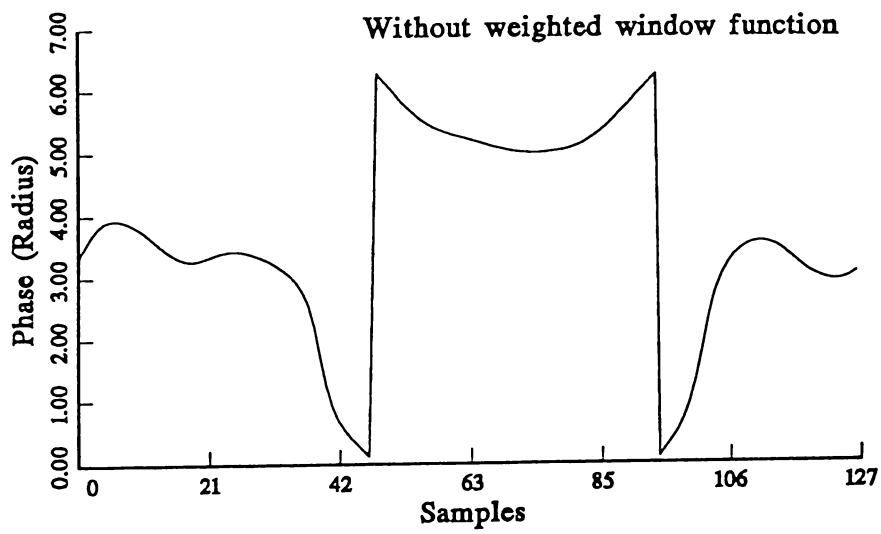


Figure II.3.3: Phase variation in a single line reconstructed by using a rectangular window with the isolated sidelobe

This comparison has clearly shown that the weighted window function used with the isolated sidelobe can dramatically reduce the leakage in the spatial domain so as to improve the accuracy of the phase variation reconstructed directly from the 1-D FFT and inverse FFT.

§ II.3.2.2 Bandpass Filter

The bandpass filter plays an important role in isolation of the desired sidelobe as described in the last chapter. In the new image processing-based methods, the bandwidth of bandpass filter is automatically determined according to the actual spectrum. The cutoff frequencies on both sides of the bandpass filter are selected where the amplitude of power spectrum is reduced to -3 dB from 0 dB of the maximum value. The bandwidth of the bandpass filter is then calculated according to the equation (II-2-1) or (II-2-2). As an example, the phase variation in the same line of sampled data as the above-shown was reconstructed using the different bandwidths of the bandpass filter.

The correct bandwidth of bandpass filter for that line of the sampled data is approximately equal to (0.6 * carrier frequency f_c). The phase variation in a single line reconstructed using the correct bandwidth of the bandpass filter is shown in Figure II.3.4.

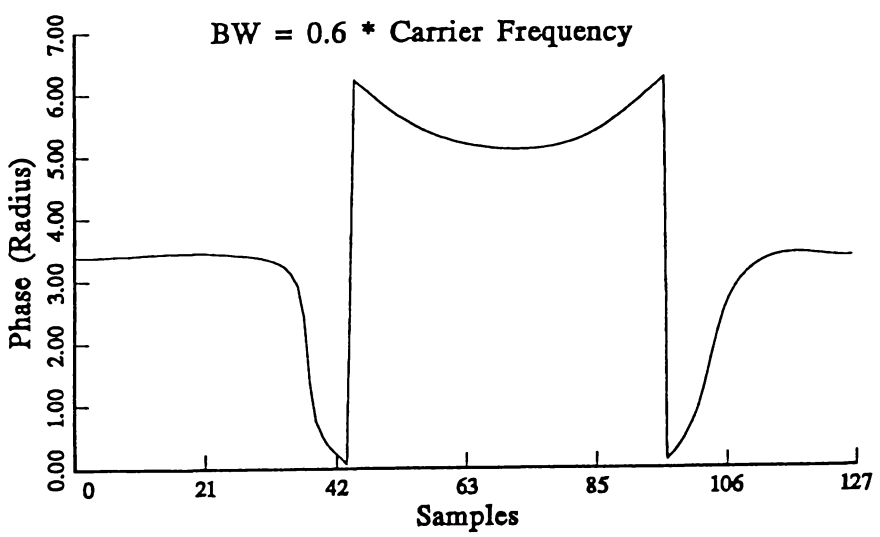


Figure II.3.4: Phase variation in a single line reconstructed using the correct bandwidth of the bandpass filter

Then the bandwidth of the bandpass filter was reduced to (0.4 * carrier frequency f_c) and increased to (1.5 * carrier frequency f_c) respectively and the resulting phase variations using those two incorrect bandwidths of the bandpass filter are shown in Figure II.3.5 and Figure II.3.6 separately.

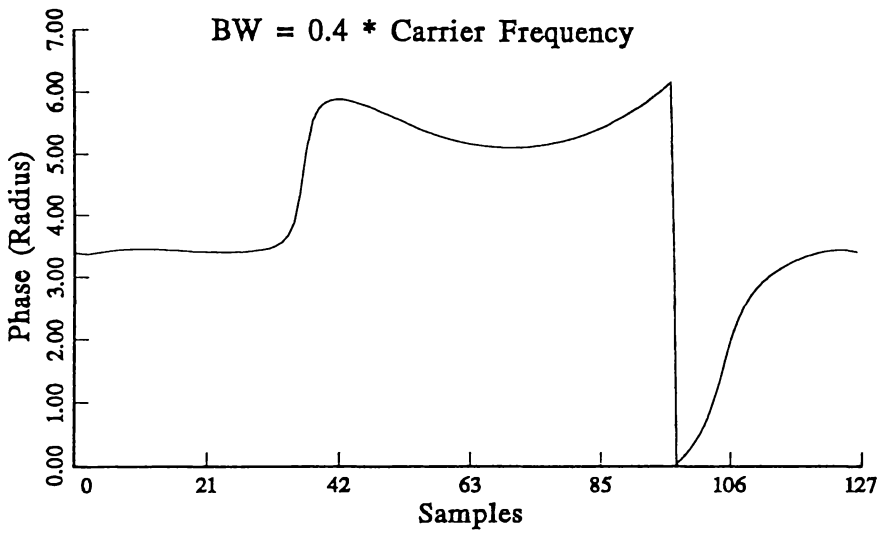


Figure II.3.5: Phase variation in a single line reconstructed using a narrow bandwidth of the bandpass filter

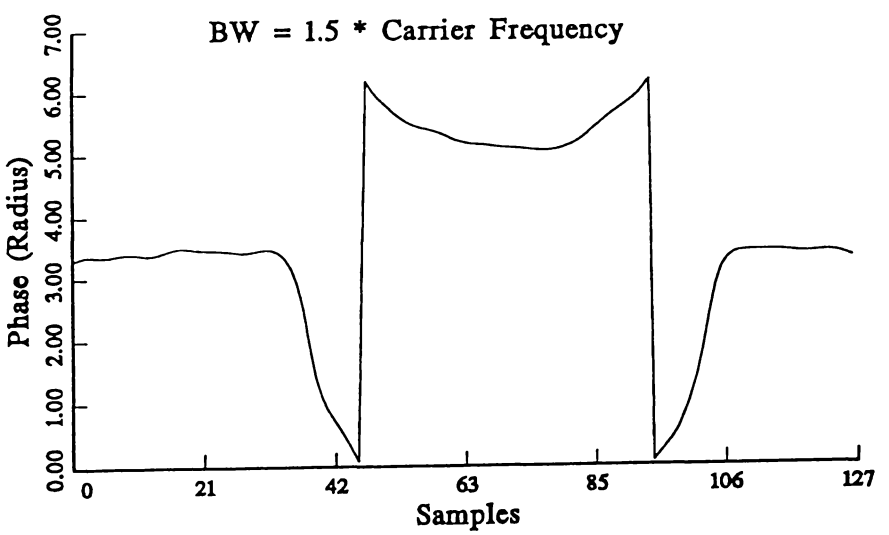


Figure II.3.6: Phase variation in a single line reconstructed using a wide bandwidth of the bandpass filter

It can be seen from the above-shown results that the reconstructed phase variation in a single line becomes less accurate as the bandwidth of the bandpass filter becomes too narrow or too wide. As the bandwidth is too narrow some phase information on that line would not be recovered , because the frequency components of phase variation are excluded by the narrow bandpass filter. In addition, as the bandwidth is too wide many small ripples appear on the recovered phase variation. This is because the high frequency components of noise outside the desired first order sidelobe are incorrectly included by the wider bandpass filter. Only the bandpass filter with a correct bandwidth can recover the accurate phase information.

§ II.3.3 Measured Phase and Height Distributions

The above intermediate results have shown that using both weighted window functions and the correct bandpass filter can improve the accuracy of the measured phase variation on a single line. The experimental results have also shown that using the above two new image processing-based methods on all lines in a fringe pattern can finally improve the accuracy of the measured phase and height distributions on the entire surface of the 3-D object and the reference plane.

A typical example is to measure the profile of an ovine saddle using Fourier transform profilometry in the Meat Research Industry Institute of New Zealand. The surface of the selected ovine saddle was reasonably smooth, but the measured phase or height distribution on the saddle surface showed noisy ripples when using"the traditional methods. The measured phase distribution on the saddle surface using the traditional methods is shown in Figure II.3.7.

But those noisy ripples were dramatically decreased when using the above-shown two new methods. The measured phase distribution on the saddle surface using the new methods is shown in Figure II.3.8. The concave surface of the phase distribution in that figure will become the convex surface of the height distribution after the height conversion without losing any resolution.

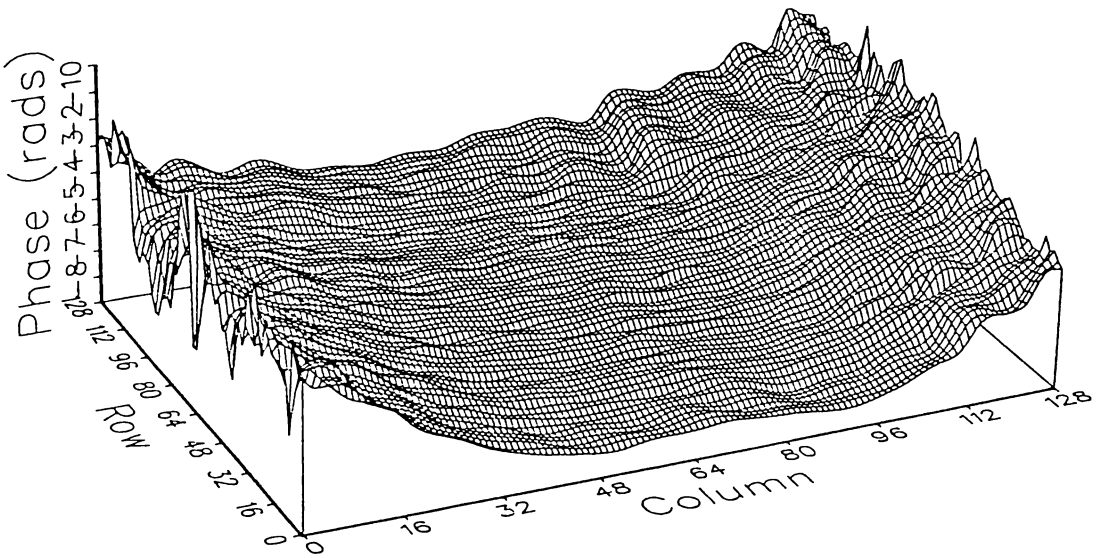


Figure II.3.7: Measured phase variation on the surface of an ovine saddle by using the traditional methods

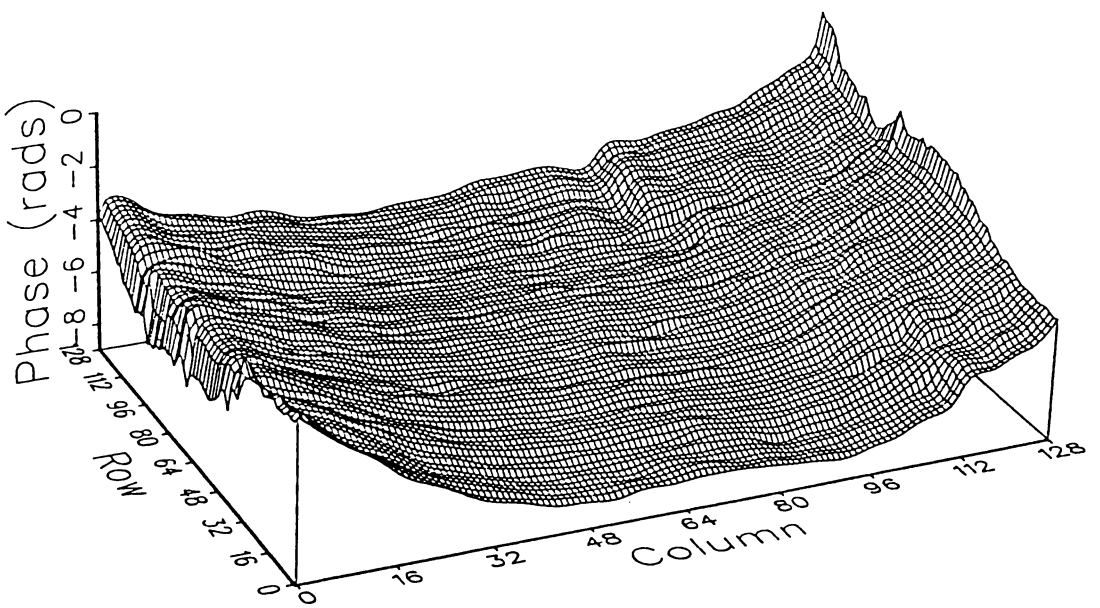


Figure II.3.8: Measured phase variation on the surface of an ovine saddle by using the new methods

The hemisphere shown in Figure II.2.1 that was reconstructed using the traditional methods was again measured using the above-shown two new methods. The measured height distribution of the hemisphere surface using the new methods is shown in Figure II. 3. 9 and the previous result is re-printed in Figure II.3.10 for comparison. The diameter of the test hemisphere was 50 mm.

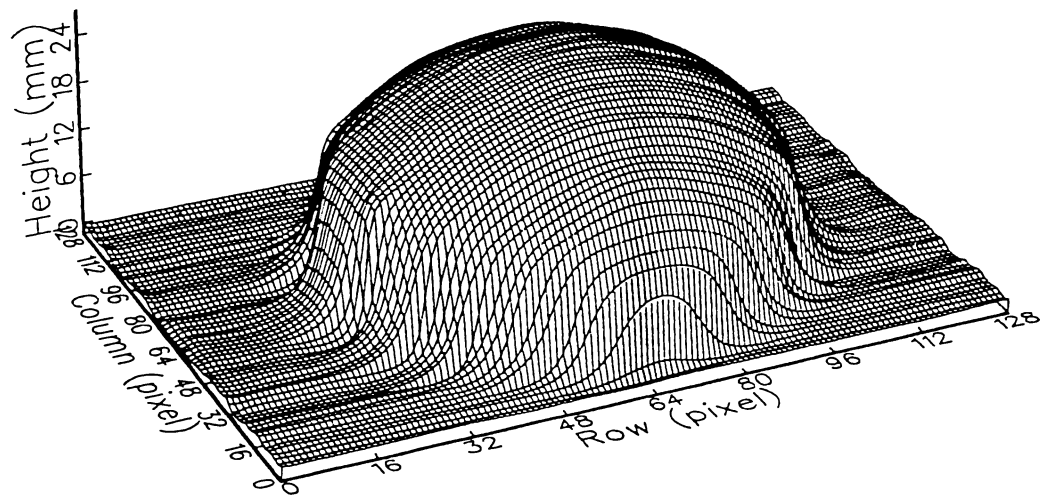


Figure II.3.9: Measured height distribution of the hemisphere using the new methods

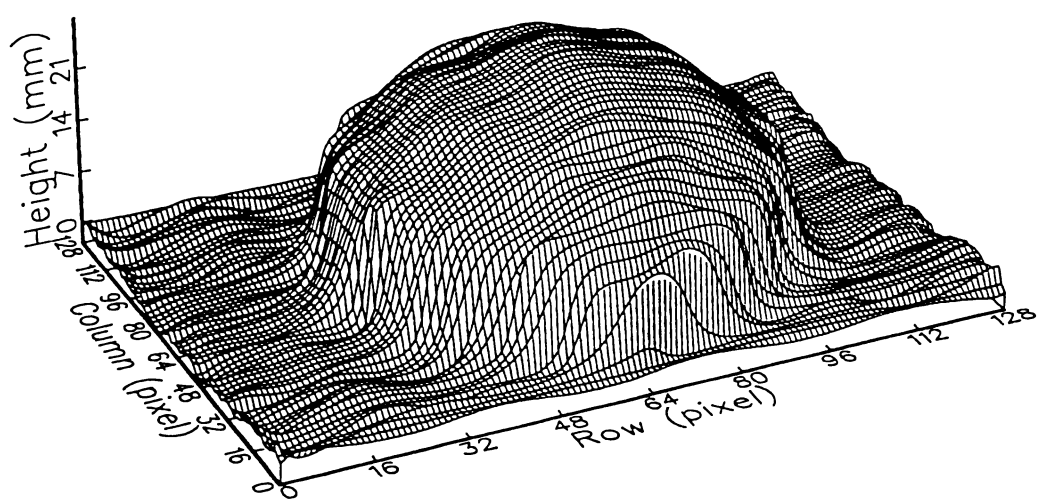


Figure II.3.10: Measured height distribution of the hemisphere using the traditional methods

Similar to the example of the ovine saddle, the uneven reference plane and the coarse surface of the hemisphere reconstructed using the traditional methods became more even and smooth respectively after using the new methods. This can be seen from the mesh on the reference plane and the surfaces of the hemisphere in both figures. The comparison of both results obtained using the traditional and new methods has again shown that using the weighted window function and the correct bandpass filter can improve the accuracy of the measured phase and height distributions on the entire surface of 3-D object and the reference plane.

However, the measured height distribution around the edges of the hemisphere was still not correct compared to the actual situation. The actual situation was that the hemisphere had very clear edges on the reference plane. The reason for failure was the high values of the hemisphere surface height derivatives in the x and y directions even though the actual height was not high. This problem cannot easily solved because there is a height constraint in measurement using Fourier transform profilometry that is based on the derivative of the surface height to be measured. The next section shows the results of using the object boundary guided phase unwrapping algorithm in the new image processing-based methods to solve this problem and the relevant large-scale discontinuities in the wrapped phase map.

§ II.3.4 Object Boundary Guided Phase Unwrapping

Although the phase unwrapping algorithm used in the traditional methods is efficient in most cases, it still has difficulty with the large-scale discontinuity that often occurs at the object boundary. To overcome this difficulty, the phase unwrapping is performed after the object boundary is detected in the new image processing-based methods. The object boundary is found by using the Sobel edge operator combined with the B-spline smooth algorithm described in the last chapter. The phase unwrapping is then performed under the guidance of the object boundary.

As an example, the profile of a 12" fan blade was measured using Fourier transform profilometry. The fringe pattern of that fan blade is shown in Figure II.3.11.

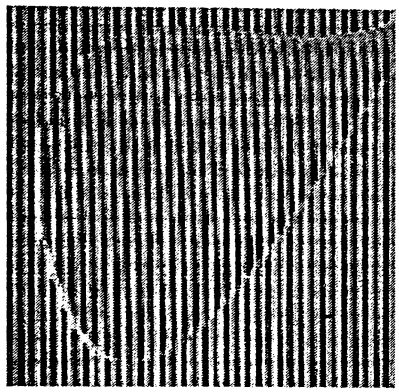


Figure II.3.11: The fringe pattern of a 12" fan blade

There was a large-scale discontinuity around the boundary of the blade on the reference plane. It is almost impossible to obtain the correct height distribution of the blade surface using the traditional methods. This is because the discontinuity around the boundary of the blade is associated with high values of height derivative that exceeded the constraint on the height measurement in Fourier transform profilometry. The height distribution of the fan blade that was unsuccessfully reconstructed by using the traditional methods is shown in Figure II.3.12.

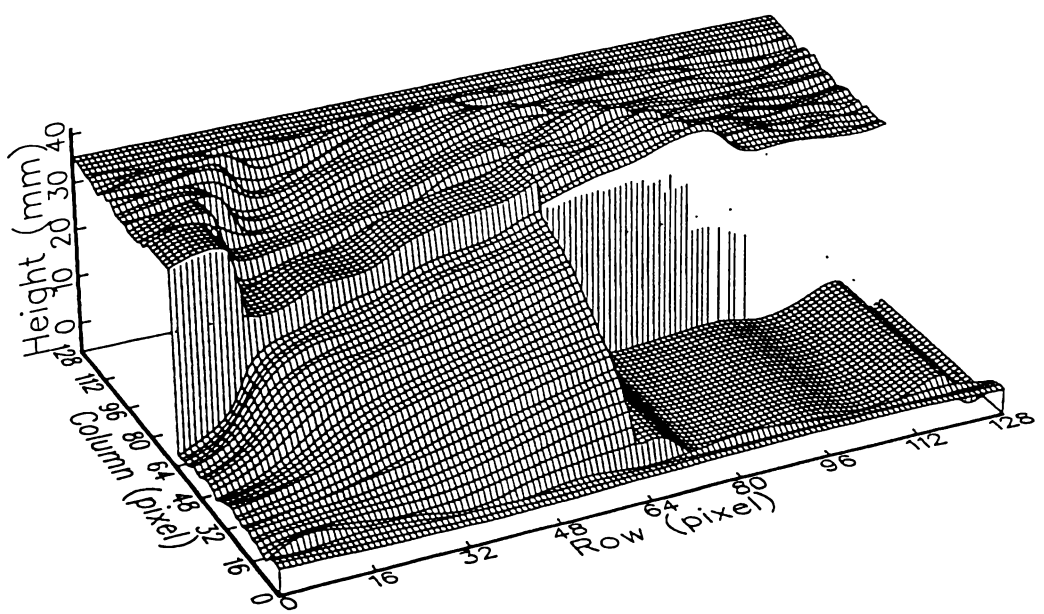


Figure II.3.12: Height distribution of the fan blade unsuccessfully reconstructed by using the traditional methods

In the new image processing-based methods, the edges of the fan blade was detected using the Sobel edge operator in the y axis and the boundary of the fan blade was then formed after the missing edge points were estimated by using the B-spline smooth algorithm. The detected boundary of the fan blade is shown in Figure II.3.13.

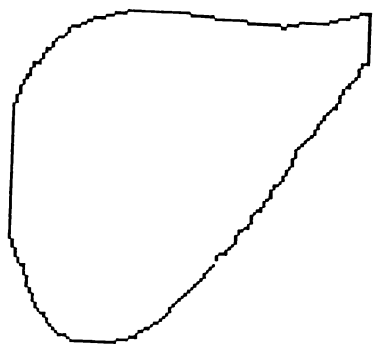


Figure II.3.13: Detected boundary of the 12" fan blade

After the boundary of the fan blade was found, the phase unwrapping was then performed under the guidance of the boundary information, i.e., only the phases within the object boundary would be unwrapped if required. The algorithm used here was similar to that in the traditional methods except for the starting point. The starting point for phase unwrapping was selected at the object centre.

Finally the unwrapped phase distribution of the surface of the fan blade was adjusted by a phase offset based on the difference between the average phase on the reference plane and the maximum phase on the surface of the fan blade (as described in the previous chapter). The resulting height distribution of the fan blade is shown in Figure II.3.14.

It is clear that using the object boundary guided phase unwrapping algorithm can solve the large-scale discontinuity problem that normally occurs around the object boundary. This problem is almost impossible to solve using the traditional methods and it is why so many researchers in this area are currently investigating new phase unwrapping algorithms.

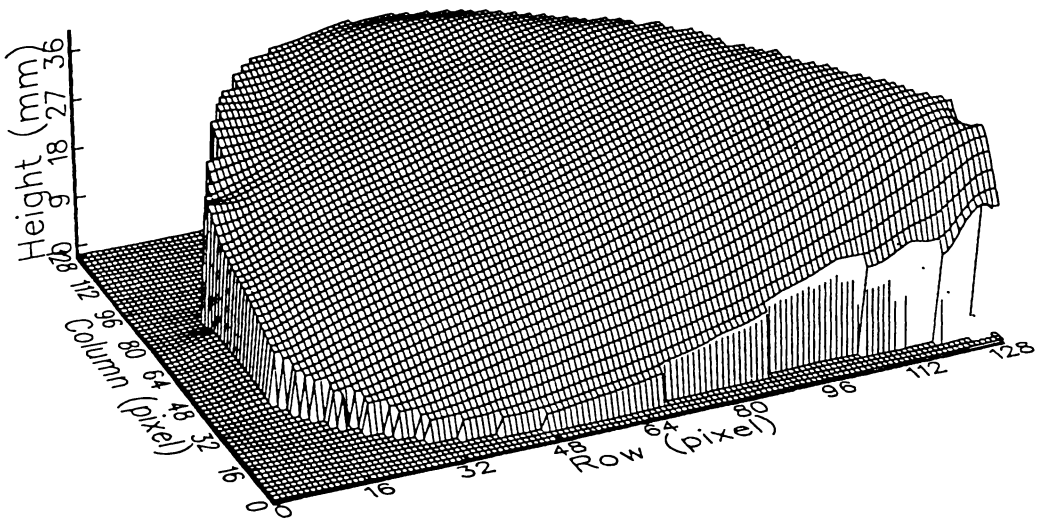


Figure II.3.14: Height distribution of the fan blade reconstructed by using object boundary guided phase unwrapping

The problem that was mentioned early in Figure II.3.9 can also be easily solved using the object boundary guided phase unwrapping algorithm. The result is shown in Figure II.3.15.

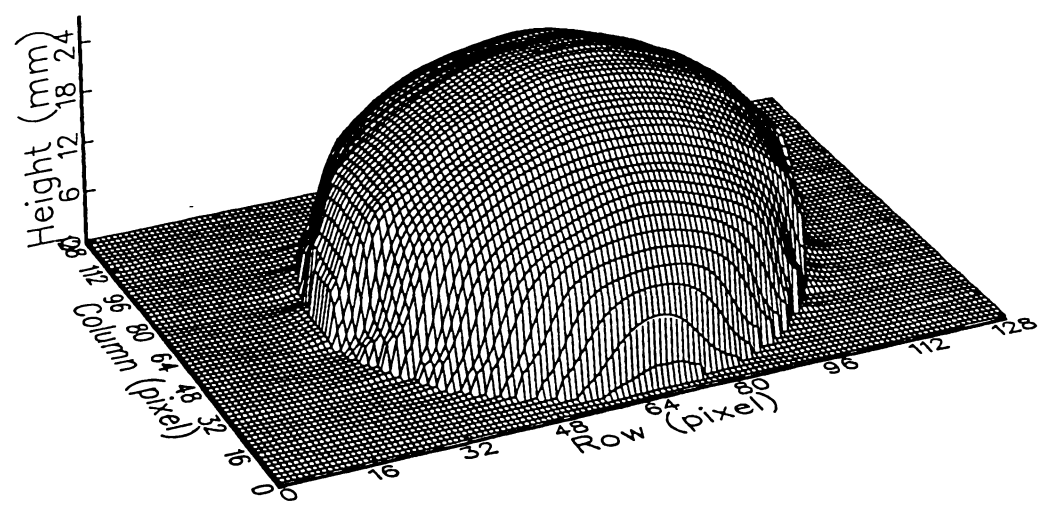


Figure II.3.15: Measured height distribution of the hemisphere using the object boundary guided phase unwrapping algorithm

The improvement around the hemisphere boundary is obvious after comparing the above result with the one shown in Figure II.3.9. To know quantitatively how well the new methods improve the overall measurement of 3-D object surface over the traditional methods, I used a computer-generated hemisphere based on the actual size of test hemisphere and its position in the fringe pattern to calculate the errors between the measured hemispheres and the test hemisphere. This computer-generated hemisphere is shown in Figure II.3.16. The mean and standard deviation of those errors are shown in Table II.3.1.

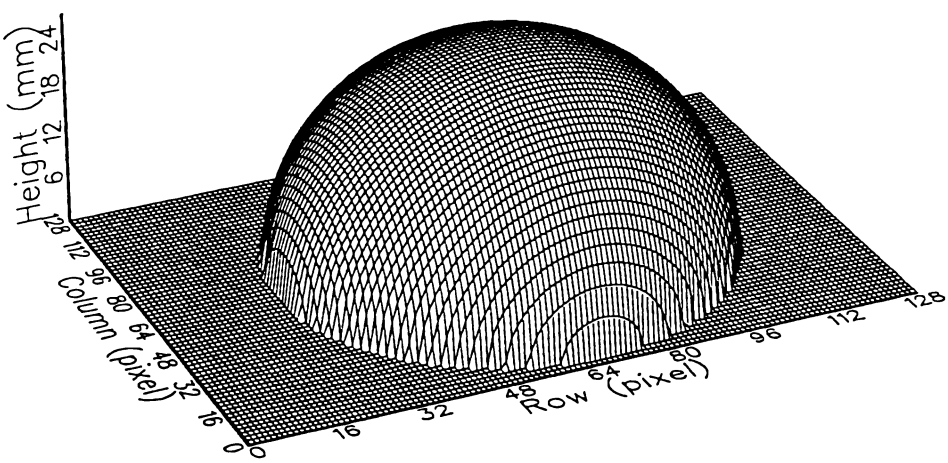


Figure II.3.16: A computer-generated hemisphere

Table II.3.1: Mean and standard deviation of errors between the measured hemispheres and the actual test hemisphere

Measured hemispheres	Mean (mm)	Std. dev. (mm)
Using traditional methods	0.979	2.146
Using new methods (1)[1]	0.632	1.350
Using new methods (2)[2]	0.513	1.423

1 --- without using the object boundary guided phase unwrapping

2 --- with using the object boundary guided phase unwrapping

As another example, the profile of a thick rubber ring was measured using both new methods and the traditional methods. The result obtained using the new methods is shown in Figure II.3.17 and the result obtained using the traditional methods is shown in Figure II.3. 18.

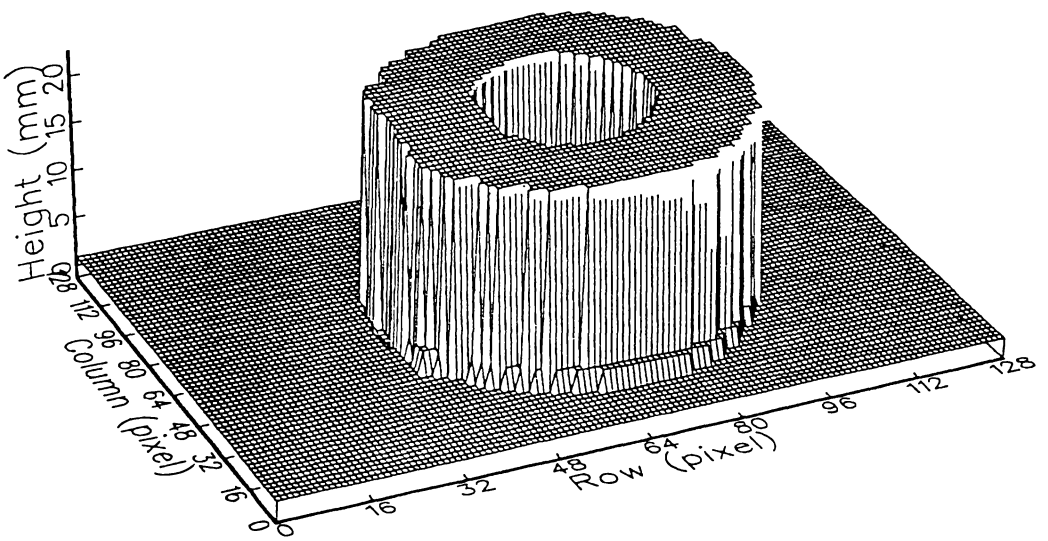


Figure II.3.17: Measured profile of a thick rubber ring using the new methods

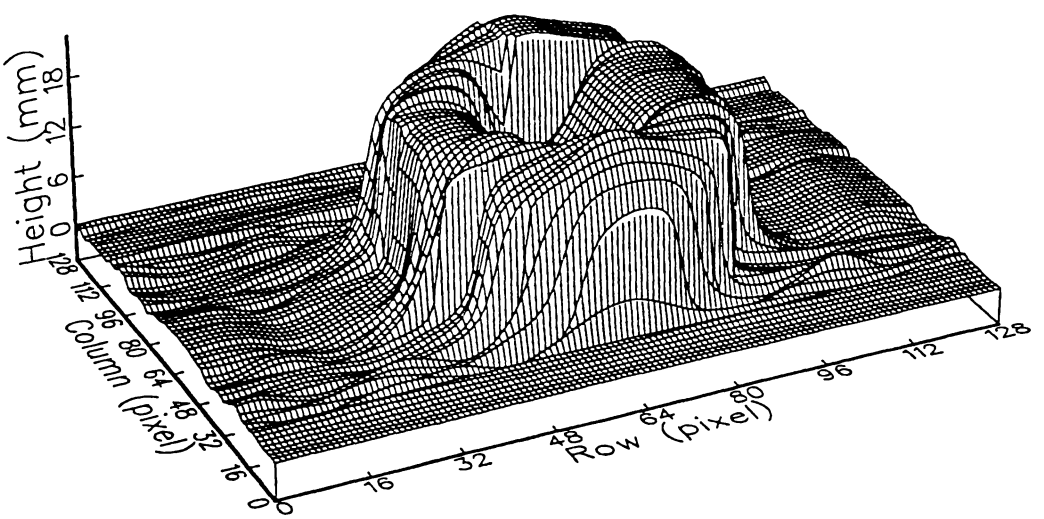


Figure II.3.18: Measured profile of a thick rubber ring using the traditional methods

PART II CHAPTER 4

CONCLUSIONS AND SUGGESTIONS

§ II.4.1 Conclusions

Fourier transform profilometry has been proved to be one of the best techniques for nondestructive measurement of 3-D object surfaces to the industrial end-user. To improve the accuracy of measurement, I have carefully analysed potential major causes of error in the traditional Takeda's methods and proposed a number of new image processing-based methods. The new methods include application of weighted window function to the isolated first sidelobe in the frequency domain, automatic determination of the bandwidth of bandpass filter based on the actual spectrum and use of object boundary guided phase unwrapping to solve large-scale discontinuities around the object boundary on the modulo 2π phase map.

After being tested over some typical 3-D objects, the new image processing-based methods have been proved to be superior to the traditional Takeda's methods in many aspects. The weighted window function used with the isolated first sidelobe has dramatically reduced the leakage error in each line of sampled data in the spatial domain. Consequently not only the correct phase variations are obtained directly from the 1-D FFT and inverse FFT but also the measured entire height distributions of the 3-D object and the reference plane are improved.

In addition the automatic determination of the bandwidth of bandpass filter based on the actual spectrum is able to correctly isolate the desired first sidelobe without containing any unnecessary high frequency noise or filtering out any part of the desired phase modulated spectrum. The resulting phase variation recovered better represents the actual situation, and the reconstructed profile of 3-D object surface is improved.

The large-scale discontinuity has been a major problem in the Fourier transform profilometry for many years. Some algorithms for phase unwrapping to solve this problem have been investigated, but they are too expensive in computation and complicated in implementation such that they are not suited to industrial applications. The object boundary guided phase unwrapping proposed in my thesis is simple but has effectively solved the problem of large-scale discontinuities that usually occur around an object boundary. The object boundary is first identified using Sobel or the smoothed edge operator plus the B-spline curve-smoothing algorithm and then the traditional scanning algorithm for phase unwrapping is used to correct the discontinuities on the modulo 2π phase map that is generated by a computer-generated arctangent routine. Since the operation of the phase unwrapping is performed only within the object boundary, the large-scale discontinuity around the object boundary never becomes a problem and also the time spent on phase unwrapping operation is reduced.

§ II.4.2 Suggestions

Although the accuracy of measurement of the 3-D object surfaces has been dramatically improved using a number of new image processing-based methods proposed in my thesis, the further improvement is still possible if the following suggestions are considered in the further work.

a) Detection of Object Boundary

In my experiments, the object boundary was detected from the fringe pattern using the Sobel or the smoothed edge operator plus the B-spline curve-smoothing algorithm. However, the strong fringe edges affected the detection of the edge points of the object. Consequently only half of that edge operator in the direction parallel to the lines of grating was used such that many of the missing edge points of the object must be estimated using the B-spline curve-smoothing algorithm. Since the estimated missing edge points were not accurate, the final object boundary used for guiding the phase unwrapping did not exactly match the actual situation on the modulo 2π phase map. This would affect the final measurement of the 3-D object surface, especially around the object boundary.

To improve the accuracy of the measurement of the 3-D object surface around the object boundary, the accurate object boundary must be obtained. There are several ways to improve the detection of the object boundary. It may be possible to find some better algorithms to detect the object boundary from the fringe pattern, which include the edge operator and the edge estimation. In addition, it may be advantageous to grab an extra image of the same object without using the grating. This image can then be used for the detection of the object boundary only. The image can be grabbed using the mirror and another camera without changing the original optical system.

b) Detection of Invalid Pixels

Although the lighting was carefully adjusted in my experiments to avoid any saturation in digitizing the fringe images of the 3-D objects, the actual reflection varies with the object surfaces to be measured. Consequently, some pixel values in the digitized image would be saturated. Also the fringe image may have some speckle noise and random noise. Those invalid pixels will disturb the phase unwrapping and further processing of the relevant data. Of course, the saturation can be avoided by carefully adjusting the lighting based on the actual situation, but this method is not practical to the industrial applications. In addition, noise is inevitable.

To reduce those invalid pixels, the fringe image pre-processing is generally required. Typically, the medium filter will be applied such that the value at a pixel is set to the average of the grey scales of its eight nearest neighbours. This operation is to reduce high-frequency noise and maintain the low-frequency fringe spacing information. Also, the invalid pixels due to saturation may be detected if one of their four nearest neighbours also has the maximum grey value 255. Those pixels are marked in a binary image that can be used as a mask during phase unwrapping.

PART II APPENDIX A

THE TRADITIONAL TAKEDA'S METHODS USED IN FOURIER TRANSFORM PROFILOMETRY

§ II.A.1 Introduction

Fourier transform profilometry was first proposed by Takeda in 1983 (Takeda, 1983). Since it does not use the interference fringe patterns, Fourier transform profilometry does not have any of the difficulties as associated with the moiré contouring techniques. Also Fourier transform profilometry has much higher sensitivity than the conventional moiré technique because the minimum variation on the height distribution generated in Fourier transform profilometry is not limited by one contour fringe as in the moiré contouring technique. Therefore, the Fourier transform profilometry has been an attractive technique for nondestructive measurement of three-dimensional (3-D) object surface since then.

The details of Fourier transform profilometry will be examined in this appendix, which is based on a description by Takeda (1982, 1983). The major aspects include the optical system used in Fourier transform profilometry, the Fourier transform method, phase unwrapping, phase-to-height conversion and height constraint on measurement of 3-D object surfaces.

§ II.A.2 Optical System

The optical system used in Fourier transform profilometry is similar to that used in conventional interferometry. Two different geometries of the optical system are commonly used in Fourier transform profilometry and one has some merits over the other as well as some demerits.

The optical system shown in Figure II.A.1 is called the crossed-optical-axes geometry. The optical axes of a projector and a camera lie in the same plane and intersect at a point O near the centre of the object surface. This geometry is easy to

construct because the grating G can be placed on the optical axis E'pEp of the projector, but it does not give planar contours unless the lens of the projector is telecentric (i.e., the chief rays resulted from a telecentric lens are parallel to the optical axis in image space and the exit pupil is at infinity.)

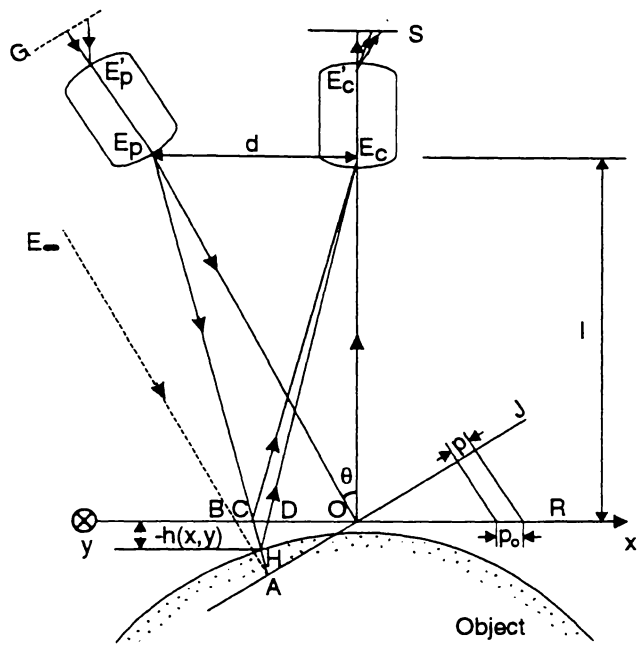


Figure II.A.1: Crossed-optical-axes geometry

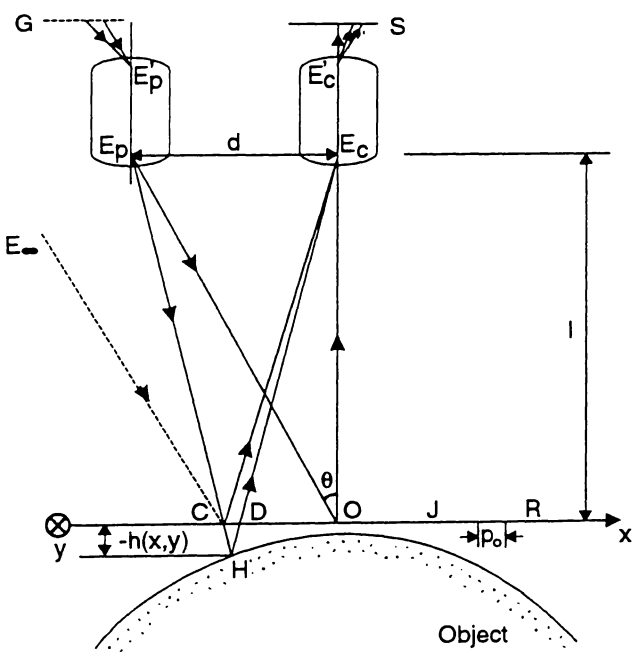


Figure II.A.2: Parallel-optical-axes geometry

Figure II.A.2 shows the parallel-optical-axes geometry that has the optical axes of a projector and a camera lying in the same plane but parallel. This geometry does give planar contours but the grating must be placed far off the optical axis of the projector to ensure the grating image is within the view area of the camera.

§ II.A.3 Grating image

In the crossed-optical-axes geometry shown in Figure II.A.1, R is a fictitious plane normal to the optical axis E'cEc of the camera lens and serves as a reference plane from which the object height $h(x,y)$ is measured. The conjugate image of grating G is formed by the projector lens on plane J through point O. First, the object is assumed to be a flat and uniform plane on the reference plane R. If the lens of the projector is telecentric (as denoted by E_∞), the grating image $g_{to}(x,y)$ projected on the object surface (the reference plane here) and observed through point E_c is a regular grating pattern that can be expressed by a Fourier series expansion:

$$g_{to}(x,y) = \sum_{n=-\infty}^{\infty} A_n \, e^{j2\pi n f_c x} \qquad \text{(II-A-1)}$$

where

$$f_c = \frac{1}{p_o} = \frac{\cos\theta}{p} \qquad \text{(II-A-2)}$$

is the fundamental frequency of the observed regular grating image. The x axis is chosen from left to right in the figure and the y axis is normal to the figure plane. The principal ray through point A strikes at point B on the reference plane. If the lens of projector is nontelecentric, the grating image projected on the reference plane is deformed. The pitch of the deformed grating image is increasing with x. The deformed grating image observed through point E_c is a deformed grating pattern and is normally expressed by a Fourier series:

$$g_0(x,y) = \sum_{n=-\infty}^{\infty} A_n \, e^{j2\pi n f_c [x + s_o(x)]} \qquad \text{(II-A-3)}$$

where $s_o(x)$ = BC and has a positive sign when C is to the right of B as in the figure.

For convenience, the deformed grating image shown in (II-A-3) for the nontelecentric lens of projector when $h(x,y) = 0$ can be interpreted as multiple signals with spatial carrier frequencies nf_c modulated by initial phase $\phi_0(x,y)$ and rewritten as

$$g_0(x,y) = \sum_{n=-\infty}^{\infty} A_n \cdot e^{j2[\pi n f_c x + n\phi_0(x)]} \qquad \text{(II-A-4)}$$

where

$$\phi_0(x) = 2\pi f_c s_0(x) \qquad \text{(II-A-5)}$$

If the object has varying height $h(x,y)$, the principal ray E_pA strikes the object surface at point H that is seen to be a point D on the reference plane. Therefore, the deformed grating image on the 3-D object surface is generally given by (II-A-6) or (II-A-7).

$$g(x,y) = r(x,y) \cdot \sum_{n=-\infty}^{\infty} A_n \, e^{j2\pi n f_c [x + s(x,y)]} \qquad \text{(II-A-6)}$$

or

$$g(x,y) = r(x,y) \cdot \sum_{n=-\infty}^{\infty} A_n \cdot e^{j2[\pi n f_c x + n\phi(x,y)]} \qquad \text{(II-2-7)}$$

where $r(x,y)$ is a nonuniform distribution of reflectivity on the object surface and

$$\phi(x,y) = 2\pi f_c s(x,y) = 2\pi f_c BD \qquad \text{(II-A-8)}$$

In the parallel-optical-axis geometry shown in Figure II.A.2, the optical axes of both the projector and the camera are parallel and normal to the reference plane. When the conjugate image of grating G is formed on the reference plane, three points A, B, and

C in Figure II.A.1 degenerate into point C in Figure II.A.2. Consequently, the grating image projected on a flat and uniform plane on the reference plane R remains a regular grating pattern that is same as the form expressed in (II-A-1) for the case of telecentric lens of projector in crossed-optical-axes geometry. The parallel-optical-axis geometry brings a merit of generating planar contour when using the nontelecentric lens of projector, but the optical system looks more or less awkward because the grating must be put far off the optical axis of the project lens in order to keep its image within the view area of the camera.

Although the parallel-optical-axis geometry normally offers a regular grating image for $h(x,y) = 0$, which theoretically has the same form as that shown in (II-A-1) for the case of telecentric lens of project in crossed-optical-axes geometry, yet there is still some initial phase modulation due to the misalignments and/or distortion of both lenses. Consequently, the grating image for $h(x,y) = 0$ in parallel-optical-axis geometry should have the same form as shown in (II-A-4) for the crossed-optical-axes geometry. In addition, the deformed grating image projected on the 3-D object surface is expressed by the same Fourier series shown in (II-A-6) or (II-A-7) except for $s(x,y) = \text{CD}$.

§ II.A.4 Fourier Transform Method

The phase $\phi(x,y)$ in the deformed grating image or the phase-modulated signals shown in (II-A-7) contains the desired information of the 3-D object surface, but the amplitude $r(x,y)$ is the unwanted signal caused by nonuniform reflectivity on the object surface. Using the Fourier transform method they can be separated. The details are described as follows.

Since the lines of the grating are normal to the x axis, the spatial carrier frequency f_c appears on the x axis only. Therefore, one-dimensional (1-D) Fourier transforms with respect to the variable x are performed line by line along the y direction with the variable y being fixed. According to sampling theory, sampling in the time domain results in a periodic function of frequency in the frequency domain. The spectra of sampled grating image $g(x,y)$ for a fixed y value can then be expressed by a sampling

form as shown in (II-A-9) and displayed in Figure II.A.3.

$$G(f,y) = \sum_{n=-\infty}^{\infty} Q_n(f - nf_c, y) \qquad \text{(II-A-9)}$$

Usually, the desired phase $\phi(x,y)$ and the unwanted amplitude variation $r(x,y)$ vary slowly compared with the spatial carrier frequency f_c so that sidelobes in the spectra are separated from each other. If the first sidelobe denoted Q_1 in Figure II.2.3 is filtered out and its inverse Fourier transform is carried out, we can obtain a complex signal

$$\hat{g}(x,y) = A_1 r(x,y) \cdot e^{j[2\pi f_c x + \phi(x,y)]} \qquad \text{(II-A-10)}$$

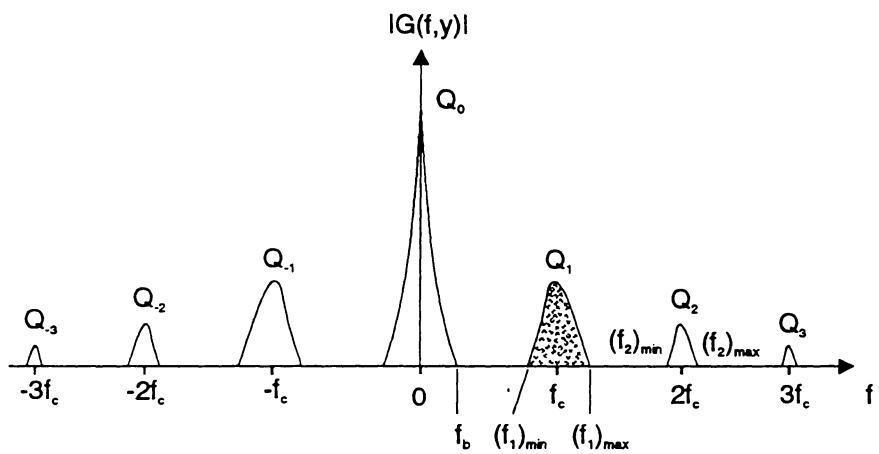


Figure II.A.3: The spectra of deformed grating image for a fixed y value

After the same operation is performed for the grating image on the reference plane, we obtain a similar complex signal

$$\hat{g}_0(x,y) = A_1 \cdot e^{j[2\pi f_c x + \phi_0(x,y)]} \qquad \text{(II-A-11)}$$

Multiplying (II-A-10) with the conjugate of (II-A-11) generates a new complex signal

$$\hat{g}(x,y) \cdot \hat{g}_0^*(x,y) = |A_1|^2 r(x,y) \cdot e^{j[\Delta\phi(x,y)]} \qquad \text{(II-A-12)}$$

where

$$\begin{aligned} \Delta\phi(x,y) &= \phi(x,y) - \phi_0(x,y) \\ &= 2\pi f_c(BD-BC) \\ &= 2\pi f_c CD \end{aligned} \qquad \text{(II-A-13)}$$

Since both $|A_1|^2 r(x,y)$ and $\Delta\phi(x,y)$ in (II-A-12) are real functions, the phase distribution $\Delta\phi(x,y)$ can finally be obtained by the arc-tangent function

$$\Delta\phi(x,y) = \tan^{-1}\left[\frac{Im[\hat{g}(x,y) * \hat{g}_0^*(x,y)]}{Re[\hat{g}(x,y) * \hat{g}_0^*(x,y)]}\right] \qquad \text{(II-A-14)}$$

where Im[ ] and Re[ ] represent the imaginary and real components respectively.

§ II.A.5 Phase Unwrapping

The phase $\Delta\phi(x,y)$ in (II-A-14) that is normally obtained by a computer-generated routine can only give a principal value ranging from $-\pi$ to π. Consequently, the phase distribution $\Delta\phi(x,y)$ is wrapped into this range and has discontinuities with 2π phase jumps for variations more than 2π. An example of phase discontinuities is shown in Figure II.A.4 (a). These discontinuities must be corrected by the phase unwrapping algorithm in Fourier transform profilometry.

In the phase unwrapping algorithm, an offset phase distribution $\phi_o(x,y)$ is to be determined and added to the discontinuous phase distribution $\phi_d(x,y)$ to convert it to a continuous phase distribution $\phi_c(x,y)$ as shown in (II-A-15).

$$\phi_c(x,y) = \phi_d(x,y) + \phi_o(x,y) \qquad \text{(II-A-15)}$$

The algorithm consists of two steps. The first step is to compute the phase difference between the ith sample point and the point preceding it:

$$\Delta\phi_d(x_i, y) = \phi_d(x_i, y) - \phi_d(x_{i-1}, y) \qquad \text{(II-A-16)}$$

where i is from 1 to N to cover all the sample points along the x direction. Since the variation of the phase difference is normally slow compared with the sampling interval, the absolute value of phase difference $|\Delta\phi_d(x_i, y)|$ is much less than 2π at the point where the phase distribution is continuous. However it becomes almost 2π at the points where the 2π phase jump happens. To find all the points where the 2π phase jump occurs, an appropriate threshold close to 2π is set for the absolute phase difference. Based on the sign of phase difference $\Delta\phi_d(x_i, y)$, the direction of phase jump can also be determined as shown in Figure II.A.4 (a).

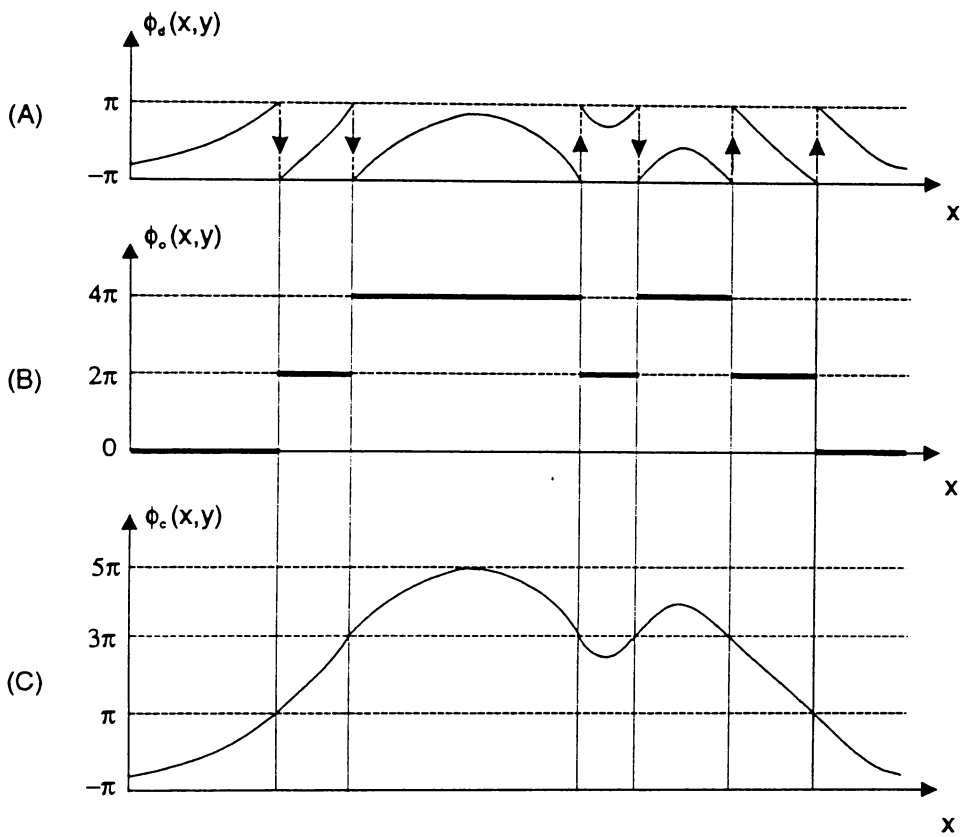


Figure II.A.4: An example of phase discontinuities and phase unwrapping (a) The discontinuous phase distribution; (b) The offset phase distribution for correcting the phase discontinuities in (a); (c) The continuous phase distribution after phase unwrapping.

Then the second step is to determine the phase offset at each sample point

sequentially, starting from the first sample point along the x direction when the variable y is fixed. Since the offset phase distribution to be determined is relative, so the starting offset phase at the first sample point on the x direction is assumed to be zero for every y value. If the first phase jump is met at point k and the direction of the jump detected is negative as shown in Figure II.A.4 (a) by the sign ↓, the offset phase at point k is then set to

$$\phi_o(x_k, y) = \phi_o(k_{k-1}, y) + 2\pi \qquad \text{(II-A-17)}$$

Similarly, if the direction of the phase jump at point k is positive (marked by sign ↑ in Figure II.A.4 (a)), the offset phase at point k becomes

$$\phi_o(x_k, y) = \phi_o(k_{k-1}, y) - 2\pi \qquad \text{(II-A-18)}$$

Next, the above-described procedure is carried out along the remaining sample points on the x direction but using the new starting offset phase. In this case the new starting offset phase is $\phi_o(x_k, y)$. In this way, the offset phase distribution along the x direction is found as shown in Figure II.A.4 (b). The continuous phase distribution is easily obtained by adding the offset phase distribution to the discontinuous phase distribution and finally shown in Figure II.A.4 (c).

For measuring the 3-D object surface, a further phase unwrapping operation in the y direction is necessary because the algorithm sets the starting offset phase zero at the first sample point in the x direction without respect to the phase distribution in the y direction. Generally it is sufficient to determine the offset phase distribution in the y direction on only one line (i.e., the variable x is fixed at an arbitrary value). The procedure of phase unwrapping on this line is same as that described for the x direction, with the starting offset phase at the first sample point on that line set to zero. After a complete two-dimensional offset phase distribution is obtained, the continuous phase distribution of the 3-D object surface is finally obtained by adding this offset phase distribution to the relative discontinuous phase distribution as shown in (II-A-15).

§ II.A.6 Phase-To-Height Conversion

Once the continuous phase distribution of 3-D object surface is obtained, it can easily be converted into the physical height distribution according to the triangular relation of optical geometry shown in Figure II.A.1 or Figure II.A.2. From either figure, it is noticed that $\Delta E_p HE_c$ is analogous to ΔCHD so that a simple relation is established in (II-A-19).

$$CD = \frac{-h(x,y)\cdot d}{[l - h(x,y)]} \qquad \text{(II-A-19)}$$

where the object height $h(x,y)$ has been defined negative as measured downwards from the reference plane R. Finally, the height of 3-D object surface is obtained by substituting (II-A-19) into (II-A-13) and solving it for $h(x,y)$.

$$h(x,y) = \frac{l\cdot\Delta\phi(x,y)}{\Delta\phi(x,y) - 2\pi f_c d} \qquad \text{(II-A-20)}$$

§ II.A.7 Height Constraint

As described early, Fourier transform profilometry is based on the assumption that the desired phase $\phi(x,y)$ and the unwanted nonuniform reflectivity $r(x,y)$ vary slowly compared with the spatial carrier frequency f_c so that sidelobes in the spectra are separated from each other. This assumption limits the range of height that can be measured using Fourier transform profilometry. The maximum height that can be measured using Fourier transform profilometry is derived as follows.

Since the grating image $g(x,y)$ is a phase-modulated signal, the frequency component f_n in the nth sidelobe can be obtained by the derivative of $g(x,y)$ as is usual for FM signals .

$$\begin{aligned} f_n &= \frac{1}{2\pi}\cdot\frac{\partial}{\partial x}[2\pi n f_c x + n\phi(x,y)] \\ &= nf_c + \frac{n}{2\pi}\cdot\frac{\partial\phi(x,y)}{\partial x} \end{aligned} \qquad \text{(II-A-21)}$$

To guarantee the first sidelobe in the spectra being separated from others, the conditions shown in (II-A-22) must be met. Those conditions are easily understood

from Figure II.A.3.

$$[(f_1)_{max} < (f_n)_{min}] \wedge [f_b < (f_1)_{min}], \quad (n=2,3\ldots) \tag{II-A-22}$$

where the sign $\wedge$ represents the logic AND that means both conditions must be satisfied.

After substituting (II-A-21) into (II-A-22), those conditions are rewritten and shown in (II-A-23).

$$\begin{aligned} &[f_c+\frac{1}{2\pi}(\frac{\partial\phi}{\partial x})_{max} < nf_c+\frac{n}{2\pi}(\frac{\partial\phi}{\partial x})_{min}] \\ \wedge\ &[f_b < f_c+\frac{1}{2\pi}(\frac{\partial\phi}{\partial x})_{min}], \quad (n=2,3\ldots) \end{aligned} \tag{II-A-23}$$

If $\left|(\partial\phi/\partial x)_{max}\right|$ is used to denote the maximum absolute value that is a larger one between $\left|(\partial\phi/\partial x)_{min}\right|$ and $\left|(\partial\phi/\partial x)_{max}\right|$, the conditions shown in (II-A-23) can be safely extended to the conditions shown in (II-A-24) by replacing $(\partial\phi/\partial x)_{min}$ with $-\left|(\partial\phi/\partial x)_{max}\right|$ in (II-A-23).

$$\begin{aligned} &[f_c+\frac{1}{2\pi}\left|\frac{\partial\phi}{\partial x}\right|_{max} < nf_c-\frac{n}{2\pi}\left|\frac{\partial\phi}{\partial x}\right|_{max}] \\ \wedge\ &[f_b < f_c-\frac{1}{2\pi}\left|\frac{\partial\phi}{\partial x}\right|_{max}], \quad (n=2,3\ldots) \end{aligned} \tag{II-A-24}$$

Both inequalities in (II-A-24) are rewritten for $\left|(\partial\phi/\partial x)_{max}\right|$ and shown in (II-A-25).

$$\begin{aligned} &[\left|\frac{\partial\phi}{\partial x}\right|_{max} < 2\pi f_c\left(\frac{n-1}{n+1}\right)] \\ \wedge\ &[\left|\frac{\partial\phi}{\partial x}\right|_{max} < 2\pi(f_c-f_b)], \quad (n=2,3\ldots) \end{aligned} \tag{II-A-25}$$

In most practical cases, f_b is much smaller than the folding frequency $f_c/2$ and also the item (n-1)/(n+1) has the smallest value when n = 2. Therefore, two inequalities are

then combined into one condition shown in (II-A-26).

$$\left|\frac{\partial \phi}{\partial x}\right|_{max} < \frac{2\pi f_c}{3} \qquad \text{(II-A-26)}$$

Since the initial phase $\phi_o(x,y)$ is usually very small, $\Delta\phi(x,y)=\phi(x,y)-\phi_o(x,y)$ can be approximated to $\phi(x,y)$. Then substituting $\Delta\phi(x,y)$ with $\phi(x,y)$ in (II-A-20) results in the following expression.

$$\begin{aligned} \phi(x,y) &= -\frac{2\pi f_c dh(x,y)}{l-h(x,y)} \\ &\approx -\frac{2\pi f_c d}{l}\cdot h(x,y) \end{aligned} \qquad \text{(II-A-27)}$$

where the approximation is based on the fact that l is usually much greater than $h(x,y)$ in most optical systems. Finally substituting (II-A-27) into (II-A-26) produces the height constraint:

$$\left|\frac{\partial h(x,y)}{\partial x}\right|_{max} < \frac{1}{3}\cdot\frac{l}{d} \qquad \text{(II-A-28)}$$

From the above inequality it is seen that the maximum height that can be measured using Fourier transform profilometry is not limited by the height distribution itself but by the derivative of height in the x direction. By adjusting the setting of optical geometry to increase the value of l/d, the maximum height that can be measured using Fourier transform profilometry can be extended.

PART II APPENDIX B

COMPARISON OF DIFFERENT COMBINATIONS OF WEIGHTED WINDOW FUNCTIONS

Some combinations of weighted window functions were tested using a single line of sampled data extracted from the fringe image of a test hemisphere. The height distribution on that line was known. The reconstructed height distribution using a pair of weighted window functions was compared with the known value. The differences between them are called as errors and the statistics of these errors are shown in this appendix.

The eight weighted window functions that were tested are defined by the following equations. In those equations, N is the number of uniformly spaced samples and k = 0, 1, . . . , N-1.

1) Rectangle (Dirichlet) window function (Rec)

$$w_k = 1.0 \tag{II-B-1}$$

2) Hanning window function (Han)

$$w_k = 0.5*(1.0 - \cos\frac{2k\pi}{N}) \tag{II-B-2}$$

3) Hamming window function (Ham)

$$w_k = 0.54 - 0.46 \cos(\frac{2k\pi}{N}) \tag{II-B-3}$$

4) Cosine^4 window function (Cos4)

$$w_k = \cos^4(\frac{k\pi}{N}) \tag{II-B-4}$$

5) Blackman window function (Black)

$$w_k = 0.42 - 0.50\cos\left(\frac{2k\pi}{N}\right) + 0.08\cos\left(\frac{4k\pi}{N}\right) \qquad \text{(II-B-5)}$$

6) Exact Blackman window (XBlack)

$$w_k = 0.42659071 - 0.49656062\cos\left(\frac{2k\pi}{N}\right) + 0.07684867\cos\left(\frac{4k\pi}{N}\right) \qquad \text{(II-B-6)}$$

7) Minimum 3-Term Blackman-Harris window function (BHar3)

$$w_k = 0.42323 - 0.49755\cos\left(\frac{2k\pi}{N}\right) + 0.07922\cos\left(\frac{4k\pi}{N}\right) \qquad \text{(II-B-7)}$$

8) Minimum 4-Term Blackman-Harris window function (BHar4)

$$w_k = 0.35875 - 0.48829\cos\left(\frac{2k\pi}{N}\right) + 0.14128\cos\left(\frac{4k\pi}{N}\right) - 0.01168\cos\left(\frac{6k\pi}{N}\right) \qquad \text{(II-B-8)}$$

The statistics of errors are shown in Table II.B.1, which include the mean of errors, the standard deviation of errors, the mean of the squared errors, the mean of the absolute errors and the maximum of errors. Although not all the combinations of weighted window functions are shown here, the result has shown a tendency that using any weighted window functions except the rectangle window function with the isolated first sidelobe will dramatically reduce all statistical values of errors. Some large values that come from the incorrect phase wrapping would not affect this clear tendency.

Table II.B.1: Statistics of errors for different combinations of windows

Windows	Mean (mm)	Std. Dev. (mm)	Sqr. mean (mm)	Abs. mean (mm)	Maximum (mm)
Rec/Rec	-0.3422	1.057	1.234	0.6058	6.198
Han/Rec	-0.7545	2.191	5.37	1.183	14.99
Ham/Rec	-0.3623	1.081	1.299	0.6939	5.925
Cos4/Rec	31.82	6.414	1054	31.82	57.17
Black/Rec	-0.7545	2.191	5.37	1.183	14.99
XBlack/Rec	-0.4475	1.779	3.365	1.084	9.884
BHar3/Rec	30.82	2.235	954.7	30.82	35.08
BHar4/Rec	31.77	6.065	1046	31.77	57.58
Rec/Han	-0.3043	0.9962	1.085	0.4876	5.063
Han/Han	0.03788	0.5568	0.3114	0.3711	2.636
Ham/Han	-0.03758	0.6484	0.4218	0.3866	3.403
Cos4/Han	0.389	0.569	0.4751	0.532	2.554
Balck/Han	0.03788	0.5568	0.3114	0.3711	2.636
XBlack/Han	0.1364	0.5141	0.2829	0.4065	2.105
BHar3/Han	0.1466	0.5091	0.2806	0.4077	2.033
BHar4/Han	0.3482	0.543	0.4161	0.4939	2.415
Rec/Ham	-0.3094	0.992	1.08	0.4904	5.18
Han/Ham	-0.01469	0.6135	0.3766	0.3882	3.009
Ham/Ham	-0.07491	0.6788	0.4663	0.3873	3.693

PART II REFERENCES

2. Burton D. R., and Lalor M. J., *The Precision Measurement of Engineering form by Computer Analysis of Optically Generated Contours,* **SPIE.** Vol. 1010 Industrial Inspection, pp. 17 - 25, 1988.
1. Burton D. R., and Lalor M. J., *Managing Some of the Problems of Fourier Fringe Analysis,* **SPIE.** Vol. 1163 Fringe Pattern Analysis, pp. 149 - 160, 1989.
3. Chen Z., and Perng D. B., *Automatic Reconstruction of 3-D Solid Objects from 2-D Orthographic Views,* **Pattern Recognition,** Vol. 21, No. 5, pp. 439 - 449, 1988.
4. Cielo P., and Vaudreuil G., *Optical Inspection of Industrial Materials by Unidimensional Fourier Transfrom,* **Applied Optics,** Vol. 27, No. 15, pp. 4645 - 4652, 1988.
5. Clarke R., *Techniques for Accurate Non-contact 3-D Surface Profile Measurement,* **MIRINZ Internal Memorandum,** IM 262, 1991.
6. Green R. J., and Walker J. G., *Phase Unwrapping Using A-Priori Knowledge About the Band Limits of a Function,* **SPIE** Vol. 1010 Industrial Inspection, pp. 36 - 43, 1988.
7. Green R. J., Walker J. G., and Robinson D. W., *Investigation of the Fourier-transform Method of Fringe Pattern Analysis,* **Optics and Lasers in Engineering,** Vol. 8, pp. 29 - 44, 1988.
8. Harris F. J., *On the Use of Windows for Harmonic Analysis With the Discrete Fourier Transform,* **Proceedings of the IEEE,** Vol. 66, No. 1, pp. 51 - 83, January 1978.
9. Huntley J. M., *Noise-Immune Phase Unwrapping Algorithm,* **Applied Optics,** Vol. 28, No. 15, pp. 3268 - 3270, 1989.
10. Idesawa M., High-Precision Image Position Sensing Methods Suitable for 3-D Measurement, **Optics and Lasers in Engineering,** Vol. 10, pp. 191 - 204, 1989.
11. Judge T. R., Quan C., and Bryanston-Cross P. J., *Holographic Deformation*

Measurements by Fourier Transform Technique With Automatic Phase Unwrapping, **Optical Engineering,** Vol. 31, No. 3, pp. 533 - 543, March 1992.

12. Kreis T., *Digital Holographic Interference-Phase Measurement Using the Fourier-Transform Method,* **J. Opt. Soc. Am.** Vol. 3, No. 6, pp. 847 - 855, June 1986.
13. Kujawinska M., and Robinson D. W., *Multichannel Phase-Stepped Holographic Interferometry,* **Applied Optics,** Vol. 27, No. 2, pp. 312 - 320, 1989.
14. Lai G., and Yatagai T., *Dual-Reference Method Holographic Interferometry With a Double Pulsed Laser,* **Applied Optics,** Vol. 27, No. 18, pp. 3855 - 3858, 1988.
15. Malcolm A. et al., *Full Field Fourier Fringe Analysis for Industrial Inspection,* **SPIE,** Vol. 1265 Industrial Inspection II, pp. 165 - 178, 1990.
16. Nakadate S., and Saito H., *Fringe Scanning Speckle-Pattern Interferometry,* **Applied Optics,** Vol. 24, No. 14, pp. 2172 - 2180, 1985.
17. Patorski K., *Moire Methods in Interferometry,* **Optics and Lasers in Engineering,** Vol. 8, pp. 147 - 170, 1988.
18. Prim R. C., *Shortest Connection Networks and Some Generalizations,* **The Bell System Technical Journal,** Vol. 36, pp. 1389 - 1401, 1957.
19. Robinson R. W., and Williams D. C., *Digital Phase Stepping Speckle Interferometry,* **Optical Communications,** Vol. 57, No. 1, pp. 26 - 30, 1986.
20. Santoyo F. M. et al, *Interferometric Fringe Analysis Using a Single Phase Step Technique,* **Applied Optics,** Vol. 27, No. 21, pp. 4363 - 4364, 1988.
21. Spik A., and Robinson D. W., *Investigation of the Cellular Automata Method for Phase Unwrapping and its Implementation on an Array Processor,* **Optics and Lasers in Engineering,** Vol. 14, pp. 25 - 37, 1991.
22. Suzuki M., and Kanaya, M., *Application of Moire Topography Measurement Methods in Industry,* **Optics and Lasers in Engineering,** Vol. 8, pp. 171 - 188, 1988.
23. Takeda M. et al., *Fourier Transform Profilometry for the Automatic Measurement of 3-D Object Shapes*, **Applied Optics,** Vol. 22, No. 24, pp. 3977 - 3982, December 1983.
24. Takeda M. et al., *Fourier-transform Method of Fringe-pattern Analysis for*

Computer-based Topography and Interferometry, **Journal of Optics Society America,** Vol. 72, No. 1, pp. 156 - 160, January 1982.

25. Towers D. P., Judge T. R., and Bryanston-Cross P. J., *A Quasi Heterodyne Holographic Technique and Automatic Algorithms for Phase Unwrapping,* **SPIE** Vol. 1163 Fringe Pattern Analysis, pp. 95 - 119, 1989.
26. Towers D. P., Judge T. R., and Bryanston-Cross P. J., *Analysis of Holographic Fringe Data Using the Dual Reference Approach,* **Optical Engineering,** Vol. 30, No. 4, pp. 452 - 460, 1991.
27. Vrooman H. A., and Mass A. A. M., *New Image Processing Algorithm for the Analysis of Speckle Interference Patterns,* **SPIE.** Vol. 1163 Fringe Pattern Analysis, pp. 51 - 61, 1989.
28. William W. Macy Jr., *Two-Dimensional Fringe-Pattern Analysis,* **Applied Optics,** Vol. 22, No. 23, pp. 3898 - 3901, December 1993.
29. Zhang S. Y., and Soukas A. V., *Optimization of Phase Sensitive Detectors Using Fast Fourier Transform,* **Measurement Science Technology,** Vol. 2, pp. 13 - 18, 1991.